



저작자표시-비영리-변경금지 2.0 대한민국

이용자는 아래의 조건을 따르는 경우에 한하여 자유롭게

- 이 저작물을 복제, 배포, 전송, 전시, 공연 및 방송할 수 있습니다.

다음과 같은 조건을 따라야 합니다:



저작자표시. 귀하는 원저작자를 표시하여야 합니다.



비영리. 귀하는 이 저작물을 영리 목적으로 이용할 수 없습니다.



변경금지. 귀하는 이 저작물을 개작, 변형 또는 가공할 수 없습니다.

- 귀하는, 이 저작물의 재이용이나 배포의 경우, 이 저작물에 적용된 이용허락조건을 명확하게 나타내어야 합니다.
- 저작권자로부터 별도의 허가를 받으면 이러한 조건들은 적용되지 않습니다.

저작권법에 따른 이용자의 권리는 위의 내용에 의하여 영향을 받지 않습니다.

이것은 [이용허락규약\(Legal Code\)](#)을 이해하기 쉽게 요약한 것입니다.

[Disclaimer](#)

Doctoral Thesis

Kinetics of Charge Transfer and Oxygen Evolution  
via Surface Functionalization  
at the Transition Metal Based Catalysts

Tae Won Lee

Department of Materials Science and Engineering

Graduate School of UNIST

2020

Kinetics of Charge Transfer and Oxygen Evolution  
via Surface Functionalization  
at the Transition Metal Based Catalysts

Tae Won Lee

Department of Materials Science and Engineering

Graduate School of UNIST

Kinetics of Charge Transfer and Oxygen Evolution  
via Surface Functionalization  
at the Transition Metal Based Catalysts

A thesis/dissertation  
submitted to the Graduate School of UNIST  
in partial fulfillment of the  
requirements for the degree of  
Doctor of Philosophy

Tae Won Lee

06. 16. 2020

Approved by

---

Advisor

Kyoung Jin Choi

Kinetics of Charge Transfer and Oxygen Evolution  
via Surface Functionalization  
at the Transition Metal Based Catalysts

Tae Won Lee

This certifies that the thesis/dissertation of Tae Won Lee is approved.

06. 16. 2020

signature

---

Advisor: Kyoung Jin Choi

signature

---

Jeong Min Baik: Thesis Committee Member #1

signature

---

Hyesung Park: Thesis Committee Member #2

signature

---

Seungho Cho: Thesis Committee Member #3

signature

---

Joonki Suh: Thesis Committee Member #4;

## Abstract

It has been attracting many attentions to develop a renewable, sustainable way to replace fossil-fuel based energy systems. Among the many candidates, hydrogen based energy systems have possibility of clean and secure future due to low-carbon society. Water splitting has huge potential for production of hydrogen in a clean way, for its source is water - renewable and nearly infinite source. However, it is only 4% portion in hydrogen production because of high cost and lack of industrial foundation. To deal with these problems, one of the solution is to develop the low-cost and highly efficient catalyst for hydrogen evolution reaction (HER) and oxygen evolution reaction (OER) to replace the noble metals (Pt) and precious metal oxides ( $\text{RuO}_2$  and  $\text{IrO}_2$ ), respectively. Especially, it is important to consider charge transfer kinetics for developing effective electrocatalyst. In this viewpoint, two main strategy were used in this study. One is the nitrogen (N) doped graphene quantum dots functionalization of perovskite oxide for better OER electrocatalyst, the other is adding conductive copper (Cu) ions to nickel phosphide (Ni-P) as an effective bifunctional electrocatalyst for overall water splitting.

First N-doped graphene quantum dot functionalized  $\text{La}_x\text{Sr}_{1-x}\text{CoO}_3$  was synthesized as a highly active electrocatalyst for OER to deal with sluggish kinetics of OER, bottleneck for water splitting. Perovskite oxide  $\text{ABO}_3$  (A: alkaline or rare earth metal, B: transition metal) have been attracting many attentions due to flexible electronic structure, high activity descriptor, good stability, etc. Among them,  $\text{La}_x\text{Sr}_{1-x}\text{CoO}_3$  have received many attentions as a highly active catalyst. And applying N doped-graphene quantum dot is a promising way for engineering of perovskite oxide to build high-performance OER catalyst by controlling charge transfer in the catalyst.

Second, Cu-doped Ni-P was synthesized by electrodeposition for effective electrocatalyst for overall water splitting. The incorporation of Cu into the Ni-P is expected to improve the electrocatalytic performances because of the reduction of charge transfer resistance and opposite sign of adsorption energy with hydrogen on Cu compared with that of Ni. It could be functioned as bifunctional electrocatalyst for overall water splitting. Finally, moisture formed on the surface was removed effectively by using water splitting reactions, which convert water into volatile hydrogen/oxygen gases. It was realized by 2-dimensional device with interdigitated pattern coated with highly active electrocatalyst NiCu-P for water splitting.

## Contents

<b>CHAPTER 1. INTRODUCTION</b> .....	1
<b>CHAPTER 2. THEORETICAL BACKGROUND</b> .....	5
2.1 General strategy of development of electrocatalyst for water splitting .....	5
2.2 Descriptors for HER/OER .....	7
<b>CHAPTER 3. EXPERIMENTAL PROCEDURE/PARAMETER</b> .....	9
3.1 Overpotential ( $\eta$ ) and Tafel Slope .....	9
3.2 How to evaluating experimentally observed current .....	9
3.3 References .....	11
<b>CHAPTER 4. HIGHLY ACTIVE OXYGEN ELECTROCATALYST BASED ON N-DOPED GRAPHENE QUANTUM DOT FUNCTIONALIZED PEROVSKITE</b> .....	13
4.1 Introduction .....	13
4.2 Experimental details .....	14
4.2.1 Synthesis and ball-milling of Perovskite oxide .....	14
4.2.2 Synthesis of the N-doped graphene quantum dots, and the N-GQD functionalized LSCO .....	15
4.2.3 Material characterization .....	15
4.2.4 Electrochemical measurement .....	16
4.2.5 Electrochemical reduction of the catalyst electrode .....	17
4.3 Results and Discussion .....	17
4.3.1 Ball-milling of perovskite oxide for optimization of the electrocatalyst.....	17
4.3.2 Functionalization of N-Graphene Quantum Dot $\text{La}_{0.5}\text{Sr}_{0.5}\text{CoO}_3$ .....	22
4.3.3 Mechanism of N-GQD LSCO by analyzing XPS .....	25

4.3.4 Synthesis of perovskite under low temperature.....	27
4.3.5 Electrochemical reduction for formation of oxygen vacancy.....	30
4.4 Conclusion .....	31
4.5 References .....	32
<b>CHAPTER 5. ELECTROCATALYTICALLY DRIVEN FAST REMOVAL OF MOISTURE BY CONDENSATION OF VAPOR AND WATER SPLITTING .....</b>	<b>35</b>
5.1 Introduction .....	35
5.2 Experimental details .....	38
5.3.1 Electrodeposition of Ni-P and NiCu-P films.....	38
5.3.2 Material characterization.....	38
5.3.3 Electrochemical measurement in a three-electrode configuration.....	39
5.3.4 Fabrication of two-electrode electrochemical cells .....	39
5.3.5 Measurement of two-electrode electrochemical cells.....	40
5.3 Results and Discussion .....	40
5.3.1 Electrodeposition of Ni-P and NiCu-P films.....	40
5.3.2 Electrocatalytic HER and OER performances in Acidic and Basic Media .....	45
5.3.3 Two-electrode electrochemical devices in DI water .....	47
5.3.4 Two-electrode planar electrochemical cells .....	50
5.4 Conclusion .....	57
5.5 References .....	59
<b>CURRICULUM VITAE .....</b>	<b>65</b>



## LIST OF FIGURES

- Figure 1.** Hydrogen-economy roadmap
- Figure 2.** Three main methods to produce hydrogen for industries
- Figure 3.** Two half-reactions in electrochemical water splitting
- Figure 4.** (a) Role of catalyst in chemical reactions, (b) I-V curve in full cell in water splitting
- Figure 5.** Strategy for development of effective electrocatalyst for water splitting by increase of the number of active sites such as porous structures, nanoparticles
- Figure 6.** Strategy for development of effective electrocatalyst for water splitting by improving intrinsic activity in each active site such as oxygen vacancy control, functionalization
- Figure 7.** (a) Reaction steps in HER on the surface of catalyst, (b)Volcano plot for various metals in HER
- Figure 8.** (a) Reaction steps in OER on the surface of catalyst (b) Volcano plot for metal oxides and (c) perovskite oxide in OER
- Figure 9.** Simple schematics explaining geometrical/electrochemically active surface area in  $\text{MoS}_2$
- Figure 10.** Linear sweep voltammetry (LSV) polarization curves of LSCO-NG with varying ratio of NGQD and LSCO
- Figure 11.** Schematics of synthesizing N-doped graphene quantum dot (N-GQD) functionalized  $\text{La}_x\text{Sr}_{1-x}\text{CoO}_3$  (LSCO)
- Figure 12.** SEM images of perovskite oxide ( $\text{La}_{0.5}\text{Sr}_{0.5}\text{CoO}_3$ ) after ball-milling process by changing processing time (a) pristine samples (without ball-milling). Samples ball-milled for (b) 0.5 hours (c) 3 hours, (d) 12 hours. Perovskite oxide particles were mixed with ethanol, before pulverized by wet ball-milling.
- Figure 13.** Size of perovskite oxide particles by wet ball-milling by varying processing time. Data was acquired by dynamic laser scattering (DLS). Concentration of the sample was 0.1 mg in 1 ml ethanol. Standard deviation was inserted in the graph at each

condition.

**Figure 14.** (a) Mass activity (MA) based on the catalyst weight of each ball-milled LSCO catalyst at an overpotential of  $\eta=0.5$  V and (b) Specific activity of ball-milled LSCO, in which surface area was ECSA (Electrochemically active surface area). Inset graph was difference in current density measured by cyclic voltammetry with varying scan rates. ECSA was estimated by calculating double-layer capacitance values extracted from linear fitting curves.

**Figure 15.** (a) Linear sweep voltammetry (LSV) polarization curves in 1.0 M KOH of ball-milled LSCO with different processing time. Arrow shows trend of the ball-milling time to OER performances and (b) corresponding Tafel plot.

**Figure 16.** XPS spectra of C 1s and O 1s for pristine and ball-milled (3 h) LSCO samples

**Figure 17.** XPS spectra of Co 2p for pristine and ball-milled (3 h) LSCO samples.

**Figure 18.** XRD patterns of pristine and ball-milled (3 h) LSCO samples (a) in range of  $20^\circ \sim 60^\circ$  and of (b)  $32^\circ \sim 34^\circ$

**Figure 19.** XRD patterns of LSCO, LSCO-BM, LSCO-QD, LSCO-NG samples

**Figure 20.** TEM (with higher magnification) and FFT images of N-GQD and LSCO-GQD NPs.

**Figure 21.** TEM (with higher magnification) and FFT images of LSCO-NG NPs.

**Figure 22.** (a) Linear sweep voltammetry (LSV) polarization curves of functionalized LSCO with conditions in 1.0 M KOH. (b) Corresponding Tafel plot and (c) Nyquist plot measured at 1.8 V (vs RHE).

**Figure 23.** XPS spectra of the functionalized LSCO: C 1s, N 1s spectra of LSCO, LSCO-GQD, LSCO-NG.

**Figure 24.** XPS spectra of the functionalized LSCO: Co 2p and O 1s spectra of LSCO, LSCO-GQD, LSCO-NG

**Figure 25.** Superoxide molecular cluster formation using cyano/superoxide molecular clusters, compared with conventional methods using amorphous clusters

**Figure 26.** (a) Reaction path using polymorph method and (b) cyano-gel based synthesis based

on mixed valence complex.

**Figure 27.** The (a) SEM images of perovskite oxides synthesized by conventional sol-gel process and cyano-complex route (scale bar: 500 nm) and (b) dynamic laser scattering (DLS) data made by both methods.

**Figure 28.** XRD data of  $\text{LaNiO}_3$  before annealing, after annealing of sol-gel and low temperature process (left) and same materials with post treatment using  $\text{H}_2\text{O}_2$  and without adding  $\text{H}_2\text{O}_2$  for annealing at 500, 600°C for 6 hours.

**Figure 29.** (a) Linear sweep voltammetry (LSV) polarization curves of  $\text{LaNiO}_3$  with applying different negative bias in 20 min. for electrochemical reduction in 1.0 M KOH, (b) LSV curves of  $\text{LaNiO}_3$  with different treatment times at -0.4V vs RHE.

**Figure 30.** (a) Moisture formation in daily lives, and (b) conventional several methods for removing moisture such as water absorber, heat exchanger, PEM electrolysis.

**Figure 31.** (a) Gibbs free energy of adsorption of hydrogen in Ni-P compared with Pt, (b) Calculated electron density of the  $\text{Ni}_2\text{P}$  surface, (c) TEM images of Ni-P with oxidation shell of  $\text{NiO}_x$  after OER, (d) Volcano plot for metals including Ni and Cu, (e) Bonding charge distribution of Cu-doped Cobalt phosphide.

**Figure 32.** (a) Precursors used and photo of NiCu-P solution. (b) Schematic illustration of NiCu-P film with  $\text{CuSO}_4 \cdot 6\text{H}_2\text{O}$  concentration. (c) Photos and SEM images of NiCu-P film on  $\text{SiO}_2/\text{Si}$  substrate with Ti/Ni (20/100 nm) with  $\text{CuSO}_4 \cdot 6\text{H}_2\text{O}$  concentration. scale bar: 1  $\mu\text{m}$ . (d) XRD data of electrodeposited NiCu-P film on Ni substrate with Cu content. (e) High-resolution TEM images of NiCu-P film and the corresponding fast Fourier Transform (FFT) patterns of the selected area. scale bar: 20 nm.

**Figure 33.** The photos of NiCu-P solutions with different  $\text{CuSO}_4 \cdot 6\text{H}_2\text{O}$  concentration.

**Figure 34.** The SEM images of the NiCu-P with different ratios of Ni:Cu (scale bar: 0.5  $\mu\text{m}$ ).

**Figure 35.** (a) EDX elemental analysis of Ni-P. (b) Formation energy of Ni-P with the different mole fraction of P. (c) Elemental composition (Ni, Cu) of NiCu-P with the different mole of  $\text{NiSO}_4 \cdot 6\text{H}_2\text{O}$  of precursors.

**Figure 36.** (a) Linear sweep voltammetry (LSV) polarization curves of NiCu-P films with different ratios of Ni:Cu in 0.5 M H<sub>2</sub>SO<sub>4</sub> at scan rate of 10 mV/s. The inset shows the SEM images of NiCu-P film with 9 at. % on Ni foam. Scale bar: 25, 10 μm. (b) Corresponding Tafel plots. (c) Nyquist plots recorded obtained at - 0.3V versus RHE. (d) LSV polarization curves of NiCu-P films with different ratios of Ni:Cu in 1.0 M KOH. The current densities in ranging from 1.3 V to 1.6 V were also plotted in the inset. (e) Corresponding Tafel plot. (f) Nyquist plots recorded obtained at 1.55V versus RHE.

**Figure 37.** (a) LSV polarization curves of Ni-P and Ni<sub>91</sub>Cu<sub>9</sub>-P films on Ni recorded in 1.0 M KOH. The inset shows the current density measured in pure water. (b) Current densities measured at various voltages from 2 to 10 V in pure water. The inset shows the gas bubbles on both surfaces when 10 V is applied. Scale bar: 1 mm. (c) Top (scale bar: 1, 10 μm) and cross-sectional. scale bar: 1 μm. SEM images of the Ni<sub>91</sub>Cu<sub>9</sub>-P films after the HER and OER reaction at 10 V in pure water. (d) pH values of electrolytes measured as a function of the water splitting reaction time at 10 V before and after Ni<sub>91</sub>Cu<sub>9</sub>-P films were treated with O<sub>2</sub> plasma treatment. O<sub>2</sub> plasma-treated NiCu-P film was named as NiCu-PO<sub>x</sub>. (e) Current densities measured at 10 V with O<sub>2</sub> plasma treatment in pure water. (f) Top and cross-sectional SEM images of the Ni<sub>91</sub>Cu<sub>9</sub>-P films after the OER reaction at 10 V in pure water. scale bar: 10, 1 μm. (g) EDAX spectra of as-deposited NiCu-P and O<sub>2</sub> plasma-treated NiCu-P films.

**Figure 38.** (a) LSV polarization curves for the HER of Ni-P and Ni<sub>91</sub>Cu<sub>9</sub>-P films on Ni recorded in pure water. (b) LSV polarization curves for the OER of Ni-P and Ni<sub>91</sub>Cu<sub>9</sub>-P films on Ni recorded in pure water.

**Figure 39.** Currents measured as a function of the applied voltage ranging from -0.25 to 0.25 V with Ni<sub>91</sub>Cu<sub>9</sub>-P and Ni-P. The inset shows a schematic illustration of I-V measurement of a device.

**Figure 40.** (a) Currents measured as a function of the applied voltage ranging from -0.25 to 0.25 V with Ni-P and NiO. (b) Current densities measured at 10 V of Ni-P/Ni-P, Ni-P for HER/NiO for OER with two-electrode cell in pure water at voltages of 10 V. (c) The SEM images of the NiO for OER films after the HER and OER reaction

at 10 V in pure water, respectively. Scale bar: 500 nm.

**Figure 41.** (a) Schematic illustration for the fabrication of two-electrode planar cells, composed of two interdigitated electrodes of NiCu-P for HER and NiCu-PO<sub>x</sub> for OER. The photo and SEM image of the cell at a wafer scale was also shown. scale bar: 1, 20 mm. (b) Currents measured as a function of the applied voltage with a few pure water drops onto the cells of approximately 2 x 2 cm<sup>2</sup> in area. The inset shows the gas bubbles generated between the two electrodes. The water removal rate with the voltage was also plotted. (c) Currents measured at various voltages from 2 to 10 V in pure water. (d) Currents measured at 10 V during 3 hrs when the cell was dipped into pure water. The SEM images of the Ni<sub>91</sub>Cu<sub>9</sub>-P films after the HER and OER reaction at 10 V in pure water, respectively. Scale bar: 50 μm. (e) Currents measured under various humidity of the inside of the headlamp of a car from 20 to 99 %. The 4 cells were attached to the inner surface and the photos after the reaction at 13.6 V for 10 min were shown. The SEM images of the Ni<sub>91</sub>Cu<sub>9</sub>-P films after the reaction were also shown. scale bar: 50 μm.

**Figure 42.** Currents measured at various voltages from 2 to 10 V with two-electrode planar cells based on Ni-P for HER/Ni-PO<sub>x</sub> for OER in pure water.

**Figure 43.** Photos of the inside surface of headlamp before/after 60 minutes under the humidity of 99%.

**Figure 44.** (a) Schematic images of flexible cells with hole patterns fabricated PEN substrate. The photo and SEM image of the cell at a wafer scale was also shown. scale bar: 2 cm, 0.4 mm. (b) Transmittance spectra of the cells with and without hole patterns. (c) Currents measured at 13.6 V under 99 % relative humidity of the headlamp of a car. The cell was attached to the inner surface of the headlamp. (d) Currents measured at 10 V with the curvature of the bending motion when it was dipped into the pure water, as shown in the inset.

**Figure 45.** (a) Photos of bending flexible planar devices with different bending curvature. (b) Currents measured with the flexible and transparent device at 10 V in pure water with different bending curvature.

## CHAPTER 1. INTRODUCTION

These days, energy sources, transportation and industries mainly rely on fossil fuels, which may induce global warming and destroy environments. It has been attracting many attention to develop a renewable, sustainable way to replace fossil fuel based energy systems. Among the many candidates, hydrogen based energy systems have possibility of clean and secure future due to low-carbon society. And effective hydrogen production, storage, transportation are critical factors in this system.

Meanwhile, hydrogen economy is a kind of system that depends on this energy source as the common fuel that could deliver a major part of energy and industries in a country. For example, Korean government announced hydrogen-economy roadmaps, related to hydrogen vehicles, H<sub>2</sub> charging station, fuel cells (Figure. 1) for alternatives to conventional energy systems. It is expected that hydrogen related field will increase rapidly in 20 years.

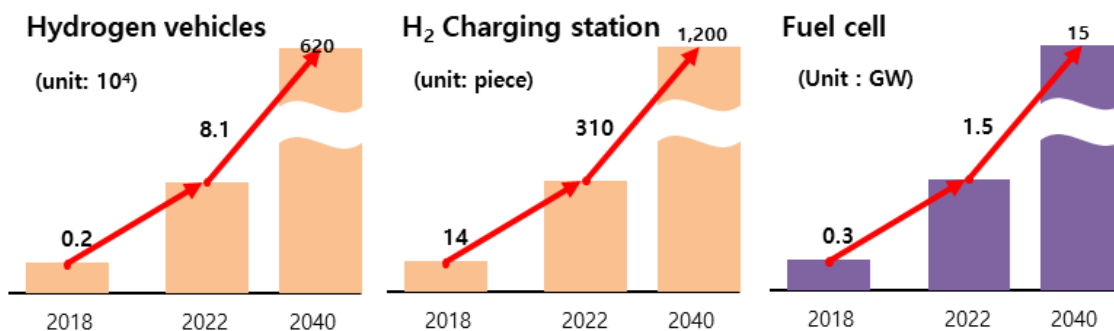


**Figure 1.** Hydrogen-economy roadmap (announced by Ministry of Trade, Industry and Energy in Korea)

They are one of the most promising systems, which can alleviate the emission of carbon dioxide (greenhouse effect) and prevent energy resource exhaustion. In spite of such an attractive potentials, it is difficult to get "molecular hydrogen" independently and additional process for generating hydrogen is essential from other hydrogen containing compound such as hydrocarbons and water.

Most of hydrogen is produced industrially by following three main ways in these days. (Figure. 2). One is made by SMR (Steam-Methane Reforming), representative production process from a methane with a high-temperature (over 700°C) steam to produce H<sub>2</sub> and CO<sub>2</sub>, before water-gas shift reaction (CO react with steam for hydrogen and CO<sub>2</sub>). Second, hydrogen is generated by

reacting O<sub>2</sub>, coal and steam under high pressures and temperatures to make mixture of CO and H<sub>2</sub> gases. Following water-gas shift reaction converts the mixture gases to additional H<sub>2</sub> and CO. Third one is electrolysis of water, which converted to only hydrogen and oxygen. With this process, hydrogen is produced in a clean way. Former two methods are more economic than latter one, and related to conventional industrial process, so most of the hydrogen production mainly depends on them (over 95%). However they are strongly depends on fossil-fuel based system, which can induce air pollution and emit carbon dioxide, which cause greenhouse effect. So environmental issues cannot be solved using these two methods. Different from them, water electrolysis has huge potential to produce hydrogen in a clean way, for its source is water - renewable and nearly infinite source.

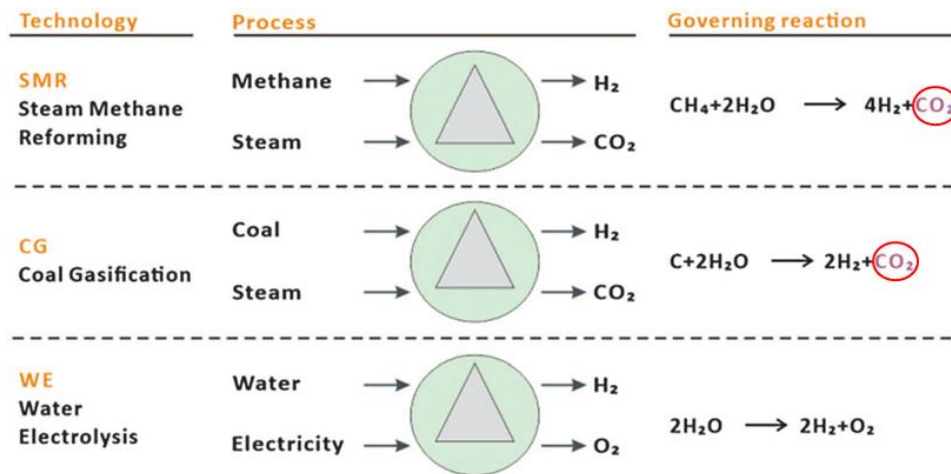
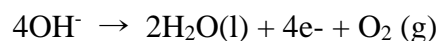
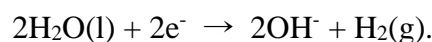


**Figure 2.** Three main methods to produce hydrogen for industries [1]

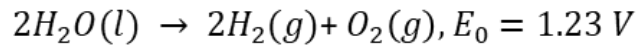
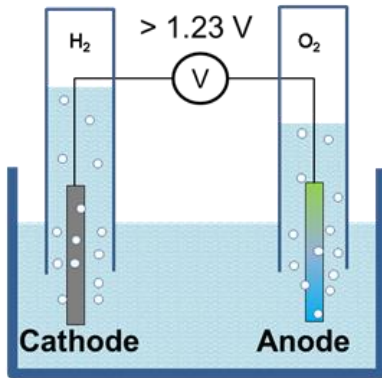
A typical schematic of full cells for electrochemically water splitting is shown in the Figure 3. In alkaline conditions, hydroxide ions which are dominant in electrolyte, converted to water and oxygen gases at the anode as the following equation:



This is known as the oxygen evolution reaction (OER). Generated electrons move through the external circuit to meet water molecule at the cathode (to circulate the electrochemical circuit). Then, water is reduced by getting electrons to produce hydrogen at the cathode, which called hydrogen evolution reaction (HER):







In Half-reaction,

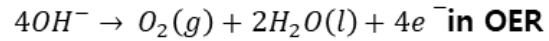
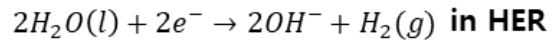


**Figure 3.** Two half-reactions in electrochemical water splitting

In thermodynamic perspectives, the minimum energy for splitting water is 1.23 V. But more energy is needed to accelerate the reactions at proper rates (in viewpoint of kinetics), which called activation energy. To reduce activation energy, catalyst is required as seen in Figure 4. (a). In I-V curves, we can consider required energy as voltages, reaction rates as current density (current divided by surface area). Especially, additional energy over the theoretical value (1.23V) at given current density is called overpotential. (expressed as symbol  $\eta$ ).

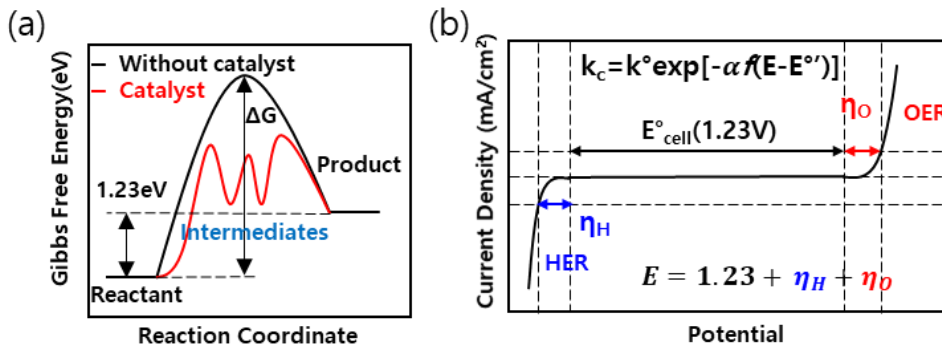


**Figure 4.** (a) Role of catalyst in chemical reactions, (b) I-V curve in full cell in water splitting

So effective electrocatalysts is to decrease this overpotential as much as possible. In Figure 4(b), lower energy (E) is needed for splitting water with effective electrocatalyst due to reducing overpotentials ( $\eta_H$ ,  $\eta_O$ ) in each reaction (HER, OER). It is widely known that noble-metal based catalyst (Pt in HER,  $IrO_2$  or  $RuO_2$  in OER) showed the best performances. But due to high cost and scarcity, effective non-noble metal based electrocatalyst have been studied to replace them.



In the work described herein, we focused on the effective non-noble metal based electrocatalyst for water splitting. To realize this, we considered charge transfer kinetics on the transition metal based electrocatalyst in this study. First, perovskite oxide  $\text{LaSrCoO}_3$  (LSCO) was modified with N-doped graphene quantum dot (N-GQD) as an effective electrocatalyst for oxygen evolution reactions (OER).  $\text{LaSrCoO}_3$  particles were synthesized by sol-gel method, before broken into smaller particles by using ball-milling process. N-GQD was made by facile hydrothermal methods and mixed with perovskite oxides for synthesizing composite catalyst. Graphene Quantum Dot (GQD) was also made for comparing hetero-atom doped GQD to study effect of modification in detail. N-GQD samples showed better performances compared with well-known electrocatalyst,  $\text{IrO}_2$ . By modified with N-GQD, electron transferred from LSCO to N-GQD with maintaining the electroneutrality, which changed electronic structure of LSCO for highly active OER catalyst. Also N-GQD was acted as an active site for OER and formed p-n junction with LSCO for better charge transfer. Second, Cu-doped Ni-P was synthesized by electrodeposition for effective bifunctional electrocatalyst for overall water splitting. Especially, an electrocatalytically driven moisture control technology is demonstrated by condensation of vapor and water splitting. The incorporation of Cu into the Ni-P is expected to improve the electrocatalytic performances because of the reduction of charge transfer resistance and opposite sign of adsorption energy with hydrogen on Cu compared with that of Ni. In addition, it could be functioned as bifunctional electrocatalyst for overall water splitting. Finally, moisture was effectively removed by using 2-dimensional device with interdigitated pattern coated with NiCu-P. The devices can remove pure water with a speed of about 0.6 ml/h at 10 V. A transparent cell with flexibility was also fabricated and kept over 75 % capability under a curvature of 0.18/cm.

## CHAPTER 2. THEORETICAL BACKGROUND AND MOTIVATION

### 2.1 General strategy of development of electrocatalyst for water splitting

There are commonly two strategies to enhance the performances of an electrocatalyst (reaction rates): one is to increase the number of exposed active sites on a fixed area of a catalyst such as increasing loading or reducing size to nano-scale. The other is improving the intrinsic activity of each active sites, like alloying and doping to change surface properties of electrocatalyst. [2] Typical approach in former methods is breaking particles into nano-size by ball-milling or removing templates for porous structure with high surface area as seen in Figure 5. [3,4] Another approach, dispersing nanoparticles on the supports like 2-dimensional materials induces additional effect, that is enhancement of the conductivity of the electrocatalyst. [5] Certain materials has active sites only on edges, not basal planes, so novel structure exposing edge sites can significantly shows better catalytic activities. [6]

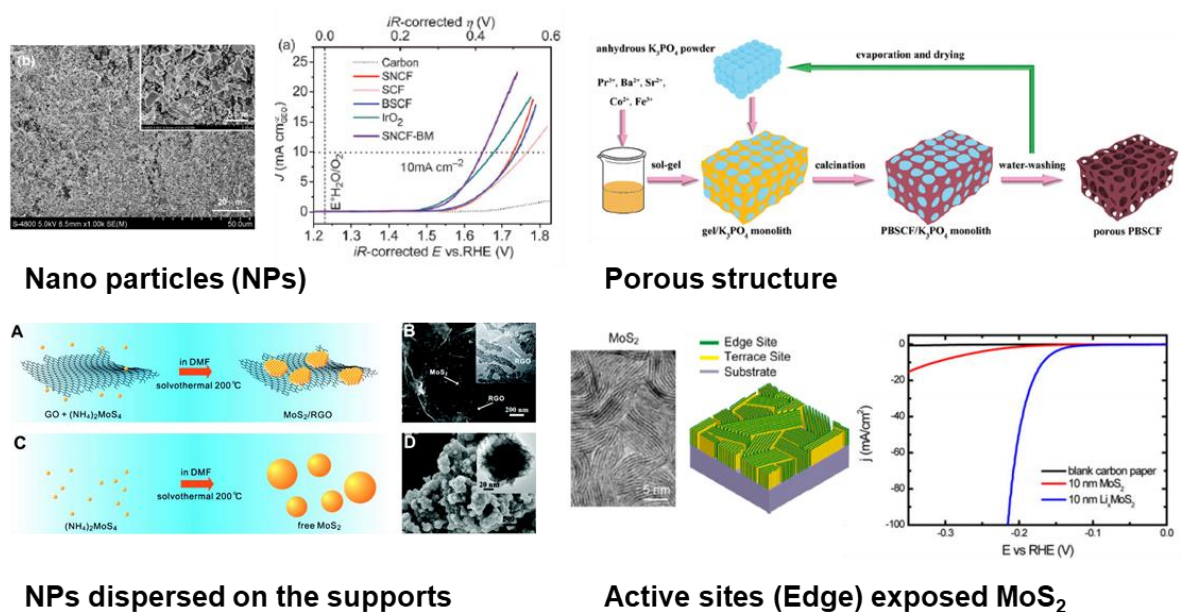


**Figure 5.** Strategy for development of effective electrocatalyst for water splitting by increase of the number of active sites such as porous structures, nanoparticles [3-6]

One of the usual method for improving intrinsic activity is changing composition of the electrocatalyst for water splitting. (Figure 6) Double perovskite is one of the attracting materials due to high flexibility of elements for tailoring the electronic and chemical properties. By changing amount of various elements, we can get the better performances of the

electrocatalyst. [7] Meanwhile, in oxide materials, oxygen diffusion is important factors in surface properties to catalyze water splitting reactions. It is commonly used to tune oxygen vacancies for enhancing intrinsic activities. [8] For TMDC (Transition Metal DiChalcogenides), number of layer determines structure and electronic property of the materials and changes the activity of the catalyst. So intercalation in  $\text{MoS}_2$  is the effective way to enhancing intrinsic catalytic activity by phase transition. [9] Functionalization of other materials such as metal, polymers, oxides is also good methods to improve the surface activity of the catalyst, act as a proton acceptors. [10] Actually latter methods are more efficient, for there is limit for mass and charge transport in cases of only increasing number of active sites. Surely, these two strategies can be realized simultaneously, inducing superior improvements in performances.

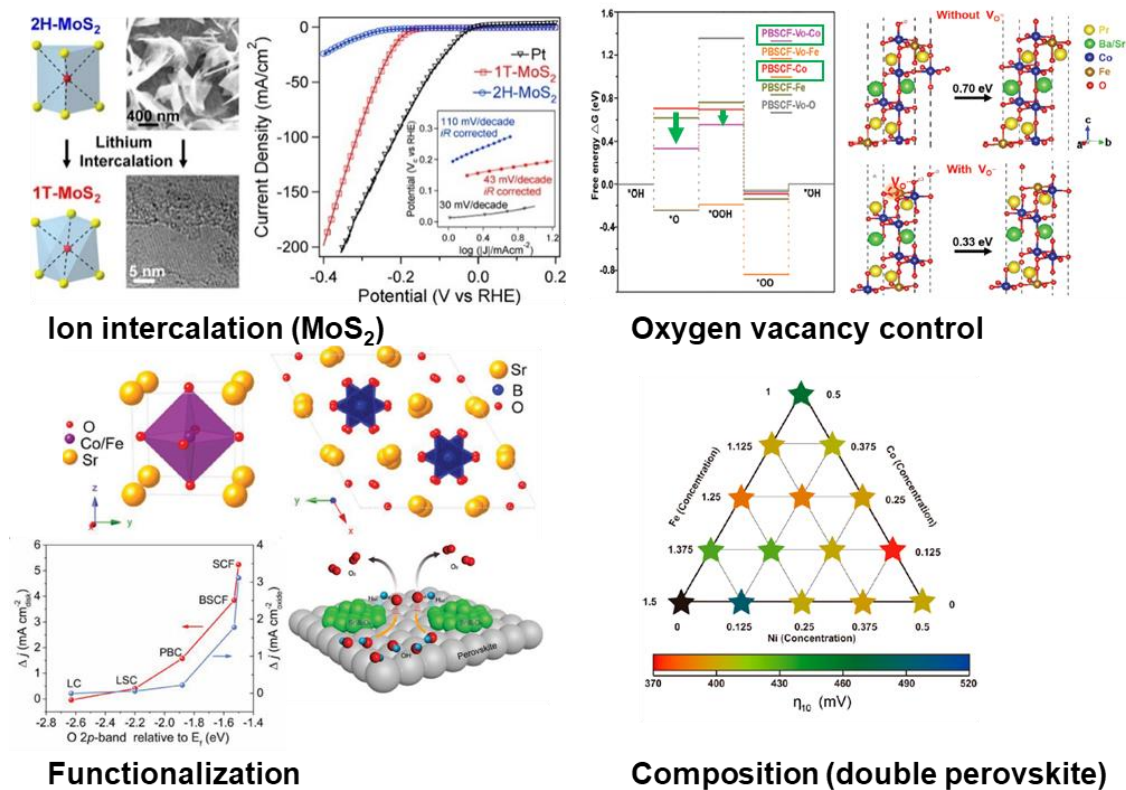


**Figure 6.** Strategy for development of effective electrocatalyst for water splitting by improving intrinsic activity in each active site such as oxygen vacancy control, functionalization [7-10]

## 2.2 Descriptors for HER/OER

By combining theory and experiments, simple but powerful tools (principles) was found for searching effective materials in HER and OER. That is activity descriptor for each reactions, which shows volcano relations. Using them, one can easily expect catalytic activity of the electrocatalyst for hydrogen/oxygen evolution reactions.

In HER, two electrons transfer for the reaction with only one intermediate (Figure 7(a)), and there are two types of main mechanisms, which are Volmer-Heyrovsky or the Volmer-Tafel. Each steps are suggested as below.

- 1-1.  $H^+ + e^- + * \rightarrow H^*$  (Volmer step)
- 1-2.  $H^* + H^+ + e^- \rightarrow H_2 + *$  (Heyrovsky step)
2.  $2H^* \rightarrow H_2 + 2*$  (Tafel step)

Considering so-called Sabatier principles, we can conclude a necessary condition to find an active HER catalyst is free energy of hydrogen adsorption,  $\Delta G_H \approx 0$ . If binding is too weak, Volmer step (adsorption) will constrain the overall reaction rate, whereas if the hydrogen binds too strongly, Heyrovsky/Tafel step (desorption) will determine the rate. The volcano relation between  $\Delta G_H$  and exchange current density is depict in Figure. 7(b) suggest a guide for the best catalyst for a given groups of catalyst materials. [11]

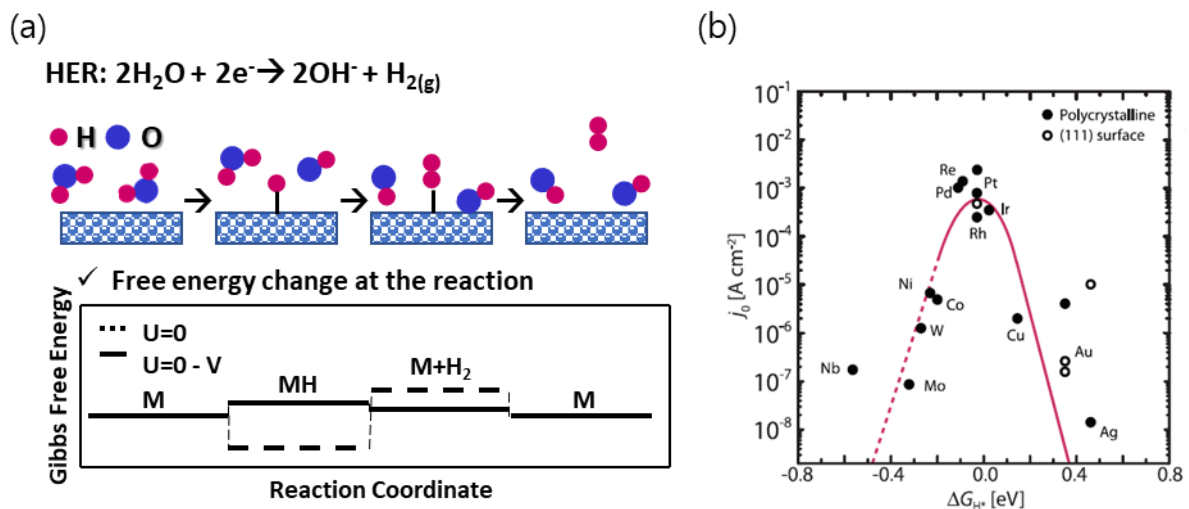


**Figure 7.** (a) Reaction steps in HER on the surface of catalyst, (b)Volcano plot for various metals in HER [11]

Compared with HER, OER is a complex reaction, which four electrons transfer reactions with catalytic intermediates (MOH, MO, MOOH) in Figure 8(a). Because metal oxide is reported as a common OER catalyst, OER volcano plots have been studied for various metal oxide surfaces such as binary oxide, spinel, rock salt, perovskite with  $\Delta G_{\text{O}} - \Delta G_{\text{OH}}$  as the descriptor. [2] In perovskite, another volcano relation is suggested that the filling of  $e_g$  orbitals in B-site metal cations can be main descriptor for OER. [12]. These two well-known volcanos are presented in Figure 8(b) and (c).

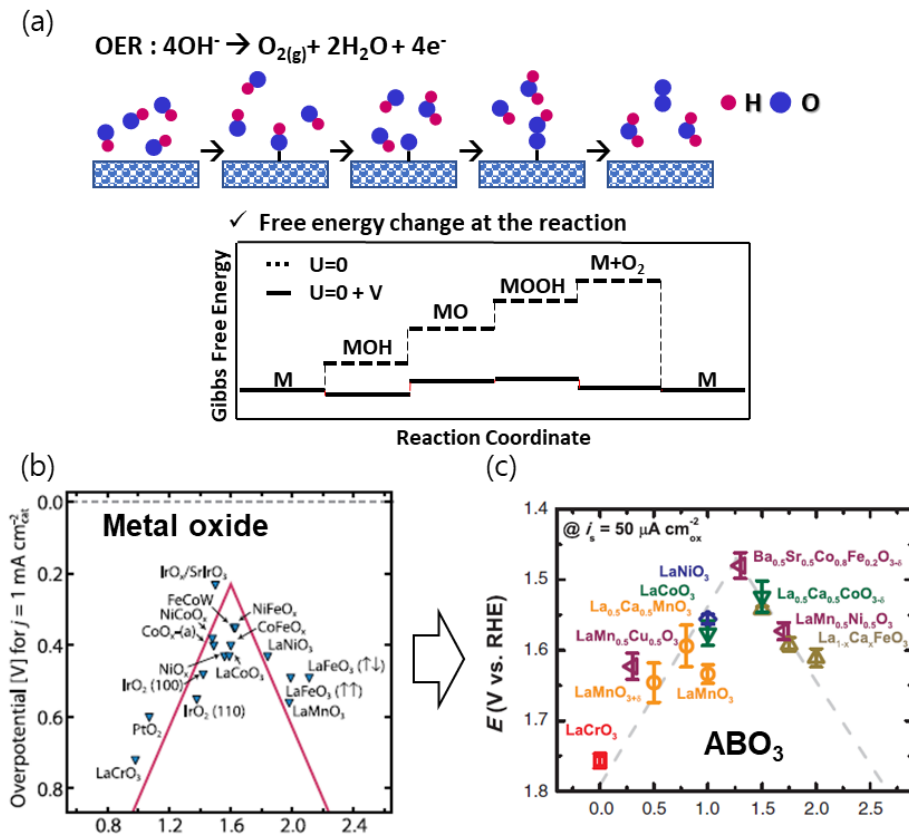


**Figure 8.** (a) Reaction steps in OER on the surface of catalyst (b) Volcano plot for metal oxides and (c) perovskite oxide in OER [2, 12]

## CHAPTER 3. EXPERIMENTAL PROCEDURE/PARAMETER

### 3.1 Overpotential ( $\eta$ ) and Tafel Slope

For the typical electrochemical reactions, total overpotential has three parts. They are concentration overpotential ( $\eta_c$ ), activation overpotential ( $\eta_a$ ), and the resistance overpotential ( $\eta_r$ ). Resistance in third one is between the electrolyte and surface, called uncompensated resistance. When the reactions start at the electrode, participating of the ions in electrolytes in reaction can cause rapid decrease in concentration near the surface, which is the concentration overpotential. Stirring the solution can minimize this kind of overpotential. Material's own catalytic activity is related to the activation overpotential, and it can be changed from one material to another. That's why it can be reduced by selecting an effective electrocatalyst. Ohmic drop compensation is used for removing the resistance overpotentials. Manually it can be calculated to multiply the current density (at uncompensated resistance) and corresponding potential. It is also called the  $iR$  drops, required to be subtracted from the measured one. Resultant overpotentials is expressed by followed equation:

$$\eta = (\Delta G / e) - 1.23 \text{ V} = \eta_c + \eta_a + \eta_r$$

Typically, the Tafel plot of an electrocatalyst is calculated by replotting the linear sweep voltammetry (LSV) with  $\log(j)$  versus overpotential. This term makes up for overpotential in expressing catalytic activity of the electrocatalyst. Tafel slop, the slope of the linear part in Tafel plot is related to charge transfer in certain potential range. Related equation is as followed:

$$\text{Tafel slop: } d \log(j) / d\eta = 2.303RT / \alpha nF$$

$R$  (ideal gas constant),  $T$  (temperature),  $\alpha$ : charge transfer coefficient,  $F$  (Faraday constant),  $n$  (number of electrons transferred). In this equation, only  $\alpha$  is variable, means an electrocatalyst with higher Tafel slope possesses an inferior charge transfer ability. For more accuracy, non-Faradaic region, which is not related to catalytic reaction, should be removed in replotting Tafel plot from the polarization curves.

### 3.2 How to evaluating experimentally observed current

Many of paper reports current divided by geometric surface area of the electrodes (in the unit of  $\text{A}/\text{cm}_{\text{geo}}^2$ ). However, under this method we cannot tell the intrinsic ability of the



given electrocatalyst. So there are several methods, which can express normalizing current measured in water splitting reactions. [13] First one is current calculated by the geometrical area of the given electrode (in units of  $A/cm_{geo}^2$ ). It is mainly used, but it cannot show intrinsic activity of the electrocatalyst materials, for different catalyst loading varies current density and actual surface layer is not different from projection area. But in very thin layer or flat electrode, it is relatively precise.

For showing intrinsic activity, there are two methods normalizing the measured current. One is using ECSA – Electrochemical surface area (in this case, the unit is  $A/cm_{ECSA}^2$ ) as shown in Figure 9. ECSA reflects the actual surface of the electrode, different from geometrical surface area. But it can be significantly different from one to another by using cyclic voltammetry and impedance measurement, which can induce potential error. The other is current normalized by Brunauer–Emmett–Teller (BET) surface area. BET measurement is determined by adsorption and desorption of the gases. It is especially powerful method in case of porous and nano-structuring materials. But gas adsorption/desorption sites and electrochemical active sites are not the same, which leads to experimental inaccuracy.

Mass activity is the current divided by catalyst loading (in the unit of  $A/g$ ). It directly considers the loading of the catalyst at all types of catalyst. But it depends on density, particle size, morphology.

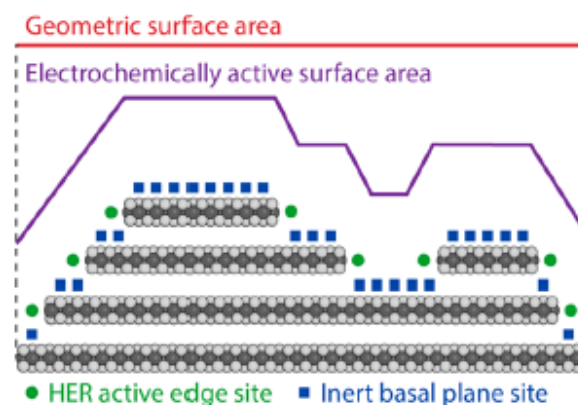


**Figure 9.** Simple schematics explaining geometrical/electrochemically active surface area in  $MoS_2$  [14]

### 3.6 References

- [1] X. Zou, Y. Zhang, Noble metal-free hydrogen evolution catalysts for water splitting, *Chem Soc Rev* 44(15) (2015) 5148-80.
- [2] Z.W. Seh, J. Kibsgaard, C.F. Dickens, I. Chorkendorff, J.K. Norskov, T.F. Jaramillo, Combining theory and experiment in electrocatalysis: Insights into materials design, *Science* 355(6321) (2017).
- [3] Y. Zhu, W. Zhou, Z.G. Chen, Y. Chen, C. Su, M.O. Tade, Z. Shao, SrNb(0.1)Co(0.7)Fe(0.2)O(3-delta) perovskite as a next-generation electrocatalyst for oxygen evolution in alkaline solution, *Angew Chem Int Ed Engl* 54(13) (2015) 3897-901.
- [4] J.D. Benck, T.R. Hellstern, J. Kibsgaard, P. Chakthranont, T.F. Jaramillo, Catalyzing the Hydrogen Evolution Reaction (HER) with Molybdenum Sulfide Nanomaterials, *ACS Catalysis* 4(11) (2014) 3957-3971.
- [5] Y. Li, H. Wang, L. Xie, Y. Liang, G. Hong, H. Dai, MoS<sub>2</sub> nanoparticles grown on graphene: an advanced catalyst for the hydrogen evolution reaction, *J Am Chem Soc* 133(19) (2011) 7296-9.
- [6] H. Wang, Z. Lu, S. Xu, D. Kong, J.J. Cha, G. Zheng, P.C. Hsu, K. Yan, D. Bradshaw, F.B. Prinz, Y. Cui, Electrochemical tuning of vertically aligned MoS<sub>2</sub> nanofilms and its application in improving hydrogen evolution reaction, *Proc Natl Acad Sci U S A* 110(49) (2013) 19701-6.
- [7] H. Sun, Z. Hu, X. Xu, J. He, J. Dai, H.-J. Lin, T.-S. Chan, C.-T. Chen, L.H. Tjeng, W. Zhou, Z. Shao, Ternary Phase Diagram-Facilitated Rapid Screening of Double Perovskites As Electrocatalysts for the Oxygen Evolution Reaction, *Chemistry of Materials* 31(15) (2019) 5919-5926.
- [8] Y. Zhu, L. Zhang, B. Zhao, H. Chen, X. Liu, R. Zhao, X. Wang, J. Liu, Y. Chen, M. Liu, Improving the Activity for Oxygen Evolution Reaction by Tailoring Oxygen Defects in Double Perovskite Oxides, *Advanced Functional Materials* 29(34) (2019).
- [9] M.A. Lukowski, A.S. Daniel, F. Meng, A. Forticaux, L. Li, S. Jin, Enhanced hydrogen evolution catalysis from chemically exfoliated metallic MoS<sub>2</sub> nanosheets, *J Am Chem Soc* 135(28) (2013) 10274-7.



- [10] S. She, Y. Zhu, Y. Chen, Q. Lu, W. Zhou, Z. Shao, Realizing Ultrafast Oxygen Evolution by Introducing Proton Acceptor into Perovskites, *Advanced Energy Materials* 9(20) (2019).
- [11] E. Skulason, V. Tripkovic, M.E. Bjorketun, S. Gudmundsdottir, G. Karlberg, J. Rossmeisl, T. Bligaard, H. Jonsson, J.K. Norskov, Modeling the Electrochemical Hydrogen Oxidation and Evolution Reactions on the Basis of Density Functional Theory Calculations, *Journal of Physical Chemistry C* 114(42) (2010) 18182-18197.
- [12] H. Yu, F. Chu, X. Zhou, J. Ji, Y. Liu, Y. Bu, Y. Kong, Y. Tao, Y. Li, Y. Qin, A perovskite oxide with a tunable pore-size derived from a general salt-template strategy as a highly efficient electrocatalyst for the oxygen evolution reaction, *Chem Commun (Camb)* 55(17) (2019) 2445-2448.
- [13] S. Anantharaj, S.R. Ede, K. Sakthikumar, K. Karthick, S. Mishra, S. Kundu, Recent Trends and Perspectives in Electrochemical Water Splitting with an Emphasis on Sulfide, Selenide, and Phosphide Catalysts of Fe, Co, and Ni: A Review, *ACS Catalysis* 6(12) (2016) 8069-8097.
- [14] J.D. Benck, T.R. Hellstern, J. Kibsgaard, P. Chakthranont, T.F. Jaramillo, Catalyzing the Hydrogen Evolution Reaction (HER) with Molybdenum Sulfide Nanomaterials, *ACS Catalysis* 4(11) (2014) 3957-3971

## CHAPTER 4. HIGHLY ACTIVE OXYGEN ELECTROCATALYST BASED ON N-DOPED GRAPHENE QUANTUM DOT FUNCTIONALIZED PEROVSKITE

### 4.1 Introduction

Under fossil fuel-based systems, greenhouse effect and exhaustion of resource is a major concern, novel energy source which are environmentally clean and abundant, is becoming needed. Water splitting can produce hydrogen, one of the promising candidates by clean and renewable ways. To split water efficiently, electrochemical oxygen evolution reaction (OER) is the main process [1–4]. However, the OER can be a bottleneck, which is more complex reactions, related to four-electron transfer process, compared with HER. Till now, noble metal such as Ir, Ru based oxides are the best OER catalyst to achieve high current density at low overpotential for water splitting, but scarcity and expensive costs of them prevent application in large-scale and industrial uses. [5, 6] To replace them, lots of study were conducted focusing on non-noble metal such as transition metal (Co, Cu, Ni) based compounds, etc. [7-11]

Among various non-noble metal compounds, perovskites oxides with chemical composition of  $ABO_3$  (A: alkaline or rare earth metal, B: transition metal ) have high flexibility of structures and compositions, showing the great potentials for tuning their electronic, chemical and catalytic properties, [12-14] attracts many attentions. Among them,  $La_xSr_{1-x}CoO_3$  have received many attentions as a highly active catalyst.

Hierarchically porous perovskite  $La_{0.5}Sr_{0.5}CoO_3$  was synthesized by electrospinning showing highly active OER performances, good rate capability, excellent stability in a Li-O<sub>2</sub> batteries. [15] J. Tyler et al. present OER electrocatalyst containing high mass activity and specific activity at room temperature by substitution of  $Sr^{2+}$  ions and control of oxygen vacancies. [16] By combining experimental and calculation methods, Seo. Et al. studied highly active OER perovskite oxides to modify the chemical composition for tuning the adsorption energy of oxygens on the surface of the catalysts. [17]

Among various carbon nano materials studied, graphene quantum dots (GQDs) have been emerging widely in research field due to its facile charge transfer, good adhesion to catalyst, high surface area, etc. [18-19] Li et. al. reported carbon quantum dots functionalized perovskite oxide-based nanofiber to show superior OER performances compared with commercial  $IrO_2$ . [20] Synergistic effect of perovskite oxide and carbon nanomaterials can

induce highly effective electrocatalyst for OER due to increased surface area and oxygen vacancies. In addition, by introducing heteroatoms such as nitrogen into the carbon mother materials has been considered as a versatile and effective strategy for controlling their electron density and defects, showing better catalytic performances. [21] Also, nitrogen containing polymer, dopamine was functionalized on the perovskite oxide nanorods for highly active OER catalyst. [22]

In this study, we modified perovskite oxide  $\text{La}_{0.5}\text{Sr}_{0.5}\text{CoO}_3$  (LSCO) with N-doped graphene quantum dot (N-GQD) functionalized as an effective electrocatalyst for oxygen evolution reactions (OER). LSCO particles were synthesized by sol-gel method, before divided into smaller particles by using ball-milling process. N-GQD was made by facile hydrothermal methods and mixed with perovskite oxides for synthesizing composite catalyst. Graphene Quantum Dot (GQD) was also functionalized on the LSCO for comparing hetero-atom doped GQD to study effect of modification in detail. It showed good performances comparable with well-known OER electrocatalyst  $\text{IrO}_2$ . By functionalized with N-GQD, electron transferred from LSCO to N-GQD with maintaining the electroneutrality, which changed electronic structure of LSCO for highly active OER catalyst. Also N-GQD was acted as an active site for OER and formed p-n junction with LSCO for better charge transfer.

## 4.2 Experimental details

### 4.2.1 Synthesis and ball-milling of Perovskite oxide

Perovskite oxide  $\text{La}_{0.5}\text{Sr}_{0.5}\text{CoO}_3$  (LSCO) was synthesized by conventional sol-gel process. Citric acid and appropriate ratio of La, Sr, Co based precursors were mixed in deionized water (D.I. water) to form a homogenous solution. All the reagents were totally dissolved, before adding polyethylene glycol (Molecular weight is about 400). After stirring a solution for overnight, as-formed solution was heated at  $300^\circ\text{C}$ , before pre-calcined at  $600^\circ\text{C}$  for several hours and annealed at  $950^\circ\text{C}$  for 4 hours.

In addition, we synthesized  $\text{LaNiO}_3$  perovskite oxides with novel methods in low temperature. It was synthesized by using cyano-gel complex and strong oxidant such as  $\text{H}_2\text{O}_2$ . La precursor (nitrate or chloride) was mixed with D.I. water for complete dissolution. Nickel cyanide was mixed with potassium cyanides for dissolution in water by considering coordination number of cyano-functional group on the Ni atoms, respectively. After both

solutions were mixed, strong oxidizer  $\text{H}_2\text{O}_2$  (Concentration should be lower due to prevention of high reactions rate) were added to form a cyano-gel. After vigorous mixing, centrifugation was repeated 5 times to remove byproducts such as potassium, cyanides. Muffle furnace was used to anneal the gel at 500, 600, 700, 800, 900 °C for 6 hours. Samples without oxidative treatment was made to study effect of oxidizer on the crystallization temperature. To increase the number of active sites, LSCO was ball-milled for nanoparticle using a machine of 8000D Mixer/Mill. By varying processing time, optimized condition as an effective catalyst was found.

#### **4.2.2 Synthesis of the N-doped graphene quantum dots, and the N-GQD functionalized LSCO**

The N-GQD quantum dots were synthesized by a simple hydrothermal process. Appropriate amount of dopamine hydrochloride and citric acid were dissolved in an ethanol, then the solution was transferred into a Teflon-lined stainless-steel autoclave. The sealed autoclave was put in a drying oven at 180 °C for several hours and was kept for cooling until room temperature naturally. The N-GQD dispersion was centrifuged several times at 5,000 rpm for 10 min. Every time the supernatant was removed and remnant was filtered by a membrane filter (0.22  $\mu\text{m}$ ). Graphene quantum dots were also made by same procedure only not with adding dopamine hydrochloride for studying role of N doping.

And as-prepared dispersion of N-doped graphene quantum dots (50, 100, 300, 500, 1,000  $\mu\text{L}$ ) was added to a 10mg/ml dispersion of ball-milled LSCO, before bath-sonication for 15 min and stirring for 1 day. To find optimum condition, linear sweep voltammetry was measured with changing ratio of N-GQD dispersion and LSCO powder as shown in Figure 10. Total process is briefly shown in Figure 11.

#### **4.2.3 Material characterization**

Scanning electron microscopy images were obtained by using a scanning electron microscope (Nova NanoSEM). X-ray diffraction (XRD) patterns were measured by a Normal X-ray diffractometer (Bruker AXS D8 ADVANCE) using  $\text{Cu K}\alpha$  radiation. Transmission electron microscopy (TEM) and Fast Fourier transform (FFT) images were collected using a transmission electron microscope (Tecnai G2 F20 X-Twin). The TEM samples was prepared by dropping 2-propanol dispersion of catalytic materials on the Au coated grid. For

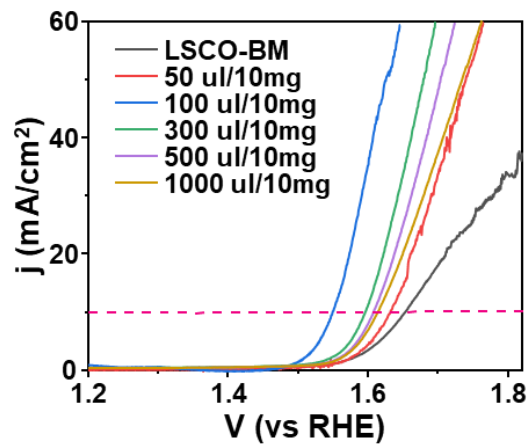


**Figure 10.** Linear sweep voltammetry (LSV) polarization curves of LSCO-NG with varying ratio of NGQD and LSCO

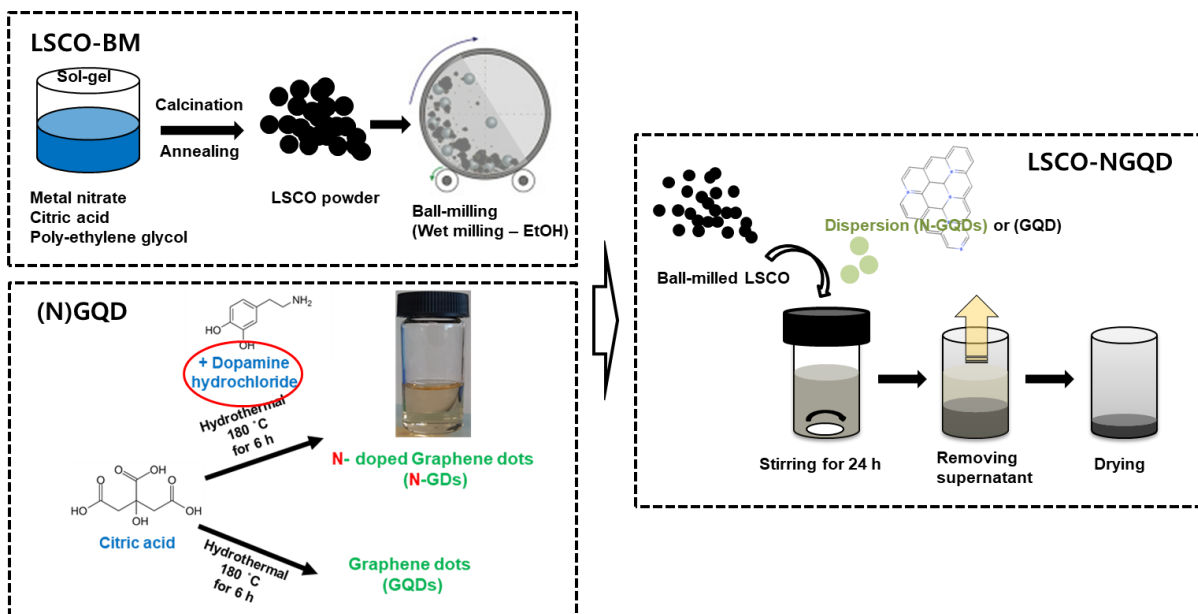


**Figure 11.** Schematics of synthesizing N-doped graphene quantum dot (N-GQD) functionalized  $\text{La}_x\text{Sr}_{1-x}\text{CoO}_3$  (LSCO)

analyzing the bonding states of each elements, X-ray photoelectron spectroscopy (XPS) was performed by Thermo Fisher ESCALAB 250XI to confirm the chemical bonding information. The XPS sample was prepared immediately after synthesizing powder and stored in a desiccator to prevent exposure to air and humid in an atmosphere.

#### 4.2.4 Electrochemical measurement

To measure electrochemical activity of the catalyst, the catalyst ink was prepared by dispersing a powder in a solution containing binder and solvent. 50 mg of the powder was in a 5 ml solution (Ethanol:IPA (isopropyl alcohol):5wt% Nafion=45 %:45%:10%, volumetric portion). After sonication (bath type) process, 2.5 ul catalytic ink was dropped on the glassy carbon electrode (GCE), drying naturally at room temperature in an air. Catalytic films were formed on the 0.07 cm<sup>2</sup> of area on the GCE, loading is 0.35 mg/cm<sup>2</sup>. Then, OER electrochemical measurements were performed by using IVIUM Stat (US). Catalyst films on GCE, a Pt wire, and an Ag/AgCl electrode were used as a working, counter, and reference electrode, respectively. All potentials related to this study were converted to the RHE ( $E_{\text{RHE}} = E_{\text{Ag/AgCl}} + 0.1976 + 0.0592 \times \text{pH}$ ). Electrolytes was 1M KOH aqueous solution full of nitrogen before measurement. The linear sweep voltammetry curves were obtained at a scan rate of 10 mV/s and a rotating speed of 1000 rpm with iR (current x internal resistance) correction. Electrochemical Impedance Spectroscopy (EIS) was performed in the same configuration at the frequency from 10<sup>5</sup> to 0.1 Hz with an AC voltage amplitude of 10 mV at a voltage of 1.8 (vs RHE).

#### **4.2.5 Electrochemical reduction of the catalyst electrode**

After forming catalyst electrode, it was dipped into the electrolyte for post-treatment, that is electrochemical reduction. The electrochemical reduction was carried out by applying a negative voltages of 0.2236 to 0.8236 V (vs RHE) with steps of 0.2V for 20 min in alkaline solution, OER activities were compared for LaNiO<sub>3</sub> (LNO) films subjected to the electrochemical reduction by applying a negative voltage of 0.8236 V (vs RHE) on the film for a time intervals of 2, 5, 10, 20, 30 min to see optimal condition. After electrochemical reduction, as-treated films were electrochemically measured in a same electrolyte, 1M KOH with N<sub>2</sub> saturation.

### **4.3 Results and Discussion**

#### **4.3.1 Ball-milling of perovskite oxide for optimization of the electrocatalyst**

The effect of ball-milling on the material properties and the OER activity of the LaSrCoO<sub>3</sub> (LSCO) perovskite was studied. Ball-milling has been reported as an efficient and



simple treatment method to enhance the OER performance of oxide catalyst.[23, 24] To raise the specific surface area of the materials, the ball-milling process is commonly used. Experimental results showed that the ball-milling process can remarkably improve the LSCO OER performance. This enhancement is related to the reducing size of agglomerates by the ball-milling process, as confirmed by dynamic laser scattering (DLS) and SEM.

However, severe ball-milling process can damage the crystallinity and surface properties of the materials. So optimization of ball-milling condition should be needed. Various physicochemical characterization has been used to study the morphology and crystallinity of the ball-milled perovskite oxides. We considered two parts of the electrocatalyst. One is total electrode activity, the other is intrinsic catalytic performances. Before mentioned, there are several methods to express the measured current to show electrochemical performances. Most used one is current density, which is measured current divided by geometrical surface area. In our study, we used specific activity to show intrinsic properties of the catalyst. To determine the surface area, we have used electrochemical surface area (ECSA) by measuring cycle voltammetry with varying scan rate.

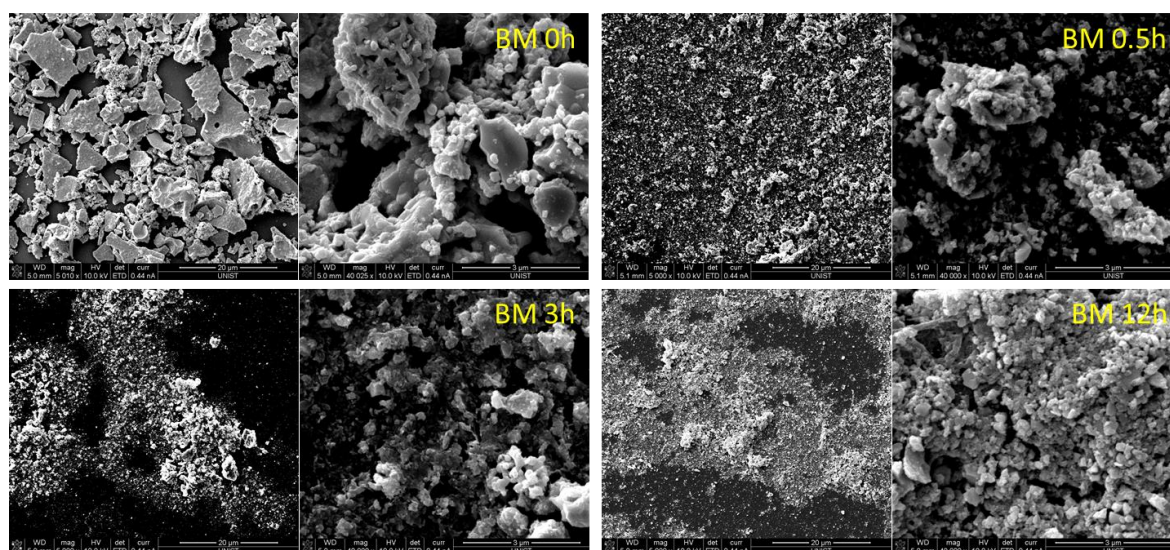


**Figure 12.** SEM images of perovskite oxide ( $\text{La}_{0.5}\text{Sr}_{0.5}\text{CoO}_3$ ) after ball-milling process by changing processing time (a) pristine samples (without ball-milling). Samples ball-milled for (b) 0.5 hours (c) 3 hours, (d) 12 hours. Perovskite oxide particles were mixed with ethanol, before pulverized by wet ball-milling.

First SEM and DLS was measured to see particles size distribution and morphology of the catalyst. As seen in Figure 12, the particles were pulverized as ball-milling time increases.

Before ball-milling particles are over several micro-size, which aggregates during high temperature annealing process. But the size of the catalyst dramatically decreased in only 30 minutes after ball-milling. As processing times increases, particles became smaller. Dynamic laser scattering was used (Figure 13) to know the quantitative size of particles, after sample was prepared by dispersing nanoparticles in ethanol. Similar to experimental results by SEM measurement, the size of the LSCO was reduced as process goes on. Size of pristine perovskite oxide particles were over 350 nm, but it reduces to under 100 nm. At initial steps, it decreased rapidly, and the size was saturated over several hours. Standard deviation in size distribution of each samples was over 50 nm, it may be due to re-agglomeration of nano particle in ethanol.

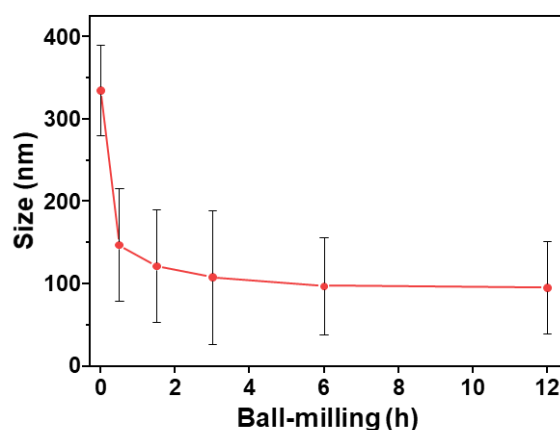


**Figure 13.** Size of perovskite oxide particles by wet ball-milling by varying processing time. Data was acquired by dynamic laser scattering (DLS). Concentration of the sample was 0.1 mg in 1 ml ethanol. Standard deviation was inserted in the graph at each condition.

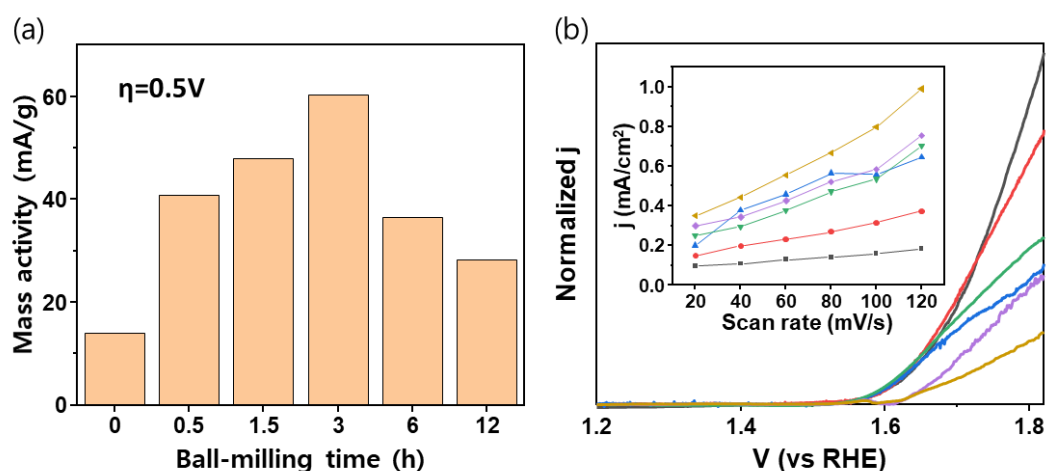


**Figure 14.** (a) Mass activity (MA) based on the catalyst weight of each ball-milled LSCO catalyst at an overpotential of  $\eta=0.5$  V and (b) Specific activity of ball-milled LSCO, in which



surface area was ECSA (Electrochemically active surface area). Inset graph was difference in current density measured by cyclic voltammetry with varying scan rates. ECSA was evaluated by calculating double-layer capacitance values derived from linear fitting curves.

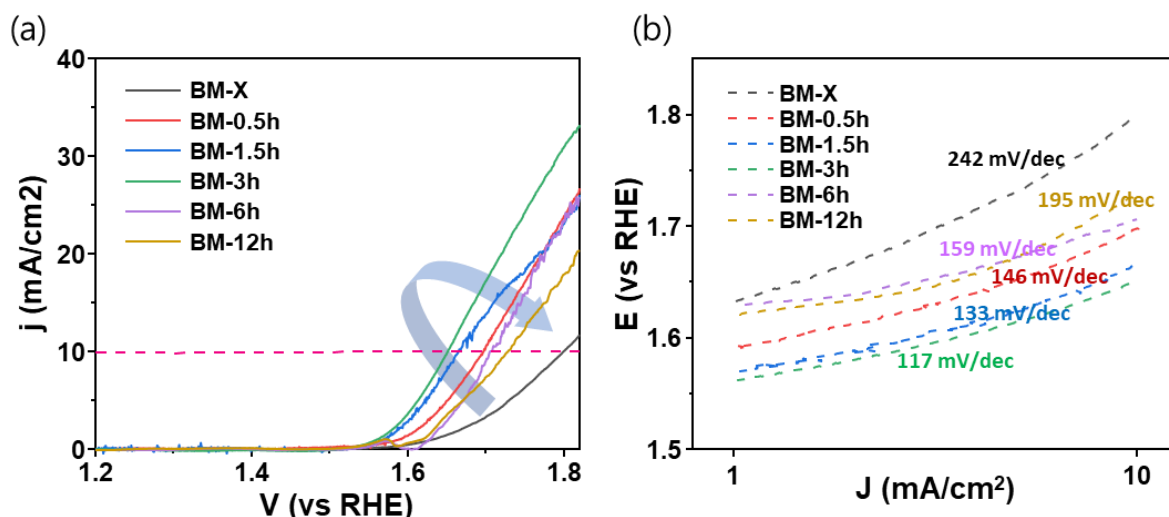


**Figure 15.** (a) Linear sweep voltammetry (LSV) polarization curves in 1.0 M KOH of ball-milled LSCO with different processing time. Arrow shows trend of the ballmilling time to OER performances and (b) corresponding Tafel plot.

As seen in Figure 14, mass activity of ball-milled LSCO catalyst was induced by dividing measured current by catalyst loadings at fixed potential of 0.5V (vs RHE). Among the all the samples, 3h ball-milled samples showed the highest mass activity. It might be due to more active sites and less damaged catalytic sites. In inset of Figure 14 (b), ECSA was the highest in 12 h ball-milled LSCO. The sequence of ECSA was (ball-milled) 12h – 6h – 3h – 1.5h – 0. This trend exactly corresponds to ball-milling time. Like SEM and DLS data in Figure 12, 13, the size of particles reduced as ball-milling process went to have higher surface area. However specific activity normalized by ECSA as shown in Figure 14 (b) was different, which shows intrinsic activity of the catalyst. It showed ball-milling gradually damaged the materials catalytic activity. Briefly ball-milling caused high surface area but deteriorated the intrinsic activity of each active sites. So it is required to consider two effects induced by ball-milling.

The electrocatalytic OER performances of the LSCO films on the glassy carbon electrode were evaluated in a N<sub>2</sub> saturated alkaline electrolyte (1M KOH, pH = 14). To evaluate the electrocatalytic activity toward OER, the current density versus potential at a scan rate of

10 mV/s was measured recorded at room temperature as a function of ball-milling time, plotted in Figure 15. For the pristine LSCO sample, a current density of  $-10 \text{ mA/cm}^2$  was achieved at an overpotential ( $\eta$ ) of 570 mV vs reversible hydrogen electrode (RHE). The overpotential decrease to 420 mV at 3 h ball-milled sample, then gradually increases to 500 mV at 12 h ball-milled ones. This tendency is same in Tafel slop as shown in Figure 15 (b).

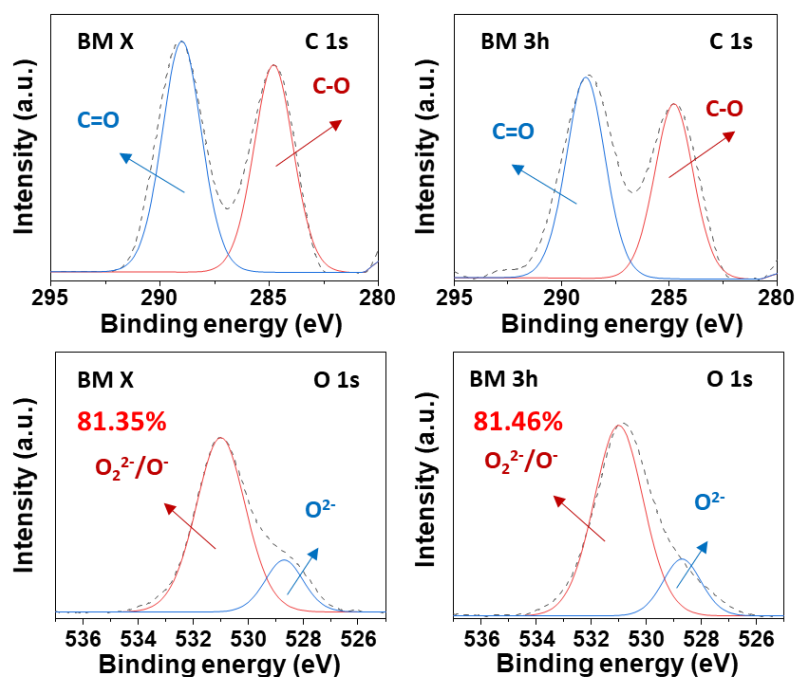


**Figure 16.** XPS spectra of C 1s and O 1s for pristine and ball-milled (3 h) LSCO samples

As seen in Figure 16 and 17, chemical bonding state of each elements was maintained after ball-milling of LSCO. XPS spectra of C 1s and O 1s showed little peak shift and changes in ratio of the bonding. C 1s in XPS data has two peaks, C-C at 285 eV and C-O bonding at 288.6 eV, O 1s spectra showed lattice oxygen at lower binding energy and oxidant states of oxygen ( $\text{O}^{2-}/\text{O}_2$ ), which is related to oxygen vacancy, may influence the OER performances. [25]. Ratio of  $\text{O}^{2-}$  to  $\text{O}^{2-}/\text{O}_2$  was almost same, 0.8135 in pristine LSCO and 0.8146 in 3h ball-milled LSCO, respectively. Bonding states of cobalt was also maintained after ball-milling of 3 hours, for binding energy of the peak and FWHM was almost same in both samples in Figure 17.

In Figure 18, grain size and crystallinity of the two samples was confirmed by XRD patterns. And crystallinity was reduced as peak intensity was reduced as shown in Figure 18 (a), full-width half maximum (FWHM) are 0.169 in pristine LSCO, 0.321 in 3h ball-milled

LSCO. By Scherrer equation, grain size of ball-milled samples was almost 2 times smaller than pristine LSCO.

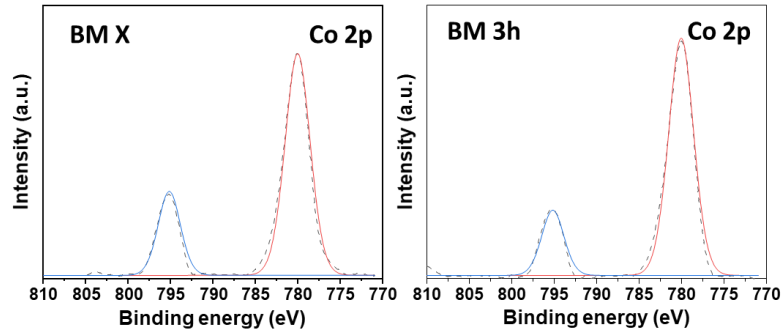


**Figure 17.** XPS spectra of Co 2p for pristine and ball-milled (3 h) LSCO samples.

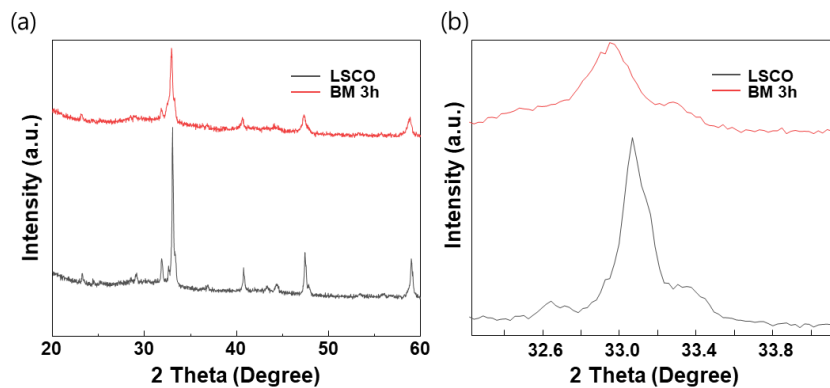


**Figure 18.** XRD patterns of pristine and ball-milled (3 h) LSCO samples (a) in range of  $20^\circ \sim 60^\circ$  and of (b)  $32^\circ \sim 34^\circ$ .

#### 4.3.2 Functionalization of N-Graphene Quantum Dot $\text{La}_{0.5}\text{Sr}_{0.5}\text{CoO}_3$

Graphene quantum dots (GQDs) have attracted many attentions in diverse rising applications due to their electrical and optical properties induced from nano-meter scale, these days. Especially, smaller ( $< 10 \text{ nm}$ ) GQDs exhibit larger bandgap, higher carrier mobility and more reactive sites, which is more attractive for various applications. In the field of electrocatalyst for water splitting, nitrogen doped carbon nanomaterials are expected to have a great potential for both half reactions.

In this section, perovskite oxide  $\text{LaSrCoO}_3$  (LSCO) was modified with N-doped graphene quantum dot (N-GQD) functionalized as an effective electrocatalyst for oxygen evolution reactions (OER). N-GQD was made by facile hydrothermal methods and functionalization of it on the LSCO was realized by only mixing with perovskite oxides for efficient composite catalyst. Graphene Quantum Dot (GQD) was also synthesized for comparing with hetero-atom doped GQD to study effect of modification in detail.

As shown in Figure 19, XRD patterns of LSCO, ball-milled LSCO, N-GQD and GQD functionalized LSCO were shown. Although rest of 3 samples except LSCO shows a little lower peak intensity and wider full-width and half maximum (FWHM), they maintained crystallinity confirmed by no peak shift.

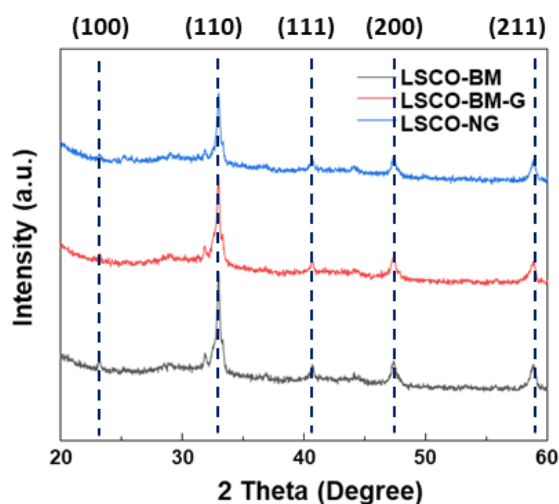


**Figure 19.** XRD patterns of LSCO, LSCO-BM, LSCO-QD, LSCO-NG samples

The N-GQDs were initially prepared by mixing dopamine and citric acid under hydrothermal condition. As-synthesized N-GQDs have several nanometer-size and high crystallinity with 0.21 nm lattice spacing corresponding to the (100) plane confirmed by TEM images in Figure 20. GQD and N-GQD functionalized LSCO composite (LSCO-GQD and LSCO-NG, respectively) was synthesized via a facile solution process as mentioned before.

As shown in TEM images of Figure 21, the N-GQDs were uniformly distributed on the outer space of the LSCO NPs. In the highly magnified image, N-GQDs and LSCO NP exhibited high crystallinity, as confirmed by the lattice-fringe of 0.26 nm and 0.21 nm, which means (100) plane of LSCO and (100) plane of N-GQDs, respectively. Corresponding fast Fourier transform (FFT) patterns also showed good crystallinity of the samples. Interestingly, N-doped

graphene rings were visualized by enlarged TEM images. In case of N-doped graphene, the distance between adjacent carbon atoms is 0.14, 0.24. It was visualized clearly in TEM images with higher magnification in Figure 21.

Similarly, GQD was distributed on the surface of the LSCO as shown in Figure 20. GQD and LSCO also showed high crystallinity as confirmed by lattice spacing of 0.21 nm and 0.37 nm, corresponding to (100) plane of GQD and (110) plane of LSCO.

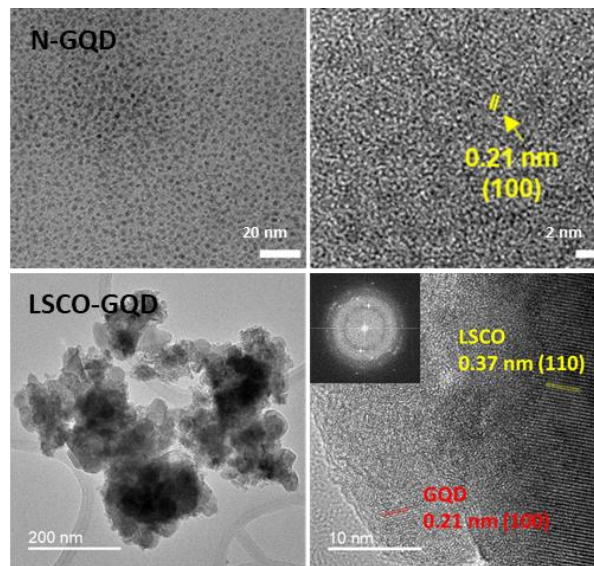


**Figure 20.** TEM (with higher magnification) and FFT images of N-GQD and LSCO-GQD NPs.

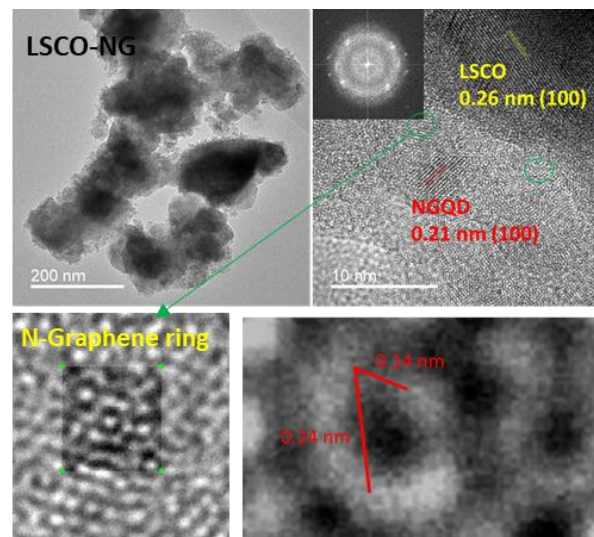


**Figure 21.** TEM (with higher magnification) and FFT images of LSCO-NG NPs.

The OER activities of the functionalized LSCO films on the glassy carbon electrode were measured under alkaline electrolyte (1.0 M KOH, pH = 14). To evaluate the OER performance, the current density vs potential (vs RHE) was measured recorded at a scan rate of 10 mV/s as each condition of modification, plotted in Figure 22. For the pristine LSCO sample, a current density of  $-10 \text{ mA/cm}^2$  was achieved at an overpotential ( $\eta$ ) of 520 mV vs reversible hydrogen electrode (RHE). The overpotential decrease to 420 mV at ball-milled samples, then gradually increases to 360 mV after modifying with GQD. The best samples, that is LSCO-NG shows the least overpotential of 320 mV, superior to well-known noble metal-based catalyst,  $\text{IrO}_2$ . To examine the kinetics and charge transfer resistance of each samples, Tafel plot and Nyquist plot were shown in Figure 23 (b), (c). Tendency of corresponding data were coincided with LSV curve.

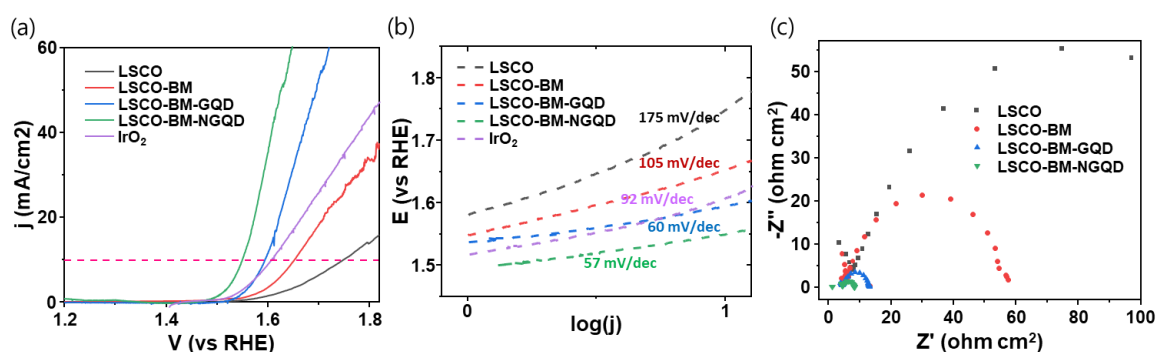


**Figure 22.** (a) Linear sweep voltammetry (LSV) polarization curves of functionalized LSCO with conditions in 1.0 M KOH. (b) Corresponding Tafel plot and (c) Nyquist plot measured at 1.8 V (vs RHE).

### 4.3.3 Mechanism of N-GQD LSCO by analyzing XPS

The chemical composition and surface chemistry of the pristine LSCO, LSCO-GQD and LSCO-NG were analyzed by using XPS. Each result was presented in Figure 24 and 25, respectively. In N-GQD functionalized LSCO, we can observe distinct changes in the C 1s and N 1s spectra, compared with pristine LSCO. In Figure 23, this  $\pi$ - $\pi^*$  shake-up peaks shifting in (N)-GQDs indicates the electron transfer from (N)-GQDs to LSCO, which altered the electronic structure of Co and O, which we can observe from XPS peak in Figure 23 and 24.



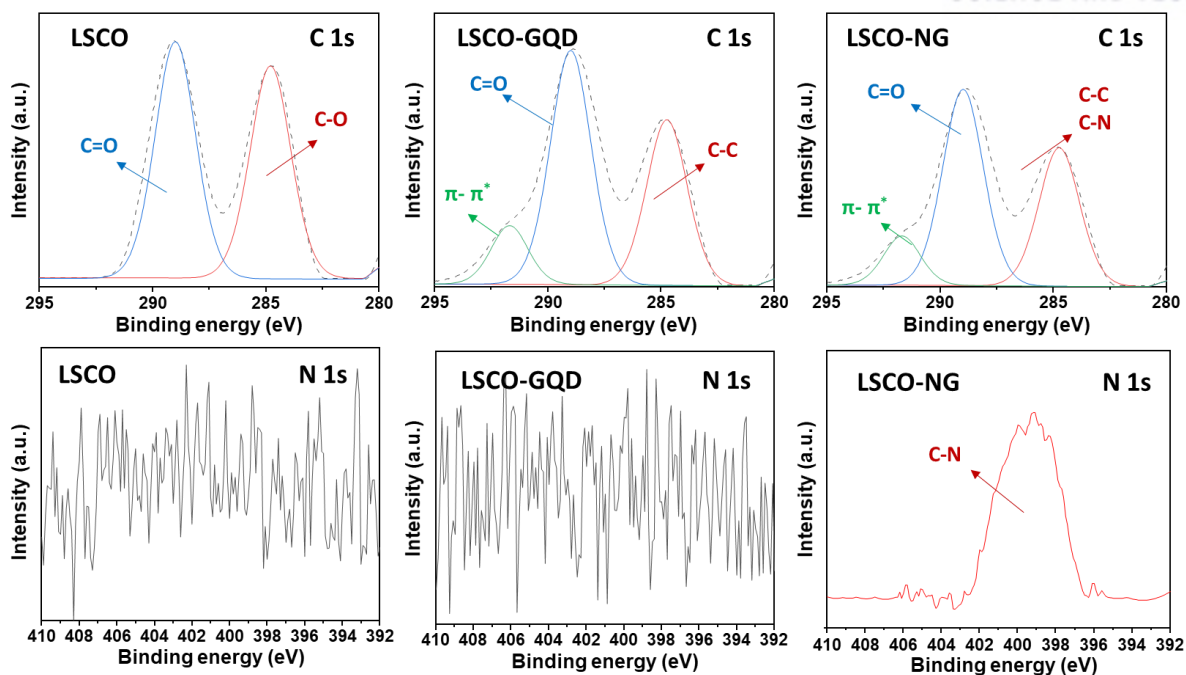


**Figure 23.** XPS spectra of the functionalized LSCO: C 1s, N 1s spectra of LSCO, LSCO-GQD, LSCO-NG

The XPS of Co shows redox ability of materials  $\text{Co}^{2+}$  and  $\text{Co}^{3+}$  species compared to pure LSCO and GQD-LSCO. Surface Co sites of LSCO are more active than surface oxygen sites, suggesting that surface Co sites govern the OER activity. Electron transferred from LSCO to N-GQD, made high electrophilicity for improving the adsorption capability of  $\text{OH}^-$ . [26] Also N-GQD was acted as an active site for OER and formed p-n junction with LSCO for better charge transfer. [27]

O 1s spectra showed lattice oxygen at lower binding energy and oxidant states of oxygen ( $\text{O}^{2-}/\text{O}_2$ ), which is related to oxygen vacancy, may influence the OER performances. Ratio of  $\text{O}^{2-}$  to  $\text{O}^{2-}/\text{O}_2$  was increased in LSCO-NG (0.8653), in LSCO-GQD (0.8591), compared with pristine LSCO (0.8135) for higher OER performances. In case of GQD samples, electronic structure of Co states was not changed without N-doping. In conclusion, N-GQD functionalization induced electron transfer and oxygen vacancy, which was good for the catalytic performances of LSCO for highly active OER electrocatalyst.

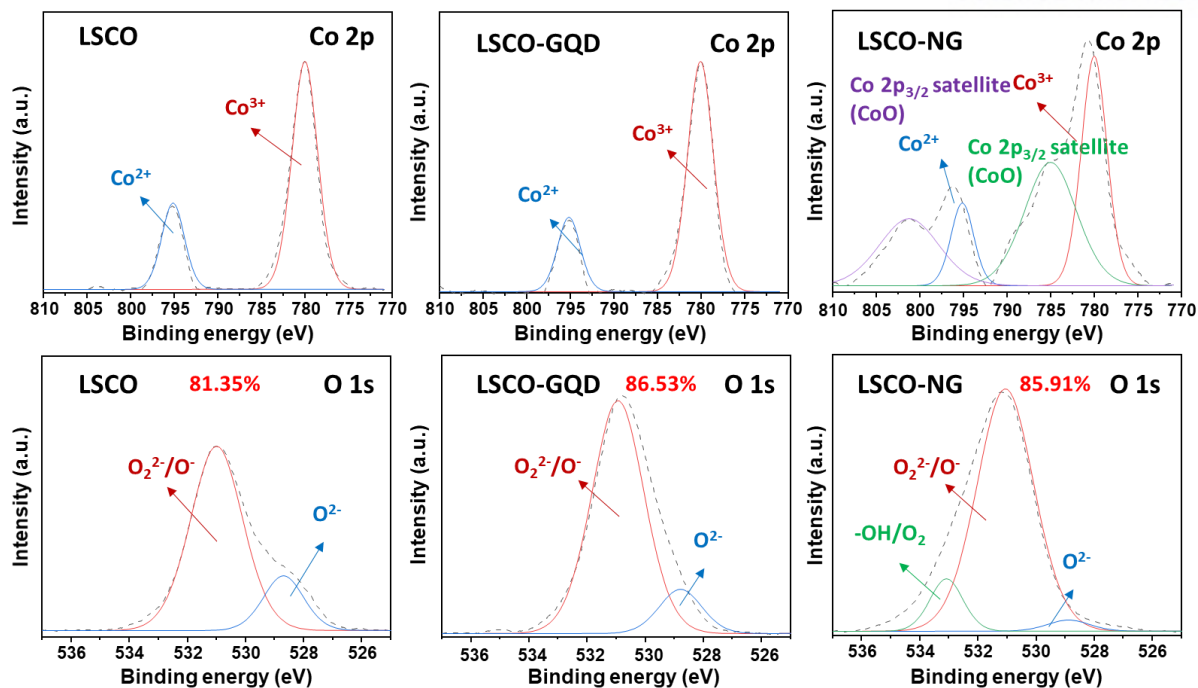


**Figure 24.** XPS spectra of the functionalized LSCO: Co 2p and O 1s spectra of LSCO, LSCO-GQD, LSCO-NG

#### 4.3.4 Synthesis of perovskite under low temperature

Among the various OER electrocatalyst,  $\text{ABO}_3$  perovskite oxide (A: alkaline or rare earth metal, B: transition metal) have been attracting many attentions due to flexible electronic structure, high activity descriptor, good stability, etc. However, conventional synthesis for perovskite oxide such as high-temperature solid-phase method, hydrothermal method has several drawbacks. It results in micro-sized particles, which show inferior catalytic performances and dispersion compared with nano-sized ones. And more element needs higher temperature, which may result in unwanted phase formation.

To solve these problems, we suggest two-steps low temperature synthesis of perovskite oxides using cyanide and superoxide molecular cluster as shown in Figure 25. Each metal precursors are mixed for gelation (hydrolyze), result in cyanide molecular clusters. Next cyanogel precursor forms by adding strong oxidizer such as peroxide. After all the process, post heat-treatment removes byproducts. In thermodynamic viewpoint, polymorph method needs low potential energy compared with conventional high temperature process (Figure 26). Also cyano-gel system using mixed-valence complex is homogeneous and decrease



crystallization energy. Simple and low energy process enables facile composition control, which can increase active-site and reduce OER descriptor energy.

Perovskite oxides are multi-component oxides, which have higher crystallization energy needed over 900°C temperature for synthesis. That's why it needs additional process such as ball-milling for reducing to nano particles. Besides, metals and cyano-group have similar bonding energy with oxygen and Prussia blue (Cyano-group) have also similar crystal structure. We chose cyano-group to synthesize by using coordination complex path for minimizing crystallization energy to have lower process temperature. By using this, LaNiO<sub>3</sub> could be made under 700 °C. As seen in Figure 27. This particle was smaller than conventional ones (~ 70 nm), can have crystallinity at low processing temperature (500°C).

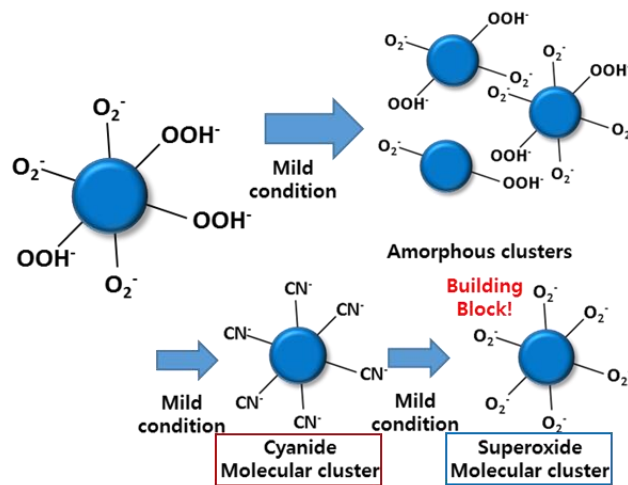


**Figure 25.** Superoxide molecular cluster formation using cyano/superoxide molecular clusters, compared with conventional methods using amorphous clusters.

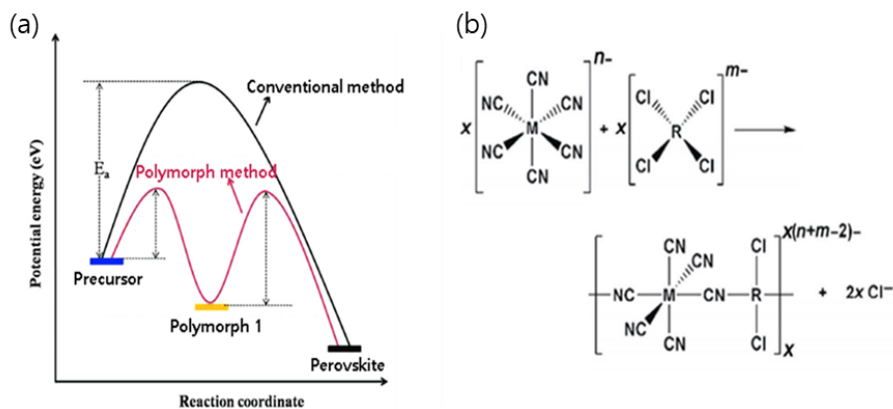


**Figure 26.** (a) Reaction path using polymorph method and (b) cyano-gel based synthesis based on mixed valence complex

XRD pattern of different samples was measured to see the effect of oxidizer on the annealing temperature in terms of crystallization. As seen in Figure 28, without annealing the particles are amorphous with no peaks in XRD data. Compared with conventional sol-gel methods, with H<sub>2</sub>O<sub>2</sub> the sample shows peaks of LaNiO<sub>3</sub> only at 500°C. However, sample without oxidizer, XRD peaks of La<sub>2</sub>O<sub>3</sub> and NiO, (not LaNiO<sub>3</sub>) were shown.

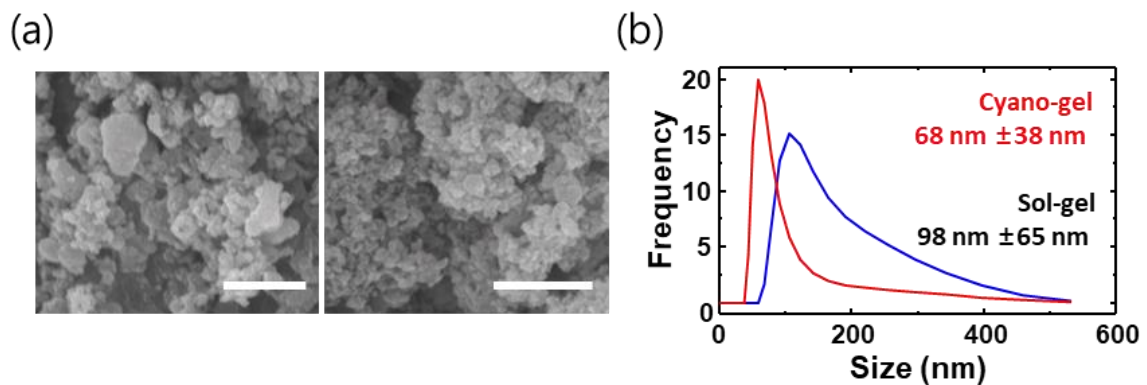


**Figure 27.** (a) SEM images of perovskite oxides synthesized by conventional sol-gel process and cyano-complex route (scale bar: 500 nm) and (b) dynamic laser scattering (DLS) data made by both methods

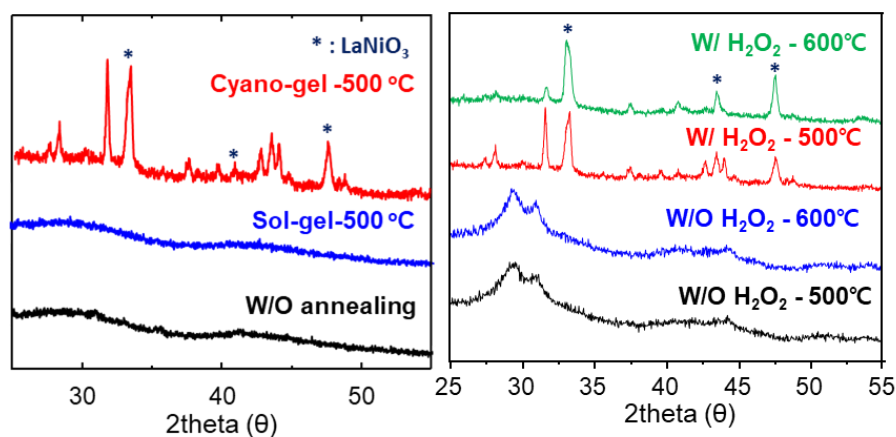


**Figure 28.** XRD data of LaNiO<sub>3</sub> before annealing, after annealing of sol-gel and low temperature process (left) and same materials with post treatment using H<sub>2</sub>O<sub>2</sub> and without adding H<sub>2</sub>O<sub>2</sub> for annealing at 500, 600°C for 6 hours.

### 4.3.5 Electrochemical reduction for formation of oxygen vacancy

Oxygen vacancy has huge effect on the catalytic performances of the electrocatalyst. Annealing in inert atmosphere is one of the most used methods in this case. It makes defects through the bulk of the materials. Electrochemical reduction is more effective methods in surface-related reaction. Zhu. et. studied the effect of each methods on the OER activity of the catalyst. [28] They also suggested that oxygen vacancies generated by varying methods have clearly different characteristics, that is dissimilar effect on the activity of electrodes. Oxygen vacancies were distributed across the bulk of the electrocatalyst formed by thermal annealing, while the electrochemical reduction generates the oxygen vacancies intensely on the surface of the catalyst. The latter method has higher efficiency and easiness, for catalytic activities mainly occurred on the surface, not in the whole bulk of the materials. Like their studied, we used electrochemical reduction to make oxygen vacancies in the low-temperature synthesized  $\text{LaNiO}_3$  thin films, The electrochemical reduction was carried out by applying a negative voltages of 0.2236 to 0.8236 V (vs RHE) with steps of 0.2V on the electrode for a time interval of 2, 5, 10, 20 and 30 min in alkaline solution and in Fig. 18, linear sweep voltammetry was shown according to electrochemical reduction.

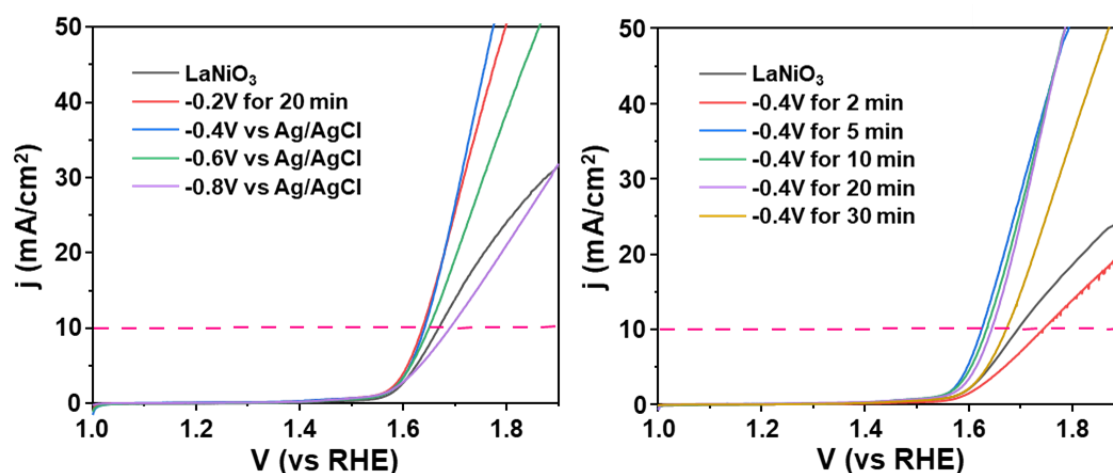


**Figure 29.** (a) Linear sweep voltammetry (LSV) polarization curves of  $\text{LaNiO}_3$  with applying different negative bias in 20 min. for electrochemical reduction in 1.0 M KOH, (b) LSV curves of  $\text{LaNiO}_3$  with different treatment times at -0.4V vs RHE.

For the pristine  $\text{LaNiO}_3$  sample, a current density of  $-10 \text{ mA/cm}^2$  was measured at an overpotential ( $\eta$ ) of 1.67 V vs reversible hydrogen electrode (RHE). The overpotential decrease to 400 mV at  $-0.4\text{V}$  for 20 min. samples. Then optimization of the electrochemical reduction was conducted by changing treatment time at fixed applying potential. At an overpotential of 390 mV at a current density of  $-10 \text{ mA/cm}^2$  was obtained at a 5 minutes-treated samples.

#### 4.4 Conclusion

In this study, we modified perovskite oxide  $\text{La}_x\text{Sr}_{1-x}\text{CoO}_3$  (LSCO) with N-doped graphene quantum dot (N-GQD) functionalized as an effective electrocatalyst for oxygen evolution reactions (OER). LSCO particles were synthesized by sol-gel method, before divided into smaller particles by using ball-milling process. N-GQD was made by facile hydrothermal methods and mixed with perovskite oxides for synthesizing composite catalyst. Graphene Quantum Dot (GQD) was also synthesized for comparing hetero-atom doped GQD to study effect of modification in detail. For the pristine LSCO sample, a current density of  $-10 \text{ mA/cm}^2$  was achieved at an overpotential ( $\eta$ ) of 510 mV vs reversible hydrogen electrode (RHE). The overpotential decrease to 420 mV at ball-milled samples, then gradually increases to 360 mV after modifying with GQD. The best samples, that is LSCO-NG shows the least overpotential of 310 mV, superior to well-known noble metal-based catalyst,  $\text{IrO}_2$ . By TEM and XPS, N-GQD and GQD was functionalized well on the surface of LSCO. By the functionalization of GQD and N-GQD, O 1s spectra showed lattice oxygen at lower binding energy and oxidant states of oxygen ( $\text{O}^{2-}/\text{O}_2$ ), which show oxygen vacancy, influences the OER performances. Higher oxidant states induce better OER catalytic activities. And only N-GQD modified samples changes in Co 2P chemical states for better OER performances. The chemical composition and surface chemistry of the pristine LSCO, LSCO-GQD and LSCO-NG were analyzed by using XPS. Each result was presented in Figure 24 and 25, respectively. In N-GQD functionalized LSCO, we can observe distinct changes in the C 1s and N 1s spectra, compared with pristine LSCO. This  $\pi$ - $\pi^*$  shake-up peaks shifting in N-GQDs indicate the electron transfer from LSCO to N-GQDs, which altered the electronic structure of Co. The XPS of Co shows redox ability of materials  $\text{Co}^{2+}$  and  $\text{Co}^{3+}$  species compared to pure LSCO and GQD-LSCO. Surface Co sites of LSCO are more active than surface oxygen sites, suggesting that surface Co sites govern the OER activity. So they can finally enhance the water splitting performances.

## 4.5 References

- [1] G. Chen, Y. Zhu, H.M. Chen, Z. Hu, S.F. Hung, N. Ma, J. Dai, H.J. Lin, C.T. Chen, W. Zhou, Z. Shao, An Amorphous Nickel-Iron-Based Electrocatalyst with Unusual Local Structures for Ultrafast Oxygen Evolution Reaction, *Adv Mater* 31(28) (2019) e1900883.
- [2] X. Cheng, B.J. Kim, E. Fabbri, T.J. Schmidt, Co/Fe Oxyhydroxides Supported on Perovskite Oxides as Oxygen Evolution Reaction Catalyst Systems, *ACS Appl Mater Interfaces* 11(38) (2019) 34787-34795.
- [3] M. Chen, S. Lu, X.Z. Fu, J.L. Luo, Core-Shell Structured NiFeSn@NiFe (Oxy)Hydroxide Nanospheres from an Electrochemical Strategy for Electrocatalytic Oxygen Evolution Reaction, *Adv Sci (Weinh)* 7(10) (2020) 1903777.
- [4] S. Niu, W.J. Jiang, Z. Wei, T. Tang, J. Ma, J.S. Hu, L.J. Wan, Se-Doping Activates FeOOH for Cost-Effective and Efficient Electrochemical Water Oxidation, *J Am Chem Soc* 141(17) (2019) 7005-7013.
- [5] Y. Duan, S.N. Sun, Y.M. Sun, S.B. Xi, X. Chi, Q.H. Zhang, X. Ren, J.X. Wang, S.J.H. Ong, Y.H. Du, L. Gu, A. Grimaud, Z.C.J. Xu, Mastering Surface Reconstruction of Metastable Spinel Oxides for Better Water Oxidation, *Adv. Mater.* 31(12) (2019) 8.
- [6] Q.R. Shi, C.Z. Zhu, D. Du, Y.H. Lin, Robust noble metal-based electrocatalysts for oxygen evolution reaction, *Chem. Soc. Rev.* 48(12) (2019) 3181-3192.
- [7] Z. Cai, L. Li, Y. Zhang, Z. Yang, J. Yang, Y. Guo, L. Guo, Amorphous Nanocages of Cu-Ni-Fe Hydr(oxy)oxide Prepared by Photocorrosion For Highly Efficient Oxygen Evolution, *Angew Chem Int Ed Engl* 58(13) (2019) 4189-4194.
- [8] K. Liu, F. Wang, P. He, T.A. Shifa, Z. Wang, Z. Cheng, X. Zhan, J. He, The Role of Active Oxide Species for Electrochemical Water Oxidation on the Surface of 3d-Metal Phosphides, *Advanced Energy Materials* 8(15) (2018).
- [9] J. Huang, Y. Sun, Y. Zhang, G. Zou, C. Yan, S. Cong, T. Lei, X. Dai, J. Guo, R. Lu, Y. Li, J. Xiong, A New Member of Electrocatalysts Based on Nickel Metaphosphate Nanocrystals for Efficient Water Oxidation, *Adv Mater* 30(5) (2018).
- [10] X. Li, H. Wang, Z.M. Cui, Y.T. Li, S. Xin, J.S. Zhou, Y.W. Long, C.Q. Jin, J.B. Goodenough, Exceptional oxygen evolution reactivities on CaCoO<sub>3</sub> and SrCoO<sub>3</sub>, *Sci. Adv.* 5(8) (2019) 7.

- [11] J. Liu, E. Jia, L. Wang, K.A. Stoerzinger, H. Zhou, C.S. Tang, X. Yin, X. He, E. Bousquet, M.E. Bowden, A.T.S. Wee, S.A. Chambers, Y. Du, Tuning the Electronic Structure of LaNiO<sub>3</sub> through Alloying with Strontium to Enhance Oxygen Evolution Activity, *Adv Sci (Weinh)* 6(19) (2019) 1901073.
- [12] W.Y. Nie, H.H. Tsai, R. Asadpour, J.C. Blancon, A.J. Neukirch, G. Gupta, J.J. Crochet, M. Chhowalla, S. Tretiak, M.A. Alam, H.L. Wang, A.D. Mohite, High-efficiency solution-processed perovskite solar cells with millimeter-scale grains, *Science* 347(6221) (2015) 522-525.
- [13] M. Risch, K.A. Stoerzinger, S. Maruyama, W.T. Hong, I. Takeuchi, Y. Shao-Horn, La<sub>0.8</sub>Sr<sub>0.2</sub>MnO<sub>3-δ</sub> Decorated with Ba<sub>0.5</sub>Sr<sub>0.5</sub>Co<sub>0.3</sub>Fe<sub>0.2</sub>O<sub>3-δ</sub>: A Bifunctional Surface for Oxygen Electrocatalysis with Enhanced Stability and Activity, *Journal of the American Chemical Society* 136(14) (2014) 5229-5232.
- [14] H.N. Sun, G. Chen, J. Sunarso, J. Dai, W. Zhou, Z.P. Shao, Molybdenum and Niobium Codoped B-Site-Ordered Double Perovskite Catalyst for Efficient Oxygen Evolution Reaction, *ACS Appl. Mater. Interfaces* 10(20) (2018) 16939-16942.
- [15] G. Liu, H. Chen, L. Xia, S. Wang, L.X. Ding, D. Li, K. Xiao, S. Dai, H. Wang, Hierarchical Mesoporous/Macroporous Perovskite La<sub>0.5</sub>Sr<sub>0.5</sub>CoO<sub>3-x</sub> Nanotubes: A Bifunctional Catalyst with Enhanced Activity and Cycle Stability for Rechargeable Lithium Oxygen Batteries, *ACS Appl Mater Interfaces* 7(40) (2015) 22478-86.
- [16] J.T. Mefford, X. Rong, A.M. Abakumov, W.G. Hardin, S. Dai, A.M. Kolpak, K.P. Johnston, K.J. Stevenson, Water electrolysis on La(1-x)Sr(x)CoO(3-δ) perovskite electrocatalysts, *Nat Commun* 7 (2016) 11053.
- [17] M.H. Seo, H.W. Park, D.U. Lee, M.G. Park, Z. Chen, Design of Highly Active Perovskite Oxides for Oxygen Evolution Reaction by Combining Experimental and ab Initio Studies, *ACS Catalysis* 5(7) (2015) 4337-4344.
- [18] P.Y. Zhang, T. Song, T.T. Wang, H.P. Zeng, In-situ synthesis of Cu nanoparticles hybridized with carbon quantum dots as a broad spectrum photocatalyst for improvement of photocatalytic H<sub>2</sub> evolution, *Appl. Catal. B-Environ.* 206 (2017) 328-335.
- [19] D. Tang, J. Liu, X.Y. Wu, R.H. Liu, X. Han, Y.Z. Han, H. Huang, Y. Liu, Z.H. Kang, Carbon Quantum Dot/NiFe Layered Double-Hydroxide Composite as a Highly Efficient Electrocatalyst for Water Oxidation, *ACS Appl. Mater. Interfaces* 6(10) (2014) 7918-7925.

- [20] G. Li, S. Hou, L. Gui, F. Feng, D. Zhang, B. He, L. Zhao, Carbon quantum dots decorated Ba<sub>0.5</sub>Sr<sub>0.5</sub>Co<sub>0.8</sub>Fe<sub>0.2</sub>O<sub>3</sub>- perovskite nanofibers for boosting oxygen evolution reaction, *Applied Catalysis B: Environmental* 257 (2019).
- [21] S. Kundu, B. Malik, D.K. Pattanayak, P. Ragupathy, V.K. Pillai, Role of Specific N-Containing Active Sites in Interconnected Graphene Quantum Dots for the Enhanced Electrocatalytic Activity towards Oxygen Evolution Reaction, *ChemistrySelect* 2(31) (2017) 9943-9946.
- [22] Y. Han, Z. Zhu, L. Huang, Y. Guo, Y. Zhai, S. Dong, Hydrothermal synthesis of polydopamine-functionalized cobalt-doped lanthanum nickelate perovskite nanorods for efficient water oxidation in alkaline solution, *Nanoscale* 11(41) (2019) 19579-19585.
- [23] J. Suntivich, K.J. May, H.A. Gasteiger, J.B. Goodenough, Y. Shao-Horn, A Perovskite Oxide Optimized for Oxygen Evolution Catalysis from Molecular Orbital Principles, *Science* 334(6061) (2011) 1383-1385.
- [24] Y. Zhu, W. Zhou, Z.G. Chen, Y. Chen, C. Su, M.O. Tade, Z. Shao, SrNb<sub>(0.1)</sub>Co<sub>(0.7)</sub>Fe<sub>(0.2)</sub>O<sub>(3- $\delta$ )</sub> perovskite as a next-generation electrocatalyst for oxygen evolution in alkaline solution, *Angew Chem Int Ed Engl* 54(13) (2015) 3897-901.
- [25] I.C. Man, H.Y. Su, F. Calle-Vallejo, H.A. Hansen, J.I. Martinez, N.G. Inoglu, J. Kitchin, T.F. Jaramillo, J.K. Nørskov, J. Rossmeisl, Universality in oxygen evolution electrocatalysis on oxide surfaces, *ChemCatChem* 3 (2011) 1159–1165
- [26] Nguyen, S. T. et al. Enhancement effect of Ag for Pd/C towards the ethanol electro-oxidation in alkaline media. *Appl. Catal. B Environ.* 91, 507–515 (2009).
- [27] Yang et al. Identification of catalytic sites for oxygen reduction and oxygen evolution in N-doped graphene materials: Development of highly efficient metal-free bifunctional electrocatalyst. *Sci. Adv.* 2, e1501122 (2016)
- [28] Y. Zhu, L. Zhang, B. Zhao, H. Chen, X. Liu, R. Zhao, X. Wang, J. Liu, Y. Chen, M. Liu, Improving the Activity for Oxygen Evolution Reaction by Tailoring Oxygen Defects in Double Perovskite Oxides, *Advanced Functional Materials* 29(34) (2019)



## CHAPTER 5. ELECTROCATALYTICALLY DRIVEN FAST REMOVAL OF MOISTURE BY CONDENSATION OF VAPOR AND WATER SPLITTING

### 5.1 Introduction

Water splitting technology, which produces hydrogen ( $H_2$ ) and oxygen ( $O_2$ ) gases from water, is a long-term technology pathway with potentially low or no greenhouse gas emissions. Most research of water-splitting through an electrocatalytic process has focused on the efficient ways of the  $H_2$  and  $O_2$  production [1-2]. The precious metals (Pt) and noble metal oxides ( $RuO_2$  and  $IrO_2$ ) were known to be the most efficient catalysts for HER and OER, respectively [3-4]. However, because of the high cost and scarcity of the materials, numerous efforts have been made to develop cost-effective and highly-active electrocatalysts to replace them. Transition-metal-based compounds, such as oxides, carbides, nitrides, sulfides, and selenides, have been studied as alternative electrocatalysts for these reactions [5-12]. Metal-free electrocatalysts, such as graphene and carbon nanotubes, were also known to have high electrocatalytic activities [13-14]. Recently, transition metal phosphides such as  $Ni_2P$  [15-16],  $Ni_5P_4$  [17],  $Ni_{12}P_5$  [18],  $Cu_3P$  [19-20], and  $CoP$  [21] were reported to be quite effective as HER catalysts because of the low Gibbs free energy for  $H_2$  adsorption and the small  $H_2O$  adsorption energy [22-23]. Furthermore, the phosphides featured good electrical conductivity and high stability over a wide pH range, promising candidates for bifunctional electrocatalysts. It indicates that these catalysts are quite useful in neutral media, as well as in acidic ( $H_2SO_4$ ) and basic (KOH) media.

In addition to producing gas, water splitting can be used to remove the water absorbed on a surface from the air by condensation of vapor in high humidity, thus, controlling the water content of the air (i.e. the humidity). The water can be also driven onto any surface by a large difference between inside and outside temperatures. This phenomena commonly occurs in everyday life, such as on windows in winter and car headlight lenses. This water can cause damage to buildings, discolor headlights, and fog up windows in cars (Figure 30(a)). Water absorbing materials such as sodium polyacrylate [24], zeolite [25], mesoporous silica [26], silica gel [27], and the activated carbon [28] were already used as shown in Figure 30(b), but they cannot be reusable and water can be reformed. Heat exchanger or air conditioner can be also effective, but the systems are complicated and expensive [29-30]. Here, an

electrocatalytically driven moisture control technology is demonstrated by condensation of vapor and water splitting. For this, it is essential to develop highly active electrocatalysts with long-term stability at high potentials because the pH of the condensed water can be very close to 7.0, meaning that the number of ions in the water is very small. Among the electrocatalysts which have been studied so far, nickel-phosphide (Ni-P) was known to have the low adsorption energy of hydrogen ( $H^+$ ) on surfaces and partial positive charges on P atoms, exhibiting the high activity toward the HER [31-32]. It also can be functioned as a OER catalyst, due to formation of oxidation sheel during water oxidation [32] as seen in Figure 31. It was also reported to be stable because of its relatively high corrosion resistance due to amorphous nature and passivity, immune to attack at grain boundary [33-35]. Various mechanisms and experimental evidences have been demonstrated, in which the partial covalent bond formation between Ni and P atoms led to a partial negative charge on the P atoms [31], and thus the dissolution of Ni into the water was prohibited [34-35]. Also, P atoms may be also oxidized into phosphate, which can subsequently act as a diffusion barrier for active dissolution [35].

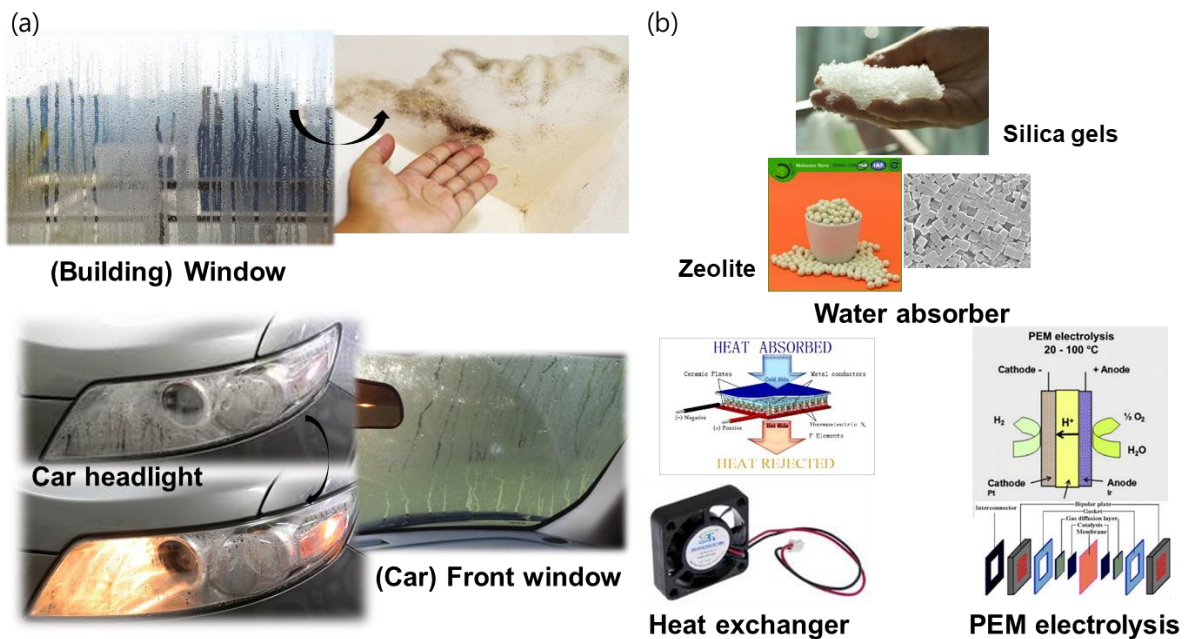


**Figure 30.** (a) Moisture formation in daily lives, and (b) conventional several methods for removing moisture such as water absorber, heat exchanger, PEM electrolysis.

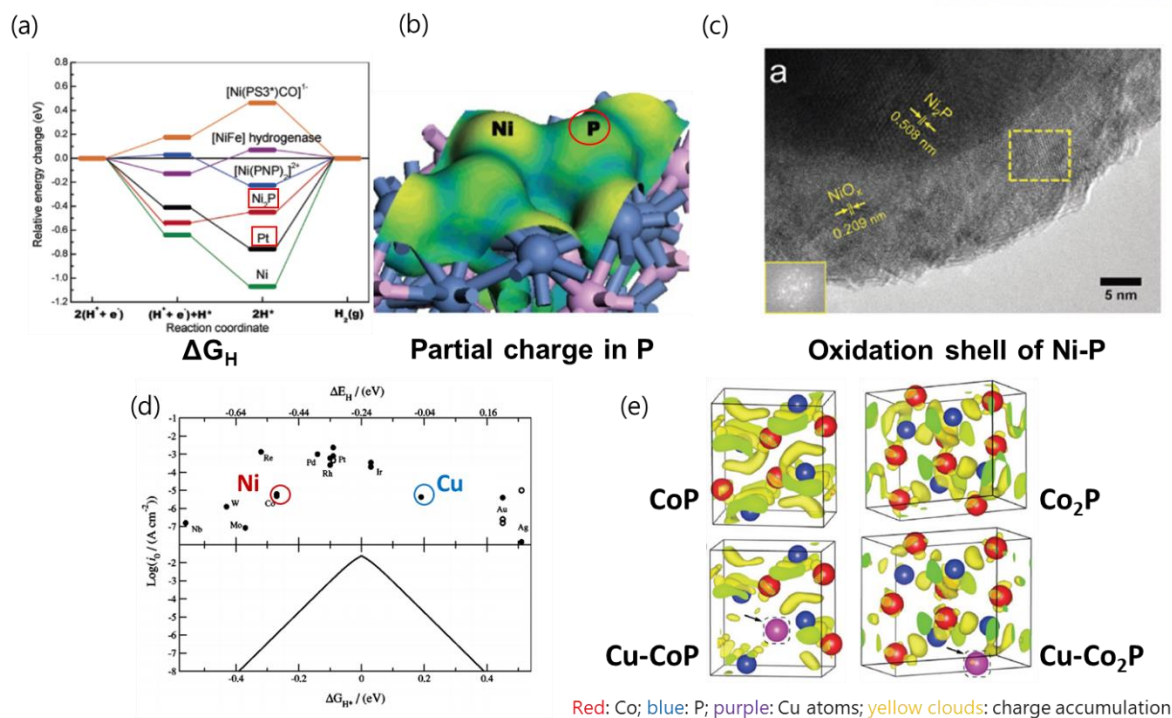


**Figure 31.** (a) Gibbs free energy of adsorption of hydrogen in Ni-P compared with Pt [31], (b) Calculated electron density of the Ni<sub>2</sub>P surface [31], (c) TEM images of Ni-P with oxidation shell of NiO<sub>x</sub> after OER [32], (d) Volcano plot for metals including Ni and Cu [37], (e) Bonding charge distribution of Cu-doped Cobalt phosphide [36].

Here, we report a facile strategy to fabricate the two-electrode electrochemical cell for the electrocatalytically driven moisture control technology, based on the nickel-copper-phosphide (NiCu-P) film synthesized by simple electrodeposition on Ni substrate. The Cu incorporation into the Ni-P film is expected to enhance the electrocatalytic activity due to the decrease of charge transfer resistance of the surface and opposite sign of binding energy with hydrogen on Cu compared with that of Ni in Figure 31 [36-37]. The film can be also used as bifunctional catalysts for HER and OER electrodes. The NiCu-P films were amorphous Ni-rich materials with various nanocrystalline phases such as Ni<sub>12</sub>P<sub>5</sub> and Ni<sub>3</sub>P at low Cu content (< 9 at.%). The overpotentials in a three-electrode configuration were measured to be 48 mV at -10 mA/cm<sup>2</sup> for HER in acidic solution and 330 mV and at 20 mA/cm<sup>2</sup> for OER in alkaline solution, respectively, while pure Ni-P films showed -60 mV and 380 mV, respectively. In order to achieve long-term stability at high voltages, the surface of the films used as OER electrodes were treated with oxygen plasma, producing an oxygen-rich layer in a near-surface region and preventing the formation of some desiccation cracks. For the HER

electrodes, the film was used without any modifications. When the two-electrode electrochemical cell was dipped into pure water, it successfully removed the water at a rate of 0.6 ml/hr at 10 V. Based on the results, a planar-type cell composed of two interdigitated electrodes are fabricated and attached to the inner surface of the transparent headlamp of a car. The water condensed onto the surface from the air at a relative humidity of > 99 % was effectively removed and the inside of the headlamp became quite clean within several minutes, indicating that the content of the water in the air could be reduced. Finally, a flexible cell with transparency over 90 % was fabricated and the water removal capability was found to maintain over 75 % at a curvature of 0.18/cm.

## 5.2 Experimental details

### 5.2.1 Electrodeposition of Ni-P and NiCu-P films

Nickel sulfate hexahydrate ( $\text{NiSO}_4 \cdot 6\text{H}_2\text{O}$ ), copper sulfate pentahydrate ( $\text{CuSO}_4 \cdot 5\text{H}_2\text{O}$ ), sodium hypophosphite monohydrate ( $\text{NaH}_2\text{PO}_2 \cdot \text{H}_2\text{O}$ ), sodium acetate ( $\text{CH}_3\text{COONa}$ ), and glycine ( $\text{NH}_2\text{CH}_2\text{COOH}$ ) were purchased from Sigma-Aldrich and used as received without any modifications. NiCu-P films were deposited on Ni foam or  $\text{SiO}_2/\text{Si}$  substrate with Ti/Ni (20/100 nm) metallic layer at room temperature. 0.1M of  $\text{NiSO}_4 \cdot 6\text{H}_2\text{O}$  and 0.1M of  $\text{CuSO}_4 \cdot 5\text{H}_2\text{O}$  were mixed in DI water and 200 mL solution was prepared with the ratio of the solutions. 1 M of  $\text{NaH}_2\text{PO}_2$ , 0.1 M of  $\text{CH}_3\text{COONa}$ , and 0.1 M of glycine were dissolved in DI water of 150 mL. Prior to the electrodeposition, the substrate was washed with acetone, isopropanol (IPA), and DI water several times under sonication. The electrodeposition was carried out in a home-made three-electrode setup, using a graphite rod as the counter electrode and a Ag/AgCl electrode as the reference electrode. Nitrogen was bubbled through the deposition solution for at least 15 min prior to the deposition and maintained during the whole deposition process. The deposition cycle was controlled 3 to 15 times between - 1.2 V and + 0.2 V with a scan rate of 10 mV/s at 600 rpm. After electrodeposition, the NiCu-P samples were carefully taken from the electrolyte solution, rinsed with ethanol and DI water, and dried in a vacuum at room temperature.

### 5.2.2 Material characterization

Scanning electron microscopy images and elemental analysis of the samples were characterized by SEM (Nova NanoSEM, SU8220 Cold FE-SEM) equipped with an energy dispersive X-ray analyzer. High resolution images were collected by HR-TEM (JEOL JEM-2100F) with the equipped energy dispersive spectrometer. The crystallinity and phase information of the samples were given by a Bruker AXS/D8 ADVANCE diffractometer with Cu K $\alpha$  radiation ( $\lambda = 1.5418 \text{ \AA}$ ). I-V curves were obtained using a Keithley 2636A source measurement unit while applying bias swept from -0.25 V to 0.25 V. The transmittance of the films was measured using a UV-Vis-NIR spectrometer (Agilent/Cary 5000).

### 5.2.3 Electrochemical measurement in a three-electrode configuration

Electrochemical measurements were performed by IVIUM Stat (US). Ni-P and NiCu-P samples, a Pt wire, and an Ag/AgCl electrode were used as a working, counter, and reference electrode, respectively. HER and OER measurements were conducted in 0.5 M H<sub>2</sub>SO<sub>4</sub> and 1.0 M KOH solutions, respectively. All potentials related to this work were converted to the RHE ( $E_{\text{RHE}} = E_{\text{Ag/AgCl}} + 0.1976 + 0.0592 \text{ pH}$ ). The linear sweep voltammetry curves were obtained in 0.5 M H<sub>2</sub>SO<sub>4</sub>, 1.0 M KOH, and pure water (0.4 M $\Omega \cdot \text{cm}$ ) at a scan rate of 10 mV/s and a rotating speed of 1000 rpm with iR (current times internal resistance) correction. Electrochemical Impedance Spectroscopy (EIS) was performed in the same configuration at the frequency from 10<sup>5</sup> to 0.1 Hz with an AC voltage amplitude of 10 mV. The current measurements were carried out in a two-electrode setup in pure water by using NiCu-P film as bifunctional catalysts. The anode was modified with O<sub>2</sub> plasma when needed.

### 5.2.4 Fabrication of two-electrode electrochemical cells

The SiO<sub>2</sub>/Si substrates were cut into pieces of 2.5 cm  $\times$  2.5 cm in area, then cleaned using acetone/IPA/DI water under sonication. The two-electrode electrochemical cell is composed of a pair of comb-type finger electrodes, that is, interdigitated electrodes, fabricated by a step-by-step process. By using an image reversal process (soft baking at 80°C and reversal baking at 100°C) with AZ5214 and a photomask consisting of comb structures, a comb structured pattern was formed and Ti /Ni (20/100 nm) was deposited, followed by the electrodeposition of the NiCu-P film onto the metallic layer to fabricate the OER electrode.



The thickness of the film was measured to be about 600 nm. The film was treated with the O<sub>2</sub> plasma treatment for 30 min, carried out under a pressure of 20 Pa and a radio-frequency (rf) power of 100 W in reactive ion etcher (TTL/Labstar). The other comb structured electrode was also fabricated by depositing Ti /Ni (20/100 nm) layer on the substrate by same procedure, followed by the electrodeposition of the NiCu-P film onto the layer. It was used as a HER electrode without any modifications. For flexible cells, the PEN substrates were used. All processes are same as that done in SiO<sub>2</sub>/Si substrates, but the thickness of Ni and NiCu-P film were controlled to be about 50 nm and 300 nm, respectively. High transparency was obtained by introducing holes of a 80 μm in diameter and 100 μm in a hole-to-hole distance. Teflon-wrapped silver coated copper wire was connected to both pads by using Ag paste, followed by sealing by Kapton tape.

### **5.2.5 Measurement of two-electrode electrochemical cells**

Humidity in headlamp was controlled using humidifier connected with silicone rubber hose. Fogs on the front surface of headlamp were formed after covering it by a cold wet wiper. Thermo/Humidity meter was used to quantify the amount of water vapor in the headlamp for precise control of humidity. To minimize leakage of vapor, water-proof glue gun was used to block any hole of the headlamp after inserting the device into the headlamp. The current measurements were carried out on the device in the headlamp. Bending tester (Z-tec/ZB-100) was used to fix a flexible device in a bent shape for the measurement.

## **5.3 Results and Discussion**

### **5.3.1 Electrodeposition of Ni-P and NiCu-P films**

A typical fabrication procedure of NiCu-P films is presented in Figure 32a and the detailed information is described in Methods. In Ni-P solution without Cu content, it showed bright green and there was no significant change in color when 0.5 mmol CuSO<sub>4</sub> was added to the solution, as shown in Figure 33. However, as the concentration of CuSO<sub>4</sub> increased to 4 mmol, it was changed to bluish green and the intensity of the blue became strong with the increasing the concentration of CuSO<sub>4</sub>. The solution with only CuSO<sub>4</sub> showed blue color. The films were then deposited onto the flat SiO<sub>2</sub>/Si substrate with the Ti/Ni (20/100 nm) layer using the electrodeposition process. In general, at the initial stage of deposition, it starts by a primary

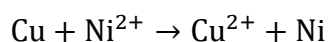
nucleation of metal by Volmer-Weber modes, which induces a phosphorus co-deposition due to the strong interaction with the metal. This leads to instantaneous nucleation and growth of hemispherical clusters [38] and then a columnar-structured film with the smooth surface is grown. At the low Cu concentration, the Cu ions were reported to suppress the hydrogen evolution during electrodeposition to prevent a void in films, acting as a stabilizer and having no effect on the deposition, as shown in Figures 32b, 32c, and 34 [39]. As the Cu content increased, many droplets (i.e. nodules) on the surface were produced and their size was drastically increased to approximately 1  $\mu\text{m}$  when 10 mmol  $\text{CuSO}_4$  was added to the solution, as shown in Figures 32c and 34. In general, the nodular structure significantly depends on the nucleation rate and the surface diffusion of the metallic ions participating in the growth. According to the larger reduction potential ( $\sim 0.337$  V) of the Cu ions than that ( $\sim -0.25$  V) of Ni ions, at the initial stage of deposition, the Cu seems to be deposited before the Ni at Cu concentration higher than a critical value. The nodule formation then appears as the result of the concentrated Cu ion reactions over a localized area, consequently creating the nucleus. The increase of the size of the droplets with increasing the Cu concentration may also mean faster surface diffusion of the Cu ions, compared with that of the Ni ions [40]. The photos and cross-sectional view of the scanning electron microscope (SEM) images in Figure 32c showed uniform film coverage over large areas and good adhesion property on the electrode.

Figure 32d shows X-ray diffraction (XRD) results for the films as a function of the atomic ratio of Cu to Ni, measured by using energy dispersive X-ray (EDX). As reference, the XRD pattern of the Ni was also obtained. The two representative peaks at  $44.66^\circ$  and  $51.98^\circ$  were observed in the Ni, corresponding to the (200) and (111) planes of the metallic Ni. For the pristine Ni-P film, there were no more peaks except the two peaks stated above. However, the expanded view of the peak positioned at  $44.66^\circ$  showed that it became quite broad and several peaks on the left side of the main peak were observed. According to the phase diagram of Ni and P [41], the solubility of the phosphorus in Ni is very small ( $\sim 0.32\%$ ) at room temperature, meaning that the amount of the P is very small in the film. However, the film contained 20 atomic % of the phosphorous by using EDX spectra shown in Figure 35a. According to the atomic size ( $\sim 98$  pm) of the phosphorous, compared with that of the Ni ( $\sim 147$  pm), it seems that the phosphorous occupied the interstitial sites [42]. According to the formation energy of Ni-P and Cu-P compounds shown in Figure 35b [42], it also seems that various Ni-P phases were produced. In high-resolution transmission electron microscope (HR-TEM) images shown in Figure 32e, the nanocrystalline materials such as  $\text{Ni}_{12}\text{P}_5$  and  $\text{Ni}_3\text{P}$  were



also observed, which corresponded to the peaks on the left of the main peak. Thus, it is believed that the Ni-P film was a form of Ni-rich phases, having several Ni-P secondary phases.

As the Cu ions were incorporated, the peak at 44.66 ° became broader. Actually, with 9 at. % Cu, the full-width-half-maximum (FWHM) was increased from 0.32 ° to 0.38 °, compared with pristine Ni phosphide film. This implies that Cu ions were incorporated into the Ni phosphide. However, the further increase in the Cu concentration produced a secondary peak positioned at 43.63 °. To identify the origin of this peak, Cu phosphide film was deposited onto the Ni and the XRD pattern was obtained. The peak was indexed to Cu (200) and it is believed that the small amount of the phosphorous was incorporated into Cu, forming Cu-rich phosphide film, according to the phase diagram [43]. Actually, the atomic size of the Cu is almost the same as that of the Ni and the two elements show a perfect solid solution in the entire composition. Thus, the Cu was expected to perfectly occupy the Ni sites during the electrodeposition. However, beyond a certain critical Cu concentration, a new phase, which was Cu-rich, was produced. This may be explained via the extremely small equilibrium constant ( $K \sim 6.6 \times 10^{-21}$ ) of the overall redox reaction of nickel and copper ions expressed as [39],



As  $K$  is much smaller than unity at high Cu ions concentration, the preferred deposition of Cu-P can be expected, as mentioned above. In the TEM image of Figure 32e, the segregation of the Cu-rich phase was also observed.

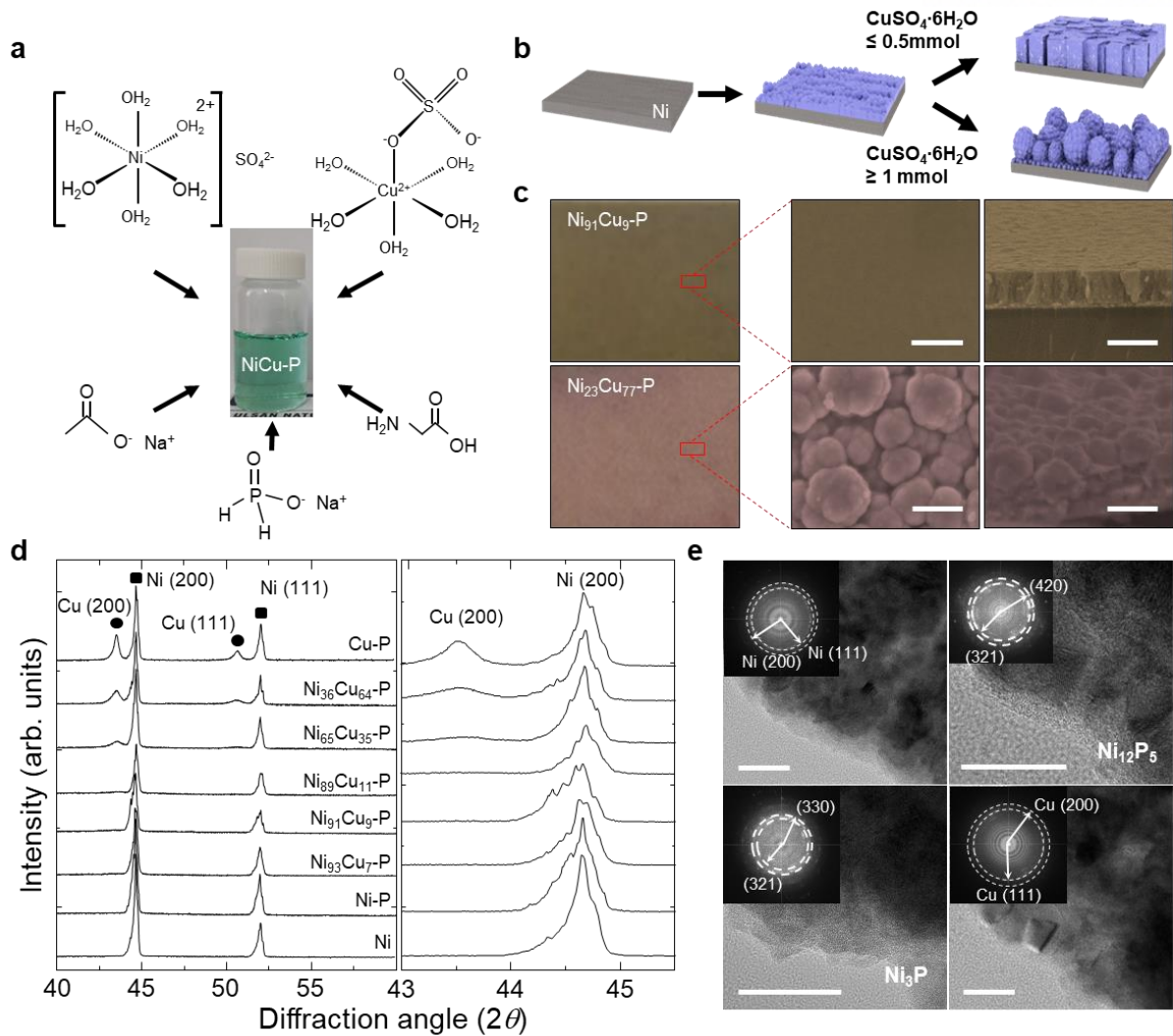
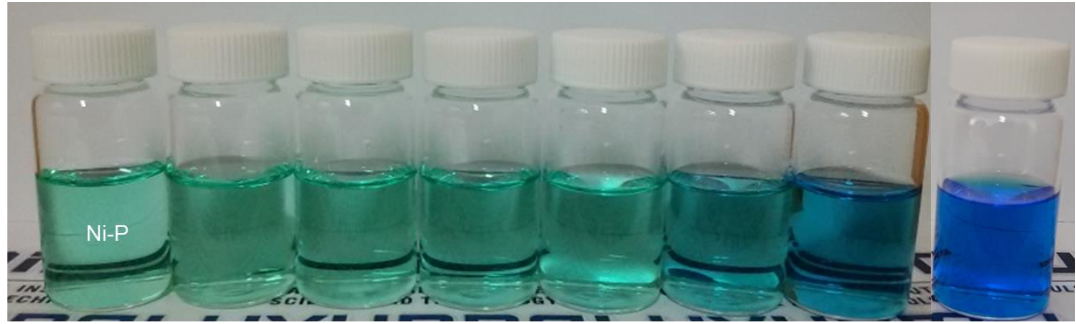


**Figure 32.** (a) Precursors used and photo of  $\text{NiCu-P}$  solution. (b) Schematic illustration of  $\text{NiCu-P}$  film with  $\text{CuSO}_4 \cdot 6\text{H}_2\text{O}$  concentration. (c) Photos and SEM images of  $\text{NiCu-P}$  film on  $\text{SiO}_2/\text{Si}$  substrate with  $\text{Ti/Ni}$  (20/100 nm) with  $\text{CuSO}_4 \cdot 6\text{H}_2\text{O}$  concentration. scale bar: 1  $\mu\text{m}$ . (d) XRD data of electrodeposited  $\text{NiCu-P}$  film on  $\text{Ni}$  substrate with  $\text{Cu}$  content. (e) High-resolution TEM images of  $\text{NiCu-P}$  film and the corresponding fast Fourier Transform (FFT) patterns of the selected area. scale bar: 20 nm.



$\text{NiSO}_4 \cdot 6\text{H}_2\text{O}$	100	99.75	99.5	99	98	96	90	0
$\text{CuSO}_4 \cdot 6\text{H}_2\text{O}$	0	0.25	0.5	1	2	4	10	100

(mmol)

**Figure 33.** The photos of NiCu-P solutions with different  $\text{CuSO}_4 \cdot 6\text{H}_2\text{O}$  concentration.

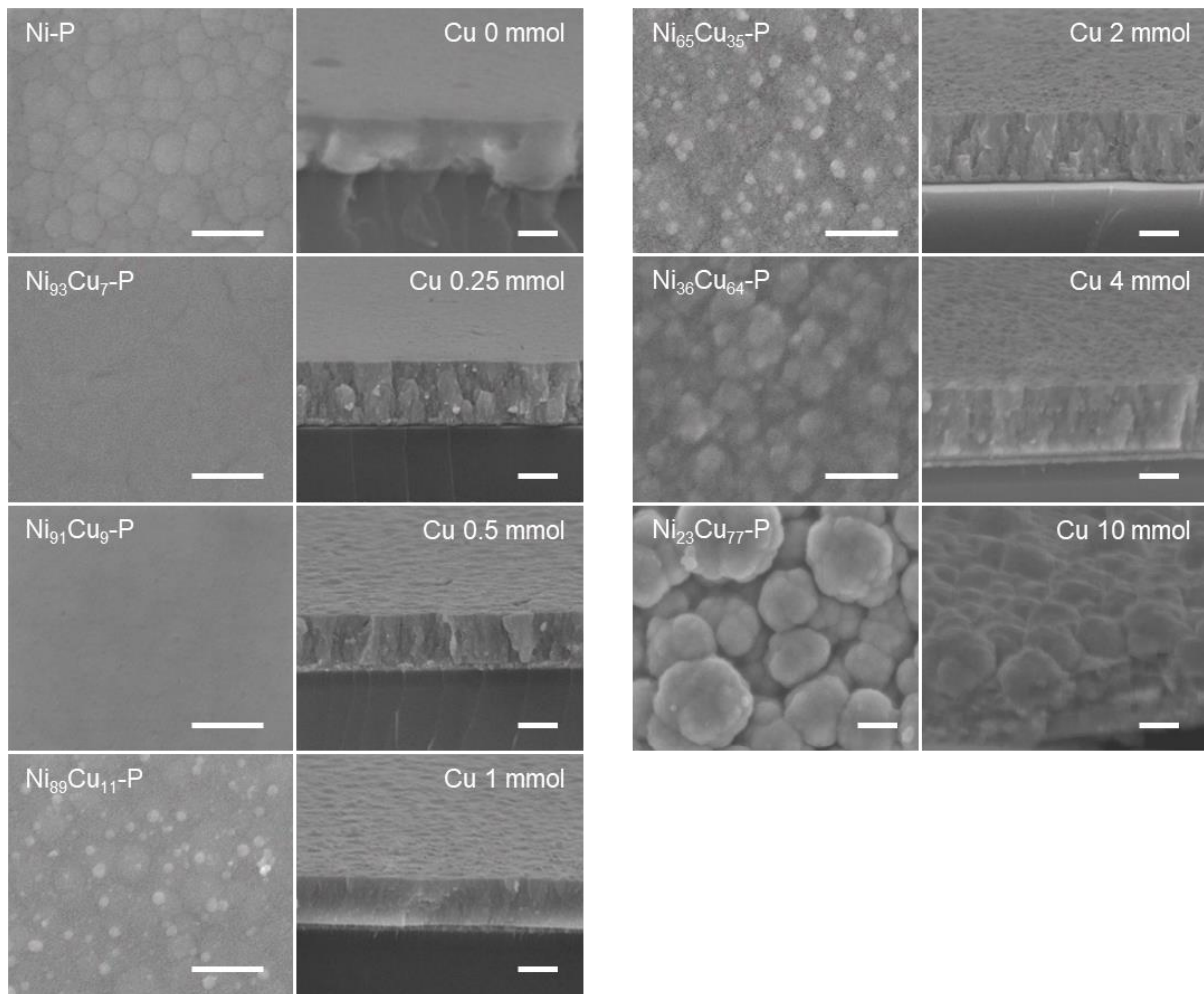


**Figure 34.** The SEM images of the NiCu-P with different ratios of Ni:Cu (scale bar: 0.5  $\mu\text{m}$ ).

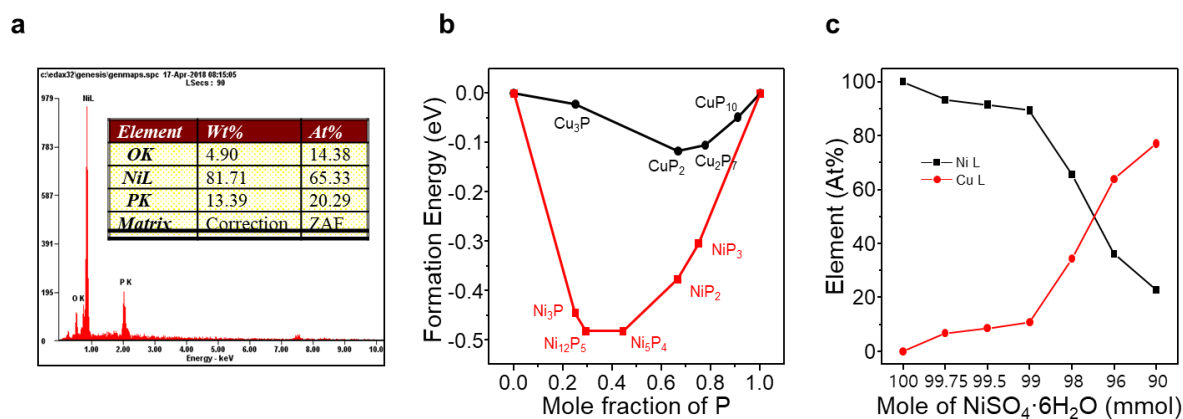


**Figure 35.** (a) EDX elemental analysis of Ni-P. (b) Formation energy of Ni-P with the different mole fraction of P. (c) Elemental composition (Ni, Cu) of NiCu-P with the different mole of NiSO<sub>4</sub>·6H<sub>2</sub>O of precursors.

### 5.3.2 Electrocatalytic HER and OER performances in Acidic and Basic Media

The electrocatalytic HER and OER activities of the NiCu-P films supported on the Ni foam were evaluated in a three-electrode configuration with the Ag/AgCl as a reference electrode under acidic (0.5 M H<sub>2</sub>SO<sub>4</sub>, pH 0.3) and alkaline (1.0 M KOH, pH 14) conditions, respectively. To evaluate the electrocatalytic activity toward HER, a Pt wire as a counter electrode was used and the current density versus potential at a scan rate of 10 mV/s was measured recorded at room temperature as a function of at. % of the Cu from 0 % to 64 %, plotted in Figure 36a. For the pristine Ni-P film, a current density of -10 mA/cm<sup>2</sup> was achieved at an overpotential ( $\eta$ ) of 60 mV vs reversible hydrogen electrode (RHE). As the Cu ions were incorporated, the overpotential decreased to 48 mV at Cu 9 at.%. Although the commercial Pt/C exhibits the lowest overpotential [44-45], the measured overpotential value is lower than that of some other phosphides-based HER catalysts such as Ni<sub>2</sub>P [16], Ni<sub>5</sub>P<sub>4</sub> [17], CoP [46], Fe<sub>3</sub>P [47], and CoFeP [48]. The SEM images of the film at Cu 9 at.% also showed that it was very uniformly coated on the Ni foam with few cracks, indicating that the adhesive properties were excellent. Further increase in the at. % of the Cu significantly increased the overpotential to -127 mV. The corresponding Tafel plots to study the HER kinetics of the samples were obtained, plotted in Figure 36b. Notably, when at.% of the Cu was approximately 9 %, the film had the smallest Tafel slope of only 69 mV/dec and a further increase in the composition increased the slope to 101 mV/dec at 64 at. %, indicating the highest conversion efficiency

with 9 at.% of the Cu. The Nyquist plots recorded at an overpotential of 320 mV also showed that the NiCu-P film gave rise to charge transfer resistance that is much lower than the pristine Ni-P film, as shown in Figure 36c.

The OER performance on the NiCu-P films was also investigated in the same manner, as shown in Figure 36d-f. The current densities with the at.% of the Cu showed very similar trends to the HER performances. Specifically, the overpotential required for achieving a current density of 20 mA/cm<sup>2</sup> was only 330 mV, which was significantly lower than those of pristine Ni-P film and NiCu-P films with different composition of the Cu. As shown in the inset, all samples showed distinct anodic peaks between 1.3 and 1.5 V versus RHE, which was associated with the oxidation of Ni and/or Cu species, such as the transition from  $\alpha$ -Ni(OH)<sub>2</sub> to  $\gamma$ -NiOOH and  $\beta$ -Ni(OH)<sub>2</sub> to  $\beta$ -NiOOH, respectively [49,50]. In general, Ni(OH)<sub>2</sub> can easily be oxidized to NiOOH, which is needed for the high activity in the water oxidation reaction. However,  $\gamma$ -NiOOH was known to be formed by the insertion of Na ions to the Ni-P film during the water splitting process, causing swelling of the film, thus, the electrode volume expansion with subsequent microcracks and disintegration of the film [51,52]. The peak intensity was smallest in the Ni-P film with Cu 9 at.%, indicating that the addition of the Cu with careful control in the at.% might be a very effective strategy to suppress the formation of  $\gamma$ -NiOOH phase. This would also promote the formation of  $\alpha$ -Ni(OH)<sub>2</sub> or  $\beta$ -Ni(OH)<sub>2</sub> occurred on the surface, providing more active sites of OER [53]. Tafel plots for OER also showed the smallest Tafel slope of 135 mV/dec at the same Cu concentration, thus, the OER performance was enhanced by Cu incorporation in alkaline solution.

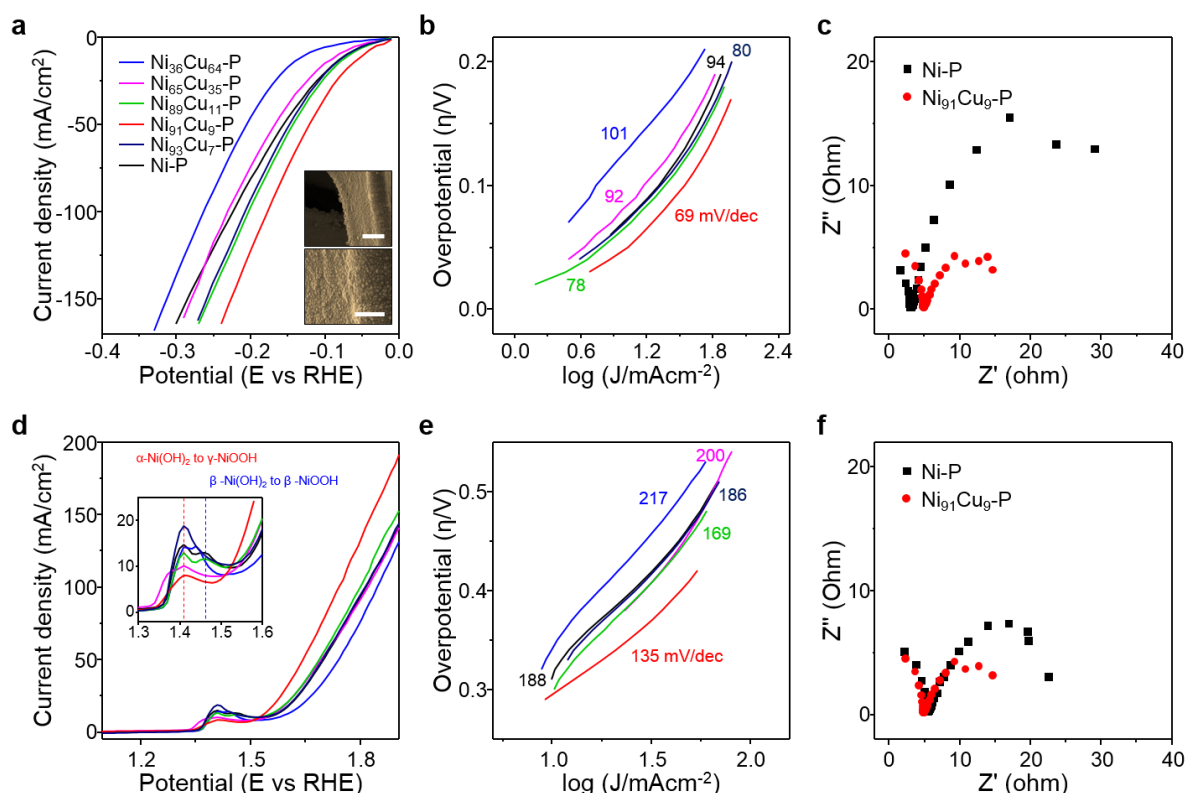


**Figure 36.** (a) Linear sweep voltammetry (LSV) polarization curves of NiCu-P films with different ratios of Ni:Cu in 0.5 M H<sub>2</sub>SO<sub>4</sub> at scan rate of 10 mV/s. The inset shows the SEM images of NiCu-P film with 9 at. % on Ni foam. Scale bar: 25, 10 μm. (b) Corresponding Tafel plots. (c) Nyquist plots recorded obtained at -0.3V versus RHE. (d) LSV polarization curves of NiCu-P films with different ratios of Ni:Cu in 1.0 M KOH. The current densities in ranging from 1.3 V to 1.6 V were also plotted in the inset. (e) Corresponding Tafel plot. (f) Nyquist plots recorded obtained at 1.55V versus RHE.

### 5.3.3 Two-electrode electrochemical devices in DI water

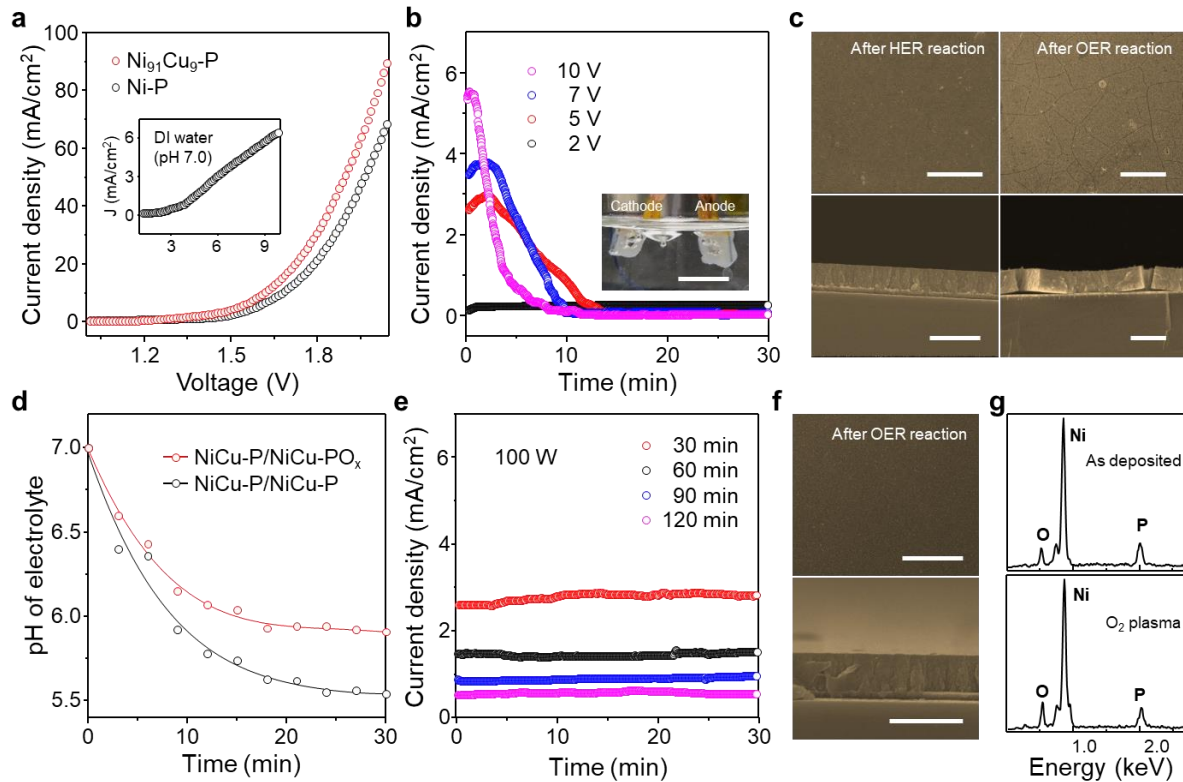
Although the three-electrode electrochemical cell is considered to be a powerful cell configuration for the water-splitting, two-electrode electrochemical cell configuration was used to explore the electrochemically driven splitting of the water molecules on the surface. The NiCu-P films, deposited on the Ni-coated SiO<sub>2</sub>/Si layer, were used as bi-functional electrodes for both HER and OER, as shown in Figure 37a. When the electrodes were dipped into the 1 M KOH electrolyte and the electrochemical measurement was carried out, the current density



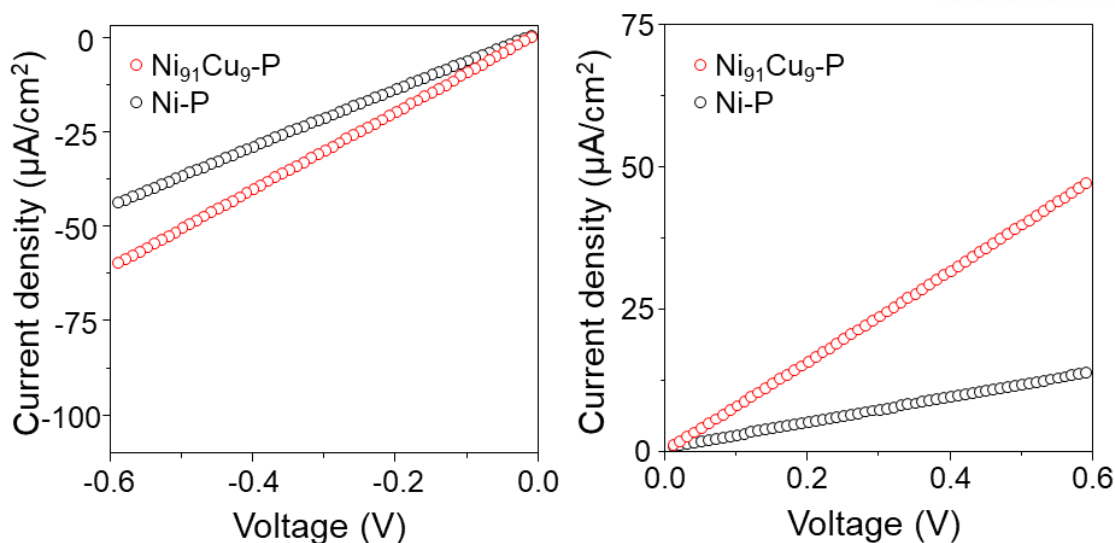
of several tens of mA/cm<sup>2</sup> at applied voltage less than 2 V was obtained, however, the current density significantly decreased to several tens of μA/cm<sup>2</sup> in the pure water, as shown in the inset of the Figure 37a. This means that the concentration of hydroxide or hydrogen ions in pure water is low. The current densities for both HER and OER in three-electrode electrochemical cells of Figure 38 also significantly decreased to several tens of μA/cm<sup>2</sup>. Actually, depending on the surrounding environmental conditions, water can be acidic or almost pure, especially, in the air. Thus, to speed up the water splitting rate in real environments, it seems that high voltage is required as well as the enhanced catalytic properties of films. As expected, the current density of NiCu-P films with Cu 9 at.% is larger than that of the Ni-P films because of the enhanced electrical properties of the NiCu-P films, as shown in Figure 38. Previously, a density functional theory analysis also showed that extra electrons could be released with Cu doping in transition metal phosphides, explaining the increase in conductivity [36].

Figure 37b shows the current density of the two-electrode cell made of NiCu-P films with Cu 9 at.% as a function of the applied voltage in pure water. A current density of 0.26 mA/cm<sup>2</sup> was measured at 2 V and the water was seen to be split to the gases in the inset. As the voltage increased to 10 V, the current density increased to 5.54 mA/cm<sup>2</sup>. However, the current suddenly dropped to zero and the rate of the current decreasing increased with the voltage. Then, there were no gas bubbles at the surface of the electrodes, meaning the water splitting reaction had stopped. The SEM images in Figure 37c show that some desiccation cracks were observed in only OER electrode, while there were no such cracks in the HER electrodes. No current indicates that the films were peeled off during the water splitting reaction at high voltage. The cracks found in the OER electrode may be ascribed to the dissolution of the phosphor atoms incorporated inside the films into the electrolyte and it is accelerated by increasing the voltage in the presence of O<sub>2</sub> in the electrolyte [54,55]. This would cause the chemical deterioration of the film coating on the substrate. This may be confirmed by measuring the pH of the pure water during the water splitting. The pH decreased from 7.0 to 5.5 with the reaction for 30 min, meaning that the water may be an acidic solution by forming phosphoric acid by reacting with phosphorous dissolved into water, as shown in Figure 37d.





**Figure 37.** (a) LSV polarization curves of Ni-P and Ni<sub>91</sub>Cu<sub>9</sub>-P films on Ni recorded in 1.0 M KOH. The inset shows the current density measured in pure water. (b) Current densities measured at various voltages from 2 to 10 V in pure water. The inset shows the gas bubbles on both surfaces when 10 V is applied. Scale bar: 1 mm. (c) Top (scale bar: 1, 10  $\mu$ m) and cross-sectional. scale bar: 1  $\mu$ m. SEM images of the Ni<sub>91</sub>Cu<sub>9</sub>-P films after the HER and OER reaction at 10 V in pure water. (d) pH values of electrolytes measured as a function of the water splitting reaction time at 10 V before and after Ni<sub>91</sub>Cu<sub>9</sub>-P films were treated with O<sub>2</sub> plasma treatment. O<sub>2</sub> plasma-treated NiCu-P film was named as NiCu-PO<sub>x</sub>. (e) Current densities measured at 10 V with O<sub>2</sub> plasma treatment in pure water. (f) Top and cross-sectional SEM images of the Ni<sub>91</sub>Cu<sub>9</sub>-P films after the OER reaction at 10 V in pure water. scale bar: 10, 1  $\mu$ m. (g) EDAX spectra of as-deposited NiCu-P and O<sub>2</sub> plasma-treated NiCu-P films.



**Figure 38.** (a) LSV polarization curves for the HER of Ni-P and Ni<sub>91</sub>Cu<sub>9</sub>-P films on Ni recorded in pure water. (b) LSV polarization curves for the OER of Ni-P and Ni<sub>91</sub>Cu<sub>9</sub>-P films on Ni recorded in pure water.

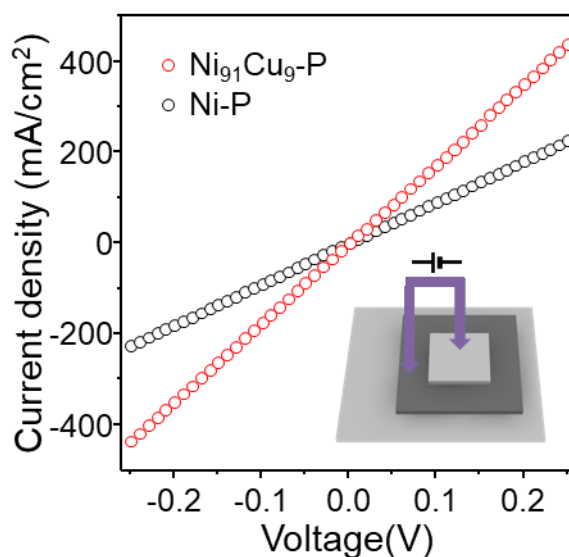


**Figure 39.** Currents measured as a function of the applied voltage ranging from -0.25 to 0.25 V with Ni<sub>91</sub>Cu<sub>9</sub>-P and Ni-P. The inset shows a schematic illustration of I-V measurement of a device.

### 5.3.4 Two-electrode planar electrochemical cells

The poor stability of the OER electrode at such a high voltage was evaluated with the oxygen content of the film by using oxygen plasma treatment. Figure 37e shows the current

density as a function of the treatment time when 10 V was applied. With oxygen plasma treatment for 30 min, the current density was measured to be approximately 3 mA/cm<sup>2</sup>, which was similar to one measured at 5 V in the non-treated sample. However, interestingly, unlike the non-treated sample, there was no decrease in the current density and also there were no cracks created in any region of OER electrode, as shown in Figure 37f. This tells us that the OER electrode became quite stable at high voltage due to the treatment. However, as the plasma treatment time increased, the current density decreased, explained via the increase in the oxygen content in the film, as shown in Figure 37e. Actually, the conductance of the NiO film by the sputtering method was lower than that of the NiP film, as shown in Figure 40a. When the NiO film was used as an OER electrode instead of the NiP film, the current density decreased by 4.4 times, as shown in Figure 40b. This is in good agreement with the decrease in the current density with the increasing plasma treatment in Figure 37e. It has been reported in a few papers that an increase in the oxygen content in the Ni-P film could improve the stability of the materials due to the larger dissociation energy (391.6 kJ/mol) of the Ni-O [56-58]. Thus, it is believed that the oxygen plasma treatment creates an oxygen-rich layer at the surface, acting as a barrier to the out-diffusion of the phosphorous atoms to the electrolytes [59]. This may be confirmed by the increase (5.5 → 6.0) of the pH measured in pure water by the plasma treatment, as shown in Figure 37d. It is also thought that the high voltage could locally focus on a specific area, leading to the dissolution of the phosphorous atoms and creating cracks in Ni-P film [34,60].

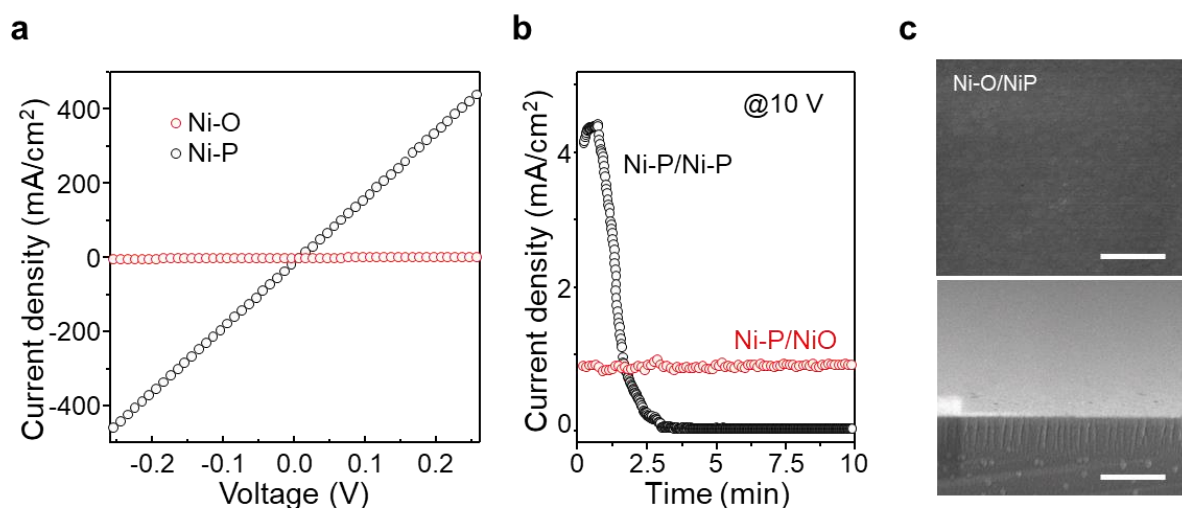


**Figure 40.** (a) Currents measured as a function of the applied voltage ranging from -0.25 to 0.25 V with Ni-P and NiO. (b) Current densities measured at 10 V of Ni-P/Ni-P, Ni-P for HER/NiO for OER with two-electrode cell in pure water at voltages of 10 V. (c) The SEM

images of the NiO for OER films after the HER and OER reaction at 10 V in pure water, respectively. Scale bar: 500 nm.

The NiCu-P films were deposited on the two interdigitated Ni electrodes on a SiO<sub>2</sub>/Si substrate. As an OER electrode, the film was treated with oxygen plasma for 30 min, while the film was used as a HER electrode without any modification, followed by the UV-Ozone treatment to make the surface hydrophilic. Thus, two-electrode planar devices based on the NiCu-P films as bifunctional catalysts were fabricated. The schematic diagram for the device and the photos of the devices fabricated on the 4-inch SiO<sub>2</sub>/Si wafer are shown in Figure 41a. With a few pure water drops of pH 7 onto the cells of approximately 2 x 2 cm<sup>2</sup> in area, the current was measured as a function of the applied voltage, plotted in Figure 41b. Under 2 V, a current of 0.118 mA was obtained and as the voltage increased to 10 V, the current increased to 1.71 mA. By the applied voltage, many gas bubbles were obviously observed between the electrodes, as shown in the inset and the Supplementary Movie 1. The movie also showed that the bubbles were pushed to the air out and disappeared. The current with the voltage was quite linear and there was no change in the current for 10 min (Figure 41c), meaning that the water splitting performance was not degraded at the high voltages. Compared to the pristine Ni-P films, an enhancement in the current of 17 % was obtained, as shown in Figure 42. The water removal rate in Figure 41b was calculated based on the number of charges transferred from the HER electrode to the OER electrode. Faraday's law of electrolysis states the amount of electrolysis reactant mH<sub>2</sub>O [61];

$$m_{H_2O} = \frac{QM_{H_2O}}{zF}$$

where Q is the total amount of electric charges passed through the electrodes for 1 h,  $M_{H_2O}$  is the molar weight of H<sub>2</sub>O (18 g/mol),  $F$  is the Faraday constant (96485.3 C/mol), and  $z$  (= 2) is the number of electrons to split one water molecule to gases. The rate of water removal at the catalytic electrode surface and thus the water splitting rate can be calculated from the current measurement.

$$\frac{dm_{H_2O}}{dt} = \frac{M_{H_2O}}{zF} \frac{dQ}{dt} = \frac{I \times M_{H_2O}}{zF} = R_{H_2O}$$

It shows that approximately 0.6 ml of water was effectively removed after 10 V was applied for 1 hr. After 3 hr, the SEM images and the measured current supported the excellent stability of the films, as shown in Figure 41d. The Supplementary Movie 2 also clearly showed

that when the water was fully removed, the current dropped to zero, indicating that the current was due to the water splitting.

As one of the practical applications, the cell of approximately  $2 \times 2 \text{ cm}^2$  in the area was attached to the inner surface of a transparent headlamp of a car and the current were measured as a function of the relative humidity. The humid air from a humidifier, balanced by dry air, was introduced into the headlamp under pressure of 1 atm. By controlling the valve between the humid/air sources, the humidity inside the chamber could be tuned over the range of 20 to 99 %, measured by the humidity sensor (Daekwang Instrument Inc., TH-05, Republic of Korea). At 20 %, a tiny current of 0.059 mA at a float voltage of 13.6 V was measured, indicating that there was only a little water between the electrodes. As the humidity increased to 70 %, a current of 0.58 mA was measured and it reached 1.07 mA at > 99%. In Figure 41e, the photos of the attached 4 cells showed that the water condensed onto the inner surface was effectively removed and the inside of the headlamp became quite transparent, meaning that the relative humidity of the air inside the headlamp decreased. This was evident from the photos taken after 60 min when the devices were not attached on the surface, as shown in Figure 43. The Supplementary Movie 3 also clearly showed that the water adsorbed onto the surface and inside of the headlamp was clearly removed by the attached cells.

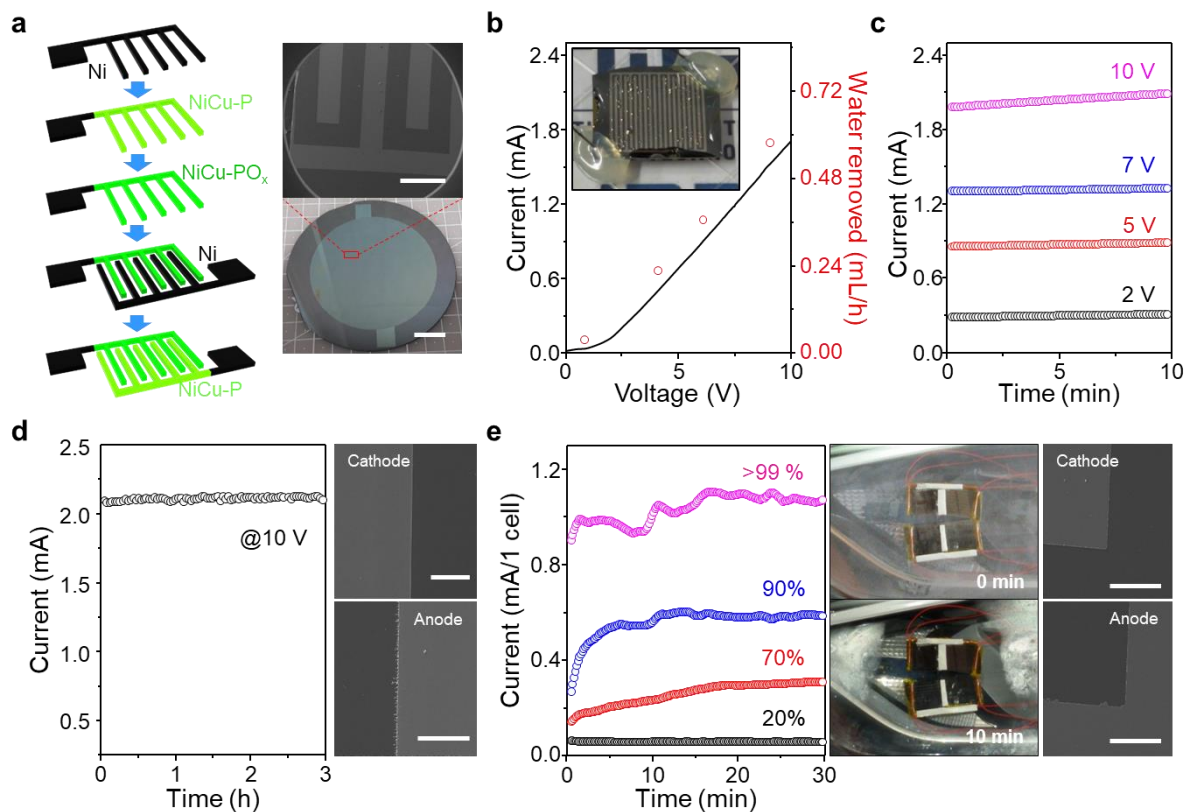


**Figure 41.** (a) Schematic illustration for the fabrication of two-electrode planar cells, composed of two interdigitated electrodes of NiCu-P for HER and NiCu-PO<sub>x</sub> for OER. The photo and SEM image of the cell at a wafer scale was also shown. scale bar: 1, 20 mm. (b) Currents measured as a function of the applied voltage with a few pure water drops onto the cells of approximately 2 x 2 cm<sup>2</sup> in area. The inset shows the gas bubbles generated between the two electrodes. The water removal rate with the voltage was also plotted. (c) Currents measured at various voltages from 2 to 10 V in pure water. (d) Currents measured at 10 V during 3 hrs when the cell was dipped into pure water. The SEM images of the Ni<sub>91</sub>Cu<sub>9</sub>-P films after the HER and OER reaction at 10 V in pure water, respectively. Scale bar: 50 μm. (e) Currents measured under various humidity of the inside of the headlamp of a car from 20 to 99 %. The 4 cells were attached to the inner surface and the photos after the reaction at 13.6 V for 10 min were shown. The SEM images of the Ni<sub>91</sub>Cu<sub>9</sub>-P films after the reaction were also shown. scale bar: 50 μm.

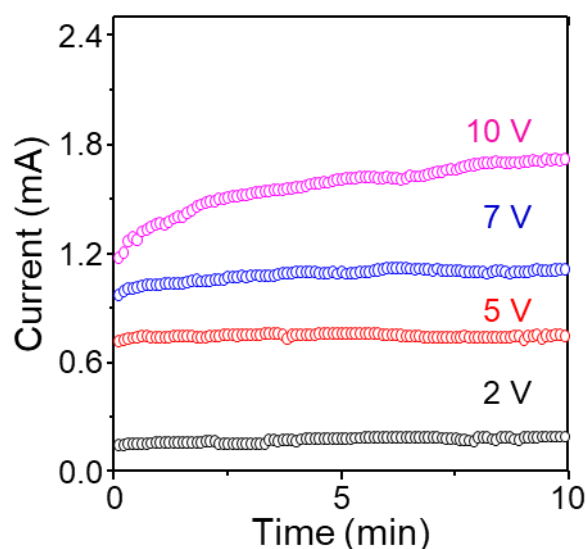


**Figure 42.** Currents measured at various voltages from 2 to 10 V with two-electrode planar cells based on Ni-P for HER/Ni-PO<sub>x</sub> for OER in pure water.



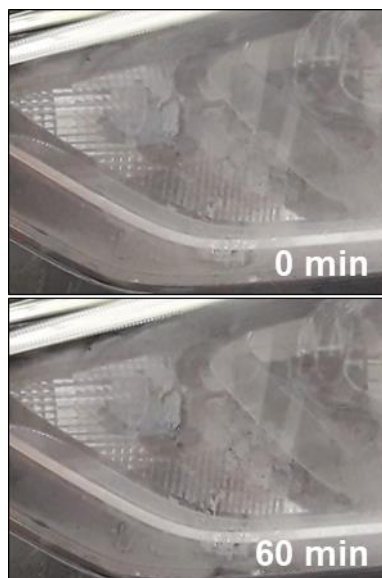


**Figure 43.** Photos of the inside surface of headlamp before/after 60 minutes under the humidity of 99%.

A flexible and transparent cell, composed of NiCu-P films deposited on the 50 nm-thick Ni coated polyethylene naphthalate (PEN) substrate, was also fabricated by introducing hole patterns of 80  $\mu\text{m}$  in diameter, as shown in Figure 44a. The photo shows that it seems quite transparent. Figure 44b shows that the device has high transparency of  $\sim 90\%$  in the wavelength between 400 and 800 nm. The transparency is evident in the photograph of the device attached on the surface of the headlamp in the inset of Figure 44c. When the current was measured under the humidity of 99%, a current of 0.95 mA with an excellent stability was measured at 13.6 V, as shown in Figure 44c. The lower current of the devices may be ascribed to the decrease in the thickness of the NiCu-P films ( $\sim 0.3\ \mu\text{m}$ ), compared with that of the film deposited on the  $\text{SiO}_2/\text{Si}$  substrate ( $\sim 0.6\ \mu\text{m}$ ). Finally, the flexibility of the device needs to be evaluated for broad applications. It seemed that the devices on the PEN substrate were quite flexible, as shown in the inset of the Figure 44d. To evaluate the effect of the bending motion on the water-splitting performance, the device was dipped into the pure water and the current was measured at 10 V as a function of the bending curvature, as shown in Figures 44d and 45. With no bending, a current of 1.33 mA was measured. At a curvature of  $0.13\ \text{cm}^{-1}$ , the current decreased to 1.21 mA and it slowly decreased until the curvature was  $0.23\ \text{cm}^{-1}$ . However, the current was quite stable, as shown in Figure 45b. Further increase in the curvature to  $0.39\ \text{cm}^{-1}$  significantly decreased to 0.25 mA and as the reaction proceeded, the current was eventually dropped to almost zero. Although it is believed that the films can be broken at large curvature,



it is notable that the water removal capability was found to maintain over 75 % at a curvature of 0.18/cm.

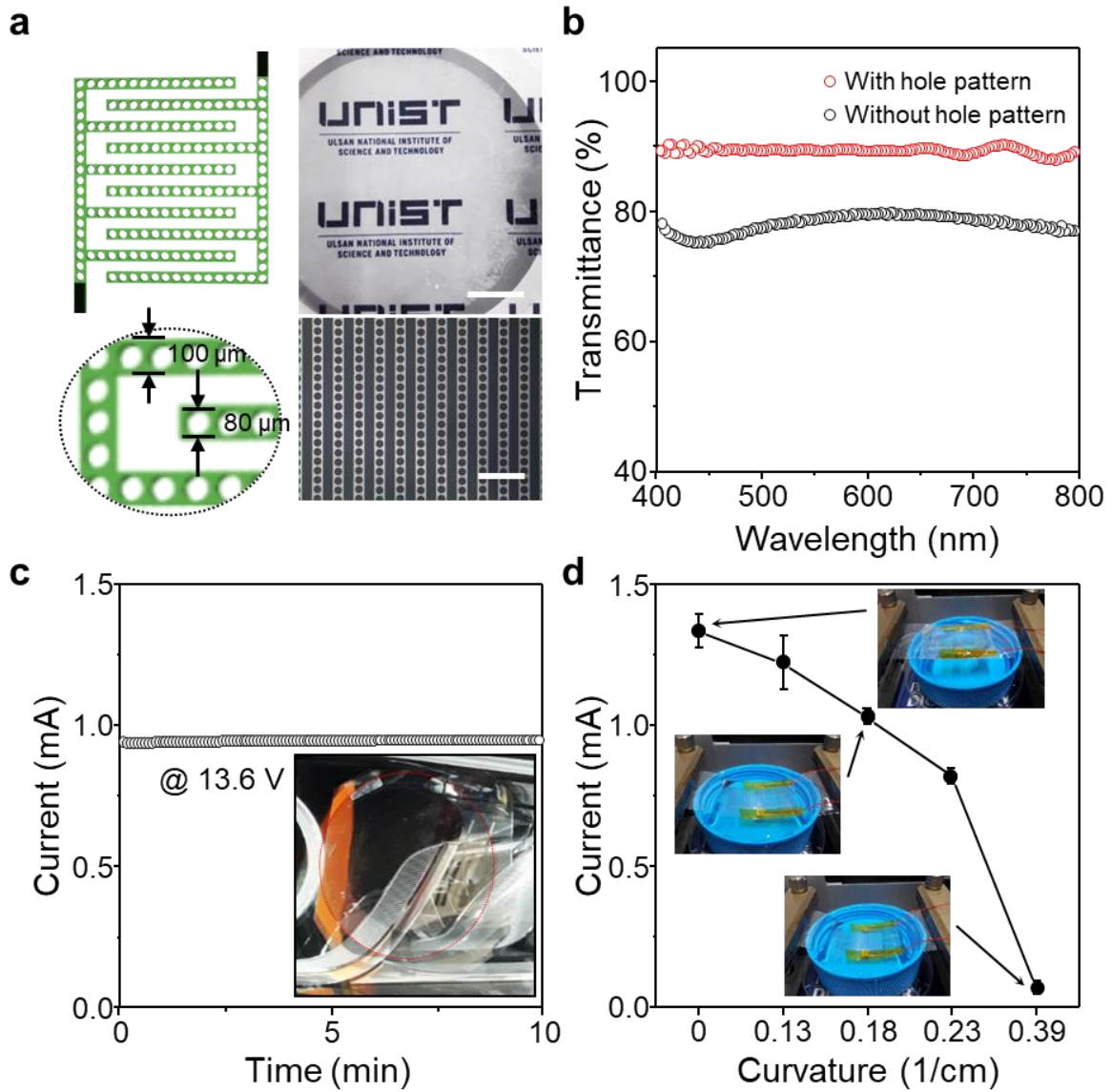


**Figure 44.** (a) Schematic images of flexible cells with hole patterns fabricated on PEN substrate. The photo and SEM image of the cell at a wafer scale was also shown. scale bar: 2 cm, 0.4 mm. (b) Transmittance spectra of the cells with and without hole patterns. (c) Currents measured at 13.6 V under 99 % relative humidity of the headlamp of a car. The cell was attached to the inner surface of the headlamp. (d) Currents measured at 10 V with the curvature of the bending motion when it was dipped into the pure water, as shown in the inset.

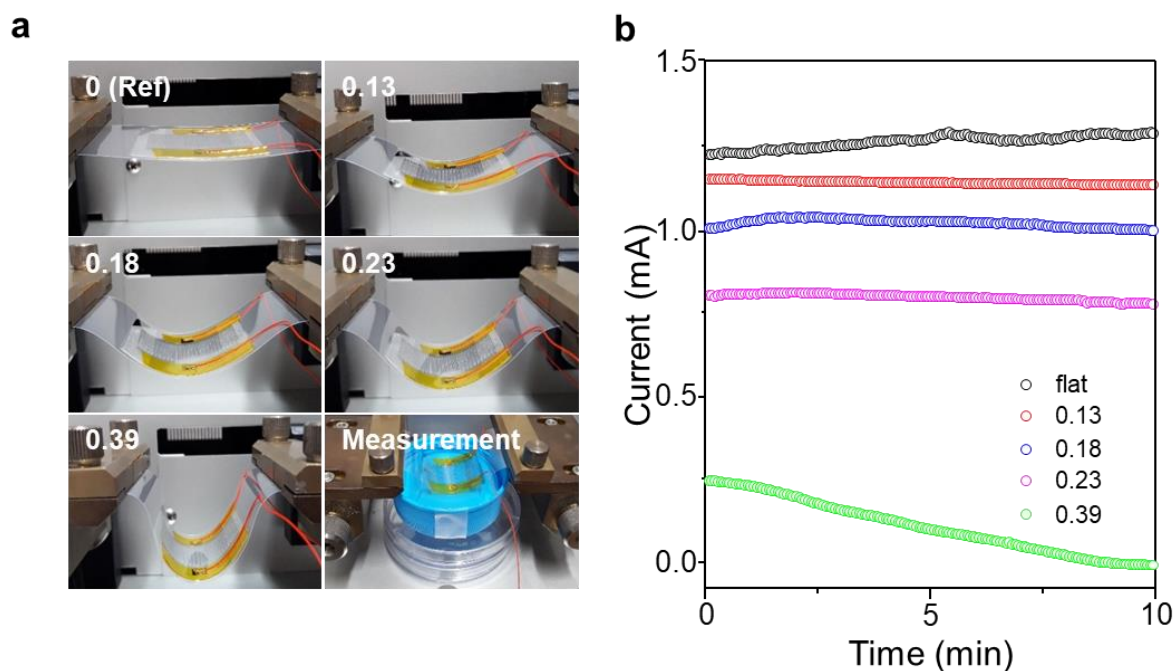


**Figure 45.** (a) Photos of bending flexible planar devices with different bending curvature. (b) Currents measured with the flexible and transparent device at 10 V in pure water with different bending curvature.

## 5.4 Conclusion

In conclusion, we reported a facile strategy to fabricate the two-electrode electrochemical cells for effective removal of water condensed on surface by the water splitting technology, based on bifunctional NiCu-P catalysts synthesized by electrodeposition. It is also shown that the technology can control the humidity of the air inside of the headlamp. The microstructural analysis by using XRD and TEM tools showed that the NiCu-P films were Ni-rich amorphous materials with various nanocrystalline phases such as Ni<sub>12</sub>P<sub>5</sub> and Ni<sub>3</sub>P at low Cu content (< 9 at.%). In a three-electrode configuration, as the Cu content increased to Cu 9 at. %, the overpotentials were decreased to 48 mV for HER in acidic solution and 330 mV at -10 mA/cm<sup>2</sup> and at 20 mA/cm<sup>2</sup> for OER in alkaline solution, respectively. However, further increase in the Cu content resulted in the segregation of Cu-rich phase instead of the solid solution, increasing the overpotentials to 125 mV and 410 mV at Cu 64 at. %, for HER and OER, respectively. Thus, the best electrocatalytic performance was obtained in NiCu-P films

with Cu 9 at. %, which might be ascribed to the low charge transfer resistance due to the solid solution of Ni and Cu in the phosphor environment.

To evaluate the water removal capability of the catalysts, a two-electrode electrochemical cell was fabricated by depositing the NiCu-P films on Ni substrates. For HER, the as-prepared film was used without any modifications. However, for OER, the films were treated with oxygen plasma, producing an oxygen-rich layer at the surface. This significantly decreased the dissolution of the phosphorous atoms and prevented the formation of any desiccation, thus, enhancing the stability of the films at high potentials over 10 V. In pure water with about pH 7, the cell was successfully proven to be effective in removing the water at a rate of 0.6 ml/hr at 10 V, calculated based on the amount of charge transferred from the HER electrode to the OER electrode.

The NiCu-P films were then deposited on two interdigitated Ni electrodes on a SiO<sub>2</sub>/Si substrate and the planar-type electrochemical cell of approximately 2 × 2 cm<sup>2</sup> was fabricated. The four cells were attached on the surface of a transparent headlamp of a car and 10 V was applied to the cells at the relative humidity of > 99 %. Within 10 min, the water condensed onto the surface was effectively removed and the headlamp became quite clean, meaning that the humidity decreased. At last a flexible cell with transparency over 90 % was fabricated and the water removal capability was found to maintain over 75 % at a curvature of 0.18/cm. Thus, the water splitting is a promising technology to effectively remove the water for a long time. It is also possible to fabricate flexible and transparent devices, which will expand the potential applications.

## 5.5 References

- 1 Y. Wang, G. Zhang, W. Xu, P. Wan, Z. Lu, Y. Li, X. Sun, A 3D Nanoporous Ni-Mo Electrocatalyst with Negligible Overpotential for Alkaline Hydrogen Evolution, *ChemElectroChem* 1(7) (2014) 1138-1144.
- 2 J. Li, Y. Wang, T. Zhou, H. Zhang, X. Sun, J. Tang, L. Zhang, A.M. Al-Enizi, Z. Yang, G. Zheng, Nanoparticle Superlattices as Efficient Bifunctional Electrocatalysts for Water Splitting, *J Am Chem Soc* 137(45) (2015) 14305-12.
- 3 H. Zhou, Y. Wang, R. He, F. Yu, J. Sun, F. Wang, Y. Lan, Z. Ren, S. Chen, One-step synthesis of self-supported porous NiSe<sub>2</sub>/Ni hybrid foam: An efficient 3D electrode for hydrogen evolution reaction, *Nano Energy* 20 (2016) 29-36.
- 4 Y. Lee, J. Suntivich, K.J. May, E.E. Perry, Y. Shao-Horn, Synthesis and Activities of Rutile IrO<sub>2</sub> and RuO<sub>2</sub> Nanoparticles for Oxygen Evolution in Acid and Alkaline Solutions, *J Phys Chem Lett* 3(3) (2012) 399-404.
- 5 M. D. Merrill & R. C. Dougherty, Metal Oxide Catalysts for the Evolution of O<sub>2</sub> from H<sub>2</sub>O. *J. Phys. Chem. C* 112 (2008) 3655–3666.
- 6 M.W. Louie, A.T. Bell, An investigation of thin-film Ni-Fe oxide catalysts for the electrochemical evolution of oxygen, *J Am Chem Soc* 135(33) (2013) 12329-37.
- 7 M. Ledendecker, H. Schlott, M. Antonietti, B. Meyer, M. Shalom, Experimental and Theoretical Assessment of Ni-Based Binary Compounds for the Hydrogen Evolution Reaction, *Advanced Energy Materials* 7(5) (2017).
- 8 Y. Yang, K. Zhang, H. Lin, X. Li, H.C. Chan, L. Yang, Q. Gao, MoS<sub>2</sub>-Ni<sub>3</sub>S<sub>2</sub> Heteronanorods as Efficient and Stable Bifunctional Electrocatalysts for Overall Water Splitting, *ACS Catalysis* 7(4) (2017) 2357-2366.
- 9 Y. Huang, J. Ge, J. Hu, J. Zhang, J. Hao, Y. Wei, Nitrogen-Doped Porous Molybdenum Carbide and Phosphide Hybrids on a Carbon Matrix as Highly Effective Electrocatalysts for the Hydrogen Evolution Reaction, *Advanced Energy Materials* 8(6) (2018).
- 10 V. Kiran, D. Mukherjee, R.N. Jenjeti, S. Sampath, Active guests in the MoS<sub>2</sub>/MoSe<sub>2</sub> host lattice: efficient hydrogen evolution using few-layer alloys of MoS<sub>2</sub>(1-x)Se<sub>2x</sub>, *Nanoscale* 6(21) (2014) 12856-63.

- 11 B. Zhao, L. Zhang, D. Zhen, S. Yoo, Y. Ding, D. Chen, Y. Chen, Q. Zhang, B. Doyle, X. Xiong, M. Liu, A tailored double perovskite nanofiber catalyst enables ultrafast oxygen evolution, *Nat Commun* 8 (2017) 14586.
- 12 R.P. Forslund, W.G. Hardin, X. Rong, A.M. Abakumov, D. Filimonov, C.T. Alexander, J.T. Mefford, H. Iyer, A.M. Kolpak, K.P. Johnston, K.J. Stevenson, Exceptional electrocatalytic oxygen evolution via tunable charge transfer interactions in  $\text{La}_{0.5}\text{Sr}_{1.5}\text{Ni}_{1-x}\text{Fe}_x\text{O}_{4\pm\delta}$  Ruddlesden-Popper oxides, *Nat Commun* 9(1) (2018) 3150.
- 13 Y. Zheng, et al., Toward Design of Synergistically Active Carbon-Based Catalysts for Electrocatalytic Hydrogen Evolution. *ACS Nano* 8, (2014) 5290–5296.
- 14 X. Lu, W.L. Yim, B.H. Suryanto, C. Zhao, Electrocatalytic oxygen evolution at surface-oxidized multiwall carbon nanotubes, *J Am Chem Soc* 137(8) (2015) 2901-7.
- 15 H. Sun, X. Xu, Z. Yan, X. Chen, F. Cheng, P.S. Weiss, J. Chen, Porous Multishelled  $\text{Ni}_2\text{P}$  Hollow Microspheres as an Active Electrocatalyst for Hydrogen and Oxygen Evolution, *Chemistry of Materials* 29(19) (2017) 8539-8547.
- 16 E.J. Popczun, J.R. McKone, C.G. Read, A.J. Biacchi, A.M. Wiltrout, N.S. Lewis, R.E. Schaak, Nanostructured nickel phosphide as an electrocatalyst for the hydrogen evolution reaction, *J Am Chem Soc* 135(25) (2013) 9267-70.
- 17 M. Ledendecker, S. Krick Calderon, C. Papp, H.P. Steinruck, M. Antonietti, M. Shalom, The synthesis of nanostructured  $\text{Ni}_5\text{P}_4$  films and their use as a non-noble bifunctional electrocatalyst for full water splitting, *Angew Chem Int Ed Engl* 54(42) (2015) 12361-5.
- 18 Z. Huang, et al.,  $\text{Ni}_{12}\text{P}_5$  Nanoparticles as an Efficient Catalyst for Hydrogen Generation via Electrolysis and Photoelectrolysis. *ACS Nano* 8 (2014) 8121-8129.
- 19 S. Wei, K. Qi, Z. Jin, J. Cao, W. Zheng, H. Chen, X. Cui, One-Step Synthesis of a Self-Supported Copper Phosphide Nanobush for Overall Water Splitting, *ACS Omega* 1(6) (2016) 1367-1373.
- 20 A. Han, H. Zhang, R. Yuan, H. Ji, P. Du, Crystalline Copper Phosphide Nanosheets as an Efficient Janus Catalyst for Overall Water Splitting, *ACS Appl Mater Interfaces* 9(3) (2017) 2240-2248.
- 21 J.A. Vigil, T.N. Lambert, B.T. Christensen, Cobalt phosphide-based nanoparticles as bifunctional electrocatalysts for alkaline water splitting, *Journal of Materials Chemistry A* 4(20) (2016) 7549-7554.

- 22 Y. Xin, X. Kan, L.Y. Gan, Z. Zhang, Heterogeneous Bimetallic Phosphide/Sulfide Nanocomposite for Efficient Solar-Energy-Driven Overall Water Splitting, *ACS Nano* 11(10) (2017) 10303-10312.
- 23 B. Song, K. Li, Y. Yin, T. Wu, L. Dang, M. Cabán-Acevedo, J. Han, T. Gao, X. Wang, Z. Zhang, J.R. Schmidt, P. Xu, S. Jin, Tuning Mixed Nickel Iron Phosphosulfide Nanosheet Electrocatalysts for Enhanced Hydrogen and Oxygen Evolution, *ACS Catalysis* 7(12) (2017) 8549-8557.
- 24 J. Lee, D.-Y. Lee, Sorption characteristics of a novel polymeric desiccant, *International Journal of Refrigeration* 35(7) (2012) 1940-1949.
- 25 J. Sherman, Synthetic zeolites and other microporous oxide molecular sieves. *Proc. Natl. Acad. Sci. USA* 96 (1999) 3471–3478.
- 26 T. Kimura, Water adsorption properties controlled by coating/filling ordered mesoporous silica inside cellulose membranes, *Phys Chem Chem Phys* 15(36) (2013) 15056-61.
- 27 X. Zheng, T.S. Ge, R.Z. Wang, L.M. Hu, Performance study of composite silica gels with different pore sizes and different impregnating hygroscopic salts, *Chemical Engineering Science* 120 (2014) 1-9.
- 28 K. Okada, M. Nakanome, Y. Kameshima, T. Isobe, A. Nakajima, Water vapor adsorption of CaCl<sub>2</sub>-impregnated activated carbon, *Materials Research Bulletin* 45(11) (2010) 1549-1553.
- 29 T.S. Ge, Y.J. Dai, R.Z. Wang, Z.Z. Peng, Experimental comparison and analysis on silica gel and polymer coated fin-tube heat exchangers, *Energy* 35(7) (2010) 2893-2900.
- 30 R. R. Smith, et al., Modeling of a solar-assisted desiccant air conditioner for a residential building. *Energy* 19 (1994) 679-691.
- 31 P. Liu, et al., Catalysts for Hydrogen Evolution from the [NiFe] Hydrogenase to the Ni<sub>2</sub>P(001) Surface: The Importance of Ensemble Effect. *J. Am. Chem. Soc.* 127 (2005) 14871-14878.
- 32 (a) M.H. Hansen, L.A. Stern, L. Feng, J. Rossmeisl, X. Hu, Widely available active sites on Ni<sub>2</sub>P for electrochemical hydrogen evolution--insights from first principles calculations, *Phys Chem Chem Phys* 17(16) (2015) 10823-9. (b) *Energy Environ. Sci.*, 2015, 8, 2347-2351
- 33 J. L. Carbajal and R. E. White, Electrochemical Production and Corrosion Testing of Amorphous Ni-P. *J. Electrochem. Soc.* 135 (1988) 2952–2957.



- 34 B. Elsener, M. Crobu, M.A. Scorciapino, A. Rossi, Electroless deposited Ni–P alloys: corrosion resistance mechanism, *Journal of Applied Electrochemistry* 38(7) (2008) 1053-1060.
- 35 A.R.J. Kucernak, V.N. Naranammalpuram Sundaram, Nickel phosphide: the effect of phosphorus content on hydrogen evolution activity and corrosion resistance in acidic medium, *J. Mater. Chem. A* 2(41) (2014) 17435-17445.
- 36 J. Song, C. Zhu, B.Z. Xu, S. Fu, M.H. Engelhard, R. Ye, D. Du, S.P. Beckman, Y. Lin, Bimetallic Cobalt-Based Phosphide Zeolitic Imidazolate Framework: CoPxPhase-Dependent Electrical Conductivity and Hydrogen Atom Adsorption Energy for Efficient Overall Water Splitting, *Advanced Energy Materials* 7(2) (2017).
- 37 (a) Z. Zhang, G. Yu, H. Li, J. Liu, X. Huang, W. Chen, Theoretical insights into the effective hydrogen evolution on Cu<sub>3</sub>P and its evident improvement by surface-doped Ni atoms, *Phys Chem Chem Phys* 20(15) (2018) 10407-10417. (b) *J. Electrochem. Soc.*, 2005, 152, J23–J26.
- 38 A. Kurowski, et al., Initial stages of Ni–P electrodeposition: growth morphology and composition of deposits. *Electrochem. Commun.* 4 (2002) 565–569.
- 39 C. -H. Chen, et al., Role of Cu<sup>2+</sup> as an Additive in an Electroless Nickel– Phosphorus Plating System: A Stabilizer or a Codeposit?. *Chem. Mater.* 18(13) (2006) 2959-2968.
- 40 L. Hansen, P. Stoltze, K.W. Jacobsen, J.K. Nørskov, Self-diffusion on copper surfaces, *Physical Review B* 44(12) (1991) 6523-6526.
- 41 T.-Y. Kim, H.-J. Son, S.-K. Lim, Y.-I. Song, H.-S. Park, S.-J. Suh, Electroless Nickel Alloy Deposition on SiO<sub>2</sub> for Application as a Diffusion Barrier and Seed Layer in 3D Copper Interconnect Technology, *Journal of Nanoscience and Nanotechnology* 14(12) (2014) 9515-9524.
- 42 B. P. Daly and F. J. Barry, Electrochemical nickel–phosphorus alloy formation. *Int. Mater. Rev.* 48(5) (2003) 326-338.
- 43 A. Jain, G. Hautier, S.P. Ong, C.J. Moore, C.C. Fischer, K.A. Persson, G. Ceder, Formation enthalpies by mixing GGA and GGA+U calculations, *Physical Review B* 84(4) (2011).
- 44 J. Mahmood, F. Li, S.M. Jung, M.S. Okyay, I. Ahmad, S.J. Kim, N. Park, H.Y. Jeong, J.B. Baek, An efficient and pH-universal ruthenium-based catalyst for the hydrogen evolution reaction, *Nat Nanotechnol* 12(5) (2017) 441-446.



- 45 R. Ma, Y. Zhou, Y. Chen, P. Li, Q. Liu, J. Wang, Ultrafine Molybdenum Carbide Nanoparticles Composited with Carbon as a Highly Active Hydrogen-Evolution Electrocatalyst, *Angew Chem Int Ed Engl* 54(49) (2015) 14723-7.
- 46 F.H. Saadi, A.I. Carim, E. Verlage, J.C. Hemminger, N.S. Lewis, M.P. Soriaga, CoP as an Acid-Stable Active Electrocatalyst for the Hydrogen-Evolution Reaction: Electrochemical Synthesis, Interfacial Characterization and Performance Evaluation, *The Journal of Physical Chemistry C* 118(50) (2014) 29294-29300.
- 47 D.E. Schipper, Z. Zhao, H. Thirumalai, A.P. Leitner, S.L. Donaldson, A. Kumar, F. Qin, Z. Wang, L.C. Grabow, J. Bao, K.H. Whitmire, Effects of Catalyst Phase on the Hydrogen Evolution Reaction of Water Splitting: Preparation of Phase-Pure Films of FeP, Fe<sub>2</sub>P, and Fe<sub>3</sub>P and Their Relative Catalytic Activities, *Chemistry of Materials* 30(10) (2018) 3588-3598.
- 48 Y. Tan, H. Wang, P. Liu, Y. Shen, C. Cheng, A. Hirata, T. Fujita, Z. Tang, M. Chen, Versatile nanoporous bimetallic phosphides towards electrochemical water splitting, *Energy & Environmental Science* 9(7) (2016) 2257-2261.
- 49 R.L. Doyle, I.J. Godwin, M.P. Brandon, M.E. Lyons, Redox and electrochemical water splitting catalytic properties of hydrated metal oxide modified electrodes, *Phys Chem Chem Phys* 15(33) (2013) 13737-83.
- 50 M.W. Louie, A.T. Bell, An investigation of thin-film Ni-Fe oxide catalysts for the electrochemical evolution of oxygen, *J Am Chem Soc* 135(33) (2013) 12329-37.
- 51 I. G. Casella, et al., Electrodeposition and Characterization of Nickel-Copper Alloy Films as Electrode Material in Alkaline Media. *J. Electrochem. Soc.* 149 (10) (2002) B465-B471.
- 52 J. Chen, et al., Nickel Hydroxide as an Active Material for the Positive Electrode in Rechargeable Alkaline Batteries. *J. Electrochem. Soc.* 146 (1999) 3606-3612.
- 53 M. Gao, W. Sheng, Z. Zhuang, Q. Fang, S. Gu, J. Jiang, Y. Yan, Efficient water oxidation using nanostructured alpha-nickel-hydroxide as an electrocatalyst, *J Am Chem Soc* 136(19) (2014) 7077-84.
- 54 J. Hu, S. Zheng, X. Zhao, X. Yao, Z. Chen, A theoretical study on the surface and interfacial properties of Ni<sub>3</sub>P for the hydrogen evolution reaction, *Journal of Materials Chemistry A* 6(17) (2018) 7827-7834.
- 55 U. Hofmann and K. G. Weil, On the oxidation of nickel/phosphorus alloys. *Corros. Sci.* 34 (3) (1993) 423-431.

- 56 J. A. Dean, Lange's Handbook Of Chemistry (McGRAW-HILL, 1999).
- 57 J. Ren, J.-g. Wang, J.-f. Li, Y.-w. Li, Density functional theory study on crystal nickel phosphides, Journal of Fuel Chemistry and Technology 35(4) (2007) 458-464.
- 58 Y.Y. Tong, C.D. Gu, J.L. Zhang, M.L. Huang, H. Tang, X.L. Wang, J.P. Tu, Three-dimensional astrocyte-network Ni-P-O compound with superior electrocatalytic activity and stability for methanol oxidation in alkaline environments, Journal of Materials Chemistry A 3(8) (2015) 4669-4678.
- 59 S.P. Murarka, Phosphorus out-diffusion during high temperature anneal of phosphorus-doped polycrystalline silicon and SiO<sub>2</sub>, Journal of Applied Physics 56(8) (1984) 2225-2230.
- 60 H. Föll, M. Leisner, A. Cojocaru, J. Carstensen, Macroporous Semiconductors, Materials 3(5) (2010) 3006-3076.
- 61 A.J. Leenheer, H.A. Atwater, Journal of The Electrochemical Society, 157 (2010) B1290-B1294.

# CURRICULUM VITAE

## PERSONAL INFORMATION

Name: Lee, Tae-Won

Date (Place) of Birth: 01. 10. 1983 (Seoul, Korea)

## EDUCATION

Ph.D. (Aug., 2020): UNIST, Korea; Material Science & Engineering

- Advisor: Prof. Jeong-Min Baik
- Title of Thesis: Kinetics of charge transfer and oxygen evolution via surface functionalization at the transition metal based catalysts

M.S. (Aug., 2014): Yonsei Univ., Korea; Material Science & Engineering

- Advisor: Prof. Hyung-Ho Park
- Title of Thesis: Effect of dispersion characteristic of carbon nanotubes on the electrical property of composite electrode materials

Bachelor (Mar., 2012): Yonsei Univ., Korea; Materials Science & Engineering

## RESEARCH INTERESTS

1. Composite electrocatalysts based on perovskite oxide and transition metal dichalcogenide for overall water splitting
  - $\text{LaMO}_3$  (M=  $\text{Sr}_{0.5}\text{Co}_{0.5}$ , Ni, Co, Fe),  $\text{MoSe}_2$ ,  $\text{NbS}_2$
2. Electrodeposited electrocatalyst based on transition-metal phosphide for water splitting and application for removal of moisture
  - Cu added Ni-P based electrocatalyst for overall water splitting
3. Metal oxide nanoparticle synthesis and application for semiconductor gas sensors
  - ZnO,  $\text{SnO}_2$ , NiO
4. Carbon nanomaterials - based composites for stretchable/transparent electrode
  - Carbon nanotube (CNT) added carbon black-polymer composite for stretchable electrode
  - CNT doped ZnO films for transparent electrode

## RESEARCH TECHNIQUES

1. Surface and Electronic Structure Analysis: X-ray Photoemission Spectroscopy (XPS), Photoemission Spectroscopy (PES), Spectromicroscopy (SPEM)  
(Pohang accelerator Laboratory experiences: 6 times - 4D, 8A1, 8A2)
2. Morphological and Structural Prop. Measurements: XRD, FE-SEM
3. Optical Prop. Measurements: Zeta potential, Dynamic Laser Scattering, FT-IR, UV-vis-NIR Spectrometer
4. Electrical Prop. Measurements: Hall-Effect Measurement, 4-Point Probe

## 1. SCI(E) Journal Articles

- 1) **Tae-Won Lee**, Hee Jun Kim, Jeong Min Baik, “Highly active bifunctional electrocatalyst based on N-doped Graphene Quantum Dot functionalized perovskite oxide and TMDC composite for overall water splitting”, *in preparation*
- 2) Hee Jun Kim, **Tae Won Lee**, Hye Hyeon Kim, U Jeong Yang, Chanul Kim, Kyoung Jin Choi, Heon Lee, Jeong Min Baik, “Triple Layered Ga<sub>2</sub>O<sub>3</sub>/Cu<sub>2</sub>O/Au Photoanodes with Enhanced Photoactivity and Stability by Iron Nickel Oxide Catalysts”, *Journal of Materials Chemistry A*, *accepted*.
- 3) Junho Jun, Heejun Kim, Hak-Jong Choi, **Tae-Won Lee**, Sucheol Ju, Jeong Min Baik, Heon Lee, “A large-area fabrication of moth-eye patterned Au/TiO<sub>2</sub> gap-plasmon structure and its application to plasmonic solar water splitting”, *Solar Energy Materials and Solar Cells*, 201, 110033 (2019)
- 4) Jae Won Lee, Sungwoo Jung, **Tae-Won Lee**, Jinhyeong Jo, Hee Young Chae, Keunsu Choi, Jae Joon Kim, Jun Hee Lee, Changduk Yang, Jeong Min Baik, “High-Output Triboelectric Nanogenerator Based on Dual Inductive and Resonance Effects-Controlled Highly Transparent Polyimide for Self-Powered Sensor Network Systems”, *Advanced Energy Materials*, 9, 1901987 (2019)
- 5) Young Hoon Sung, Jaemin Park, Eun Seo Choi, Tae-Hoon Chung, **Tae-Won Lee**, Hee Jun Kim, Jeong Min Baik, Heon Lee, “InGaN/GaN light emitting diodes grown on nanoimprint-based hollow-patterned sapphire substrates”, *Microelectronic Engineering*, 216, 111082 (2019)
- 6) **Tae-Won Lee**, Hee Jun Kim, Jang Su Park, Jeong Min Baik, “Electrocatalytically driven fast removal of moisture by condensation of vapor and water splitting”, *Nano Energy*, 61, 295 (2019)
- 7) **Tae-Won Lee**, Hyung-Ho Park, “The effect of MWCNTs on the electrical properties of a stretchable carbon composite electrode”, *Composites Science and Technology*, 114, 11 (2015)
- 8) **Tae-Won Lee**, Chang-Sun Park, Hyung-Ho Park, “The effect of ball-milling on the dispersion of carbon nanotubes: the electrical conductivity of carbon nanotubes-incorporated ZnO”, *Journal of the Ceramic Society of Japan*, 122 (8), 634 (2014)

## 2. Non-SCI Journal Articles

- 1) **Tae-Won Lee**, Hyung-Ho Park, “A Study on the Electrical Resistivity of Graphene Added Carbon Black Composite Electrode with Tensile Strain”, *Journal of the Microelectronics and Packaging Society*, 22 (1), 55-61 (2015)
- 2) **Tae-Won Lee**, Hyung-Ho Park, “The Effect of Graphene on the Electrical Properties of a Stretchable Carbon Electrode”, *Journal of the Microelectronics and Packaging Society*, 21 (4), 77-82 (2014)

### 3. Awards

- 1) **우수 논문상** (BK21 플러스 창의소재인력양성사업단), Aug. 19, 2015
- 2) **우수 포스터 발표 논문상** (poster presentation) (2015 춘계 학술대회 (한국마이크로전자 및 패키징학회)), Apr. 2, 2015
- 3) **우수과제 (중소기업청장상)** (산학협력기술개발사업 중소기업청장상), Dec. 17, 2013
- 4) **우수 포스터 발표 논문상** (poster presentation) (2013 년도 정기학술대회 (한국마이크로전자 및 패키징학회)), Nov. 14, 2013

### 4. Conference Presentations

#### ▣ Oral Presentations

- 1) **Tae-Won Lee**, Jeong Min Baik, “Flexible and Transparent Two-terminal Planar Electrocatalytical Systems for Enhanced Moisture Removal”, The 4th International Conference on Nanoenergy and Nanosystems 2019, June. 15~17, 2019, Beijing, China
- 2) **Tae-Won Lee**, Pilgyu Byeon, Hong-Sub Lee, and Hyung-Ho Park, “A study on the BaTiO<sub>3</sub> based ferroelectric tunnel junction using semiconductor electrodes for cross-point arrays”, International Conference on Traditional and Advanced Ceramics 2015, Sep. 9~11, 2015, Bangkok, Thailand

#### ▣ Poster Presentations

- 1) **Tae-Won Lee**, Hee Jun Kim, Jeong Min Baik, “Cu<sub>2</sub>O based Photostable Photoanodes by the Au Passivation for High efficiency Photoelectrochemical Applications”, 2018 추계 학술대회 (한국표면공학회), Nov. 14~16, 2018, Kyungju, Korea
- 2) Hee Jun Kim, **Tae-Won Lee**, Jeong Min Baik, “Pyramidal-shaped metal-dielectric hybrid-structure geometry with asymmetric TiO<sub>2</sub> layer for broadband light absorption and photo-catalytic applications”, SPIE. OPTICS+PHOTONICS, Aug. 19~15, 2018, San Diego, USA
- 3) **Tae-Won Lee**, Hyung-Ho Park, “A Study on the Effects of the Graphene on the Electrical Properties of the Stretchable Carbon Composite Electrode”, The 14<sup>th</sup> International Symposium on Microelectronics and Packaging, Oct. 13~15, 2015, Ilsan, Korea
- 4) **Tae-Won Lee**, Hyung-Ho Park, “A study of component effects on the electrical property of stretchable carbon black based composite” 2015 춘계 학술대회 (한국마이크로전자 및 패키징학회), Apr. 2, 2015, Seoul, Korea
- 5) **Tae-Won Lee**, Min-Hee Hong, Hae-Noo-Ree Jung, Hyung-Ho Park, “Effect of components on the electrical property of stretchable carbon black electrode”, 8th International Conference on Materials Science and Technology (MSAT-8), Dec. 15~16, 2014, Bangkok, Thailand

- 6) **Tae-Won Lee**, Chang-Sun Park, Min-Hee Hong, Hyung-Ho Park, “Effect of components on the electrical and physical properties of conductive carbon pastes”, 2013 년도 정기학술대회 (한국마이크로전자 및 패키징 학회), Nov. 14, 2013, Seoul, Korea
- 7) **Tae-Won Lee**, Jong-Tae Baek, Hyung-Ho Park, “A study of components effect on the property of the conductive carbon black pastes”, 2013 한국세라믹 학회 춘계 연구발표회, Apr. 18~19, 2013, Changwon, Korea

## 5. Patents

- 1) Jang-su Park, Young-eun Hwang, Jeong Min Baik, Hee Jun Kim, **Tae-Won Lee**, “Method Of Manufacturing Electrocatalyst Through One Step Electrodeposition And Electrocatalyst Manufactured Therefrom”, Republic of Korea, Application number: 10-2018-0095514, 08.16.2018 (US 출원: 16/188,650)
- 2) Jang-su Park, Hee Jun Kim, **Tae-Won Lee**, Jeong Min Baik, “Water Decomposition Device And Manufacturing Method Thereof”, Republic of Korea, Application number: 10-2018-0097437, 08.21.2018 (US 출원: 16/188,650)
- 3) Hyung Ho Park, Hee Yoon Chung, Hae Noo Ree Jung, **Tae-Won Lee**, “Porous structure and method of fabricating the same”, Republic of Korea, Application number: 10-2016-0067408, (US 출원: 15/607,119) Registration Number: 10-1902618-0000

## 6. Projects

- 1) “지능형 신축성 카본전극 소재개발”, 산학연 공동기술개발 전국사업, 2011~2013 (한국산학연합회장상, 중소기업청장상)
- 2) “그래핀을 이용한 스마트 연성전극 신소재 개발”, 중소기업 기술혁신개발사업, 2012~2014
- 3) “열 극한물성 시스템 연구”, 글로벌 프론티어 사업, 2014~2016 (1 단계)
- 4) “고온 안정성을 갖는 Flexible, Tough & Strong 에어로겔 합성”, 이공학개인지초연구지원사업, 2015~2016
- 5) “광전기 촉매를 활용한 헤드램프용 습기 제거 기술(소재) 개발”, 산학협동 연구과제 (현대엔지비), 2017~2018
- 6) “IoT 센서기반 유해물질 안전대응 플랫폼 구축”, 과학기술기반 지역수요 맞춤형 R&D 지원사업, 2018~2019
- 7) “니어제로 김스에너지 페로브스카이트 전기촉매 기초연구실”, 기초연구실지원사업, 2019~2020